Continued Development of a Joint-Type Knee Wear Simulator

by

Johan van der Merwe

Thesis presented in partial fulfilment of the requirements for the degree of Master of Science in Engineering (Mechatronic) at Stellenbosch University

Department of Mechanical and Mechatronic Engineering,
University of Stellenbosch,
Private Bag X1, Matieland 7602, South Africa.

Supervisors:

Prof. C. Scheffer Dr. C. Muller

March 2012

Declaration

By submitting this thesis electronically, I declare that the entirety of the work contained therein is my own, original work, that I am the sole author thereof (save to the extent explicitly otherwise stated), that reproduction and publication thereof by Stellenbosch University will not infringe any third party rights and that I have not previously in its entirety or in part submitted it for obtaining any qualification.

Signature: .....
J. van der Merwe

Date: February 2012 .....

Abstract

Continued Development of a Joint-Type Knee Wear Simulator

J. van der Merwe

Department of Mechanical and Mechatronic Engineering,
University of Stellenbosch,
Private Bag X1, Matieland 7602, South Africa.

Thesis: MScEng (Mechatronic)

March 2012

This thesis is concerned with the continued development of the Stellenbosch University joint-type knee wear simulator. Initially, information regarding simulators from the literature and commercial entities was collected to provide a knowledge base for current and future work. To further the design of the simulator itself, electronic hardware and software subsystems was developed and evaluated during experimental testing procedures. National Instruments' cDAQ 9174 data acquisition unit was deemed inadequate for real-time input-output control, though proved sufficient for signal capturing purposes in conjunction with LabView software. Furthermore, the various servo-pneumatic sub-circuits' individual ability to conform to the ISO 14243 series standards' protocol led to the estimation of measurable performance criteria and the application to a single circuit for illustration. The anterior/posterior actuation circuit in question demonstrated adequate performance for the cases where the piston's rod was respectively fixed and free to move. *In-silico* modelling and identification of the relevant servo-pneumatic components then commenced, with the valve and cylinder chamber models yielding adequate estimates of the recorded data. The identified quasi-static friction model proved sensitive to transient effects present within the system, resulting in performance deterioration of the integrated model. Sufficiently accounting for these effects would result in the emergence of the sub-circuit's model as an invaluable tool in terms of control system development, prediction of the simulator's behaviour and subsequent design recommendations. Future work therefore concerns improvement, identification and integration of the various sub-circuit models to fully exploit the aforementioned advantages.

Uittreksel

Voortgesette Ontwikkeling van 'n Gewrigstipe Knie-afslytingsimulator

J. van der Merwe

Departement Meganiese en Megatroniese Ingenieurswese,
Universiteit van Stellenbosch,
Privaatsak X1, Matieland 7602, Suid Afrika.

Tesis: MScIng (Megatronies)

Maart 2012

Hierdie tesis handel oor die voortgesette ontwikkeling van Universiteit Stellenbosch se gewrigstipe knie-afslytingsimulator. Aanvanklik is inligting versamel vanaf literatuur en kommersiële entiteite om sodoende 'n kennisbasis te verskaf vir huidige en toekomstige werk. Elektroniese hardeware en sagteware stelsels is ontwerp en geëvalueer tydens toetsprosedures om die ontwerp van die simuleerder self te verbeter. National Instruments se cDAQ 9174 dataversamelaarseenheid word onvoldoende geag vir intydse inset-uitset beheer, maar wel vir dataversamelingsdoeleindes tesame met LabView sagteware. Die nodigheid om die verskeie servo-pneumatiese sub-stroombane se individuele vermoë om aan te pas by die ISO 14243-reeks se protokol-standaarde te ondersoek, het gelei tot die beraming van meetbare werkverrigtingskriteria en die toepassing daarvan ter illustrasie. Die anterior/posterior stroombaan het voldoende werksverrigting getoon vir studies waar die suier se stang onderskeidelik vas en los was. *In-silico* modellering en die identifisering van servo-pneumatiese komponente het hierna begin. Die klep en silinderkamer modelle het voldoende skattings gelewer van die gemete data. Die geïdentifiseerde kwasistatiese wrywingsmodel het sensitiwiteit getoon teenoor die oorgangseffekte teenwoordig in die stelsel wat gelei het tot verminderde werksverrigting van die geïntegreerde model. Deur rekening te hou met sulke effekte kan die sub-stelsel se model waardevol wees sover dit beheerstelsel ontwikkeling aangaan, sowel as die voorspelling van die simuleerder se optrede en die daaropvolgende ontwerpsvoorstelle. Toekomstige navorsing kan fokus op die verbetering, identifikasie en integrasie van die verskeie sub-stroombaan modelle om die voorafgenoemde potensiaal ten volle ontgin.

Acknowledgements

I would like to express my sincere gratitude to the following people who have contributed and helped towards this work's completion:

- To my supervisors, Prof. Cornie Scheffer and Dr. Cobus Muller for their valuable advice, guidance and encouragement. Thank you for the opportunity to do this work, for trusting me to do it to the best of my ability and for helping me to exceed even that.
- To Stephen Plumb from National Instruments, for taking the time to help me debug my troublesome LabView VI's.
- To Coen Pretorius from Festo, for putting up with my ignorance and a legion of tedious requests.
- To my colleagues at BERG, thank you for your help, advice and all the good times and late nights shared.
- To my family, who supported me unconditionally and never once doubted my ability.

The financial assistance of the National Research Foundation (NRF) towards this research is hereby acknowledged. Opinions expressed and conclusions arrived at, are those of the author and are not necessarily to be attributed to the NRF.

Dedications

To Him Who makes all things possible

Contents

List of Figures

List of Tables

Nomenclature

Abbreviations

ACL	Anterior Cruciate Ligament
ADL	Activities of Daily Living
A/P	Anterior/Posterior
AxF	Axial Force
DAQ	Data Acquisition Device
F/E	Flexion/Extension
GMS	Generalised Maxwell Slip
HTO	High Tibial Osteotomy
ID	Inside Diameter
I/E	Internal/External
I/O	Input/Output
ISO	International Organisation for Standardization
LVDT	Linear Variable Differential Transducer
PC	Personal or Desktop Computer
PCL	Posterior Cruciate Ligament
PID	Proportional-Integral-Derivative
PLC	Programmable Logic Controller
RIO	Real-time Input/Output
SU	Stellenbosch University
TKA	Total Knee Arthroplasty
TKR	Total Knee Replacement
UHMWPE	Ultra High Molecular Weight Polyethylene
UKA	Unicompartmental Knee Arthroplasty
USB	Universal Serial Bus
VI	Virtual Instrument
V/V	Varus/Valgus

Symbols

A	Area	$[\mathrm{m}^2]$
a	Cracking Pressure Ratio	[ ]
b	Critical Pressure Ratio	[ ]
C	Sonic Conductance	$[\mathrm{m}^3.\mathrm{Pa}^{-1}.\mathrm{s}^{-1}]$
Cd	Discharge Coefficient	[ ]
c	Speed of Sound	$[\mathrm{m.s}^{-1}]$
cp	Specific Heat Capacity at Constant Pressure	$[\mathrm{m}^2.\mathrm{s}^{-2}.\mathrm{K}^{-1}]$
cv	Specific Heat Capacity at Constant Volume	$[\mathrm{m}^2.\mathrm{s}^{-2}.\mathrm{K}^{-1}]$
D	Diameter	[m]
F	Force	[N]
f	Predicted Model Value	[Inherited]
L	Length	[m]
MAE	Mean Absolute Error	[Inherited]
m	Mass	[kg]
n	Number of Elements	[#]
$\dot{m}$	Mass Flow Rate	$[\mathrm{kg.s}^{-1}]$
P	Absolute Pressure	[Pa]
$\dot{P}$	Rate of Pressure Change	$[\mathrm{Pa.s}^{-1}]$
R	Gas Constant	$[\mathrm{J.kg}^{-1}.\mathrm{K}^{-1}]$
S	Stribeck Curve	[N]
T	Temperature	[K]
t	Time	[s]
u	Control Signal	[V]
V	Volume	$[\mathrm{m}^3]$
w	Width	[m]
x	Displacement	[m]
$\dot{x}$	Velocity	$[\mathrm{m.s}^{-1}]$
$\ddot{x}$	Acceleration	$[\mathrm{m.s}^{-2}]$
y	Recorded Experimental Value	[Inherited]
α	Heat Transfer Coefficient	[ ]
β	Subsonic Flow Index	[ ]
δ	Arbitrary Stribeck Power	[ ]
ε	Stribeck Threshold	$[\mathrm{m.s}^{-1}]$
γ	Ratio of Specific Heats	[ ]
ρ	Density	$[\mathrm{kg.m}^{-3}]$
ϕ	Relative Humidity	[%]
ψ	Flow Function	[ ]

Subscripts

A	Flow Path
a	Atmospheric
B	Flow Path
b	Bias
$choked$	Choked Flow
cf	Coulomb Friction
cr	Critical Ratio
d	Downstream
e	Extended
eff	Effective
ex	Exhaust
f	Friction
h	Bored Hole
i	Element
in	Inlet
ISO	ISO standard
L	Load
max	Maximum
p	Piston
r	Piston Rod
s	Stribeck Velocity
sf	Static or Breakaway Friction
sp	Spool
t	Tube
u	Upstream
v	Vessel
vf	Viscous Friction
0	Reference Condition

Chapter 1

Introduction

1.1 Background

The notion of knee arthroplasty has been around for more than a century, with the concepts upon which modern knee replacements are based dating back to Thermestocles Gluck's lectures in Berlin during 1890 (Callaghan, 2003). Thanks to numerous technical advancements during the ensuing decades, knee replacement surgery has now become a common method used for treating joint degradation, with more than eighty thousand procedures performed in the United Kingdom during 2010 (The NJR Centre, Hemel Hempstead, 2010) alone. Due to their widespread use, the need to somehow investigate an implant's performance has consequently arisen. Various quantifiable measures exist against which said implant may be evaluated, each measure being studied via a method most suited to the task. One such measure, and that of interest during this work, is wear.

In-vivo wear studies performed on explanted knee replacements, while providing valuable insights, are unfortunately ill suited to the investigation of new implant designs, as both sufficiently large donor populations and long term use prior to explantation is required. On the other hand, *in-vitro* wear evaluation has successfully been conducted to this effect for a number of years now, mostly upon test rigs reminiscent of that detailed by Walker *et al.* (1997). Indeed, it was upon a version of the knee wear simulator for which said author was responsible that the ISO 14243 series of standards which prescribe load and displacement parameters for such machines as well as methods of measurements, were developed (Walker *et al.*, 2000).

Such is the perceived value of standardised *in-vitro* wear evaluation that numerous commercial testing solutions are available to researchers with sufficient funding and understandably so - while not only enabling refinement of an implant's design, long term simulation of the gait cycle provides a means of obtaining proof-of-concept prior to clinical trials. This serves, among other things, to reduce the risk to a patient willing to test a newly developed implant

or, in the least and from a purely pragmatic point of view, could only aid the process of acquiring ethical approval to conduct such pilot studies.

1.2 Motivation

The overarching purpose of this work is the continued development of the Stellenbosch University (SU) joint-type knee wear simulator, which in turn stems from the need to investigate the wear of a knee implant currently being developed by the Biomedical Engineering Research Group. Said machine's mechanical design has previously been completed based on requirements derived from the ISO 14243 series standards, and makes use of pneumatic actuators as a cost-effective alternative to hydraulic and electromechanical devices.

The use of pneumatics does, however, have some disadvantages, such as the presence of non-linearities, susceptibility to friction effects and relatively limited response times in the presence of high loads. It would be ideal if the simulator is capable of performing tests conforming to the ISO 14243 standards in terms both load and displacement. Various commercial pneumatically actuated simulators are available, although few, if any, of them are capable of performing ISO based tests - those that can, are typically hybrid systems, with some degrees of freedom being actuated by either hydraulic or electromechanical actuators.

So the questions remain: would the simulator, as it has been designed, be capable of effecting ISO based load and displacement profiles, on some or all of its controlled degrees of freedom? What, if any, modifications are required to achieve this? And which considerations must be accounted for during continued simulator development? This thesis is focused on finding ways in which such questions may be answered. While time constraints may not allow investigation of all the simulator's components, and hence the behaviour of the overall system, an attempt is made to provide a solid foundation upon which future work may be based.

1.3 Objectives

Both literature and available information concerning commercially available knee wear simulators are to be perused in order to establish the accepted best practice. This would additionally serve to provide a knowledge base for the continued development of the simulator, as most articles detailing the use or even design of a simulator are necessarily concise, and commercial entities tend to be reluctant to part with technical information. While some basic background information will be discussed as a necessary introduction to the more technical aspects of the work, the main focus here will be the required

implementation of loads, displacements and environmental conditions that best mimic physiological conditions, from a design perspective.

While the SU simulator's mechanical assembly has previously been completed as per Van der Merwe (2009), the electronic subsystems have only been detailed to the extent of selecting adequate sensors and regarding potential data acquisition and control software concepts. Therefore, as part of this work the various concepts will be considered and the most promising should be implemented. This would serve the dual purpose of not only identifying the most feasible approach to controlling the simulator electronically, but, once sufficiently developed, the relevant hardware and software may be used to aid in the further characterisation and investigation of the servo-pneumatic actuator circuits. Additionally, safety measures are to be implemented within the pneumatic, electronic and software subsystems.

In order to discern the ability of servo-pneumatic systems to adequately affect physiologically relevant loads and displacements, certain performance requirements will be derived based on information from the ISO 14243 series of standards. This should allow the individual investigation of each pneumatic circuit, thereby enabling a focused assessment of the simulator's subcomponents and facilitating potential future design recommendations. A single pneumatic circuit will be evaluated thus in order to set the precedent.

The final, and one of the major objectives of this work, is the modelling and parameter identification of a pneumatic circuit. This ties in with the purpose of continued simulator development, as accurate models may prove to be invaluable during controller design. Certainly, a study of a servo-pneumatic circuit's behaviour would contribute to an understanding of parameters influencing the overall system's behaviour, thereby enabling a technician to make informed decisions regarding appropriate use of actuators and control valves prior to testing. Such models are to be validated via comparison with the actual pneumatic circuit or individual components in question, during experimental tests that best reflect adherence, or lack thereof, to the aforementioned performance requirements.

Objectives for this work may therefore be summarised as follows:

1. To thoroughly peruse literature and available information regarding the design of joint-type knee wear simulators in order to aid not only the continued design of the SU machine, but also to provide an in-house knowledge base, a summary of applicable references and a starting point for any future work concerning use and application of such a device.

2. To further the electronic hardware, software and safety subsystems' design to a point that experimental validation and parameter identification procedures may be conducted, and that insight may be gained concerning said systems' suitability for application to the simulator as a whole.

3. To derive performance requirements and implement methods enabling individual investigation of the various servo-pneumatic circuits' ability to adequately effect ISO based load and displacement parameters.

4. To develop and test a model of a dynamically actuated servo-pneumatic circuit, along with suitable parameter identification procedures.

Note that the objectives listed previously are numbered for reference, and that their order does not reflect relative importance.

1.4 Thesis Outline

Chapter 2 provides relevant background information concerning the anatomy of the knee as well as various treatment options for joint degradation. This is followed by an in depth discussion concerning the design of joint-type knee wear simulators which is aimed at addressing the first objective previously listed. The chapter concludes with an overview of literature concerning modelling of servo-pneumatic actuator circuits as an introduction for the work done in later chapters.

Chapter 3 presents the SU simulator, as well as work done towards the electronic hardware and software and safety system design. Also detailed is the experimental setup used during parameter identification along with the derivation of applicable performance requirements. This chapter is therefore relevant to the second and third objectives above.

Work done towards meeting the final objective is discussed in Chapter 4, where models for each element of the relevant pneumatic circuit is presented, their parameters identified and validated accordingly. Also presented throughout this chapter is an evaluation of the various components' ability to meet the performance requirements of Chapter 3, with the overall circuit's behaviour investigated in the final sections of Chapter 4.

Finally, Chapter 5 shortly recaps the research that was done, summarises the results that were obtained and suggests recommendations for future work.

Chapter 2

Literature Review

This chapter presents a review of literature relevant to the *in-vitro* simulation of wear on knee implants. To start with, the basic anatomy of the knee is discussed, followed by a short description of procedures performed on the knee joint, their indicators, suitability for various patient groups, and advantages/disadvantages relative to each other. Having established that arthroplasty is a relevant treatment for knee joint degradation, the chapter continues by discussing the design ethos of joint-type simulators, this being the primary attempt at meeting the first objective outlined in Chapter 1. Finally, a quick overview of servo-pneumatic modelling is presented as an introduction to the later chapters.

2.1 Knee Joint Anatomy

Palastanga *et al.* (2002) describes the knee as the largest and one of the most complex joints in the human body. Being a bicondylar hinge joint, with articulation occurring between the condyles of the femur and tibia, and with the patella located anteriorly, stability of the knee joint is maintained by the interaction between the collateral and cruciate ligaments. Menisci, located between the femur and the tibia, facilitates meshing, weight transfer, shock absorption and lubrication. The articulating surfaces of the femur, tibia and patella are covered with cartilage, minimising friction during motion. Lubrication and nourishment are provided to the aforementioned cartilage by the fluid that the synovial membrane, which encases the joint, secretes. Figure 2.1 illustrates the anatomy of the knee, while movement thereof with respect to relevant reference frames is described in Appedix A.

2.2 Osteotomy and Arthroplasty of the Knee

Knee joint degradation may be due to a number of causes such as osteoarthritis, posttraumatic arthritis and rheumatoid arthritis, which invariably cause

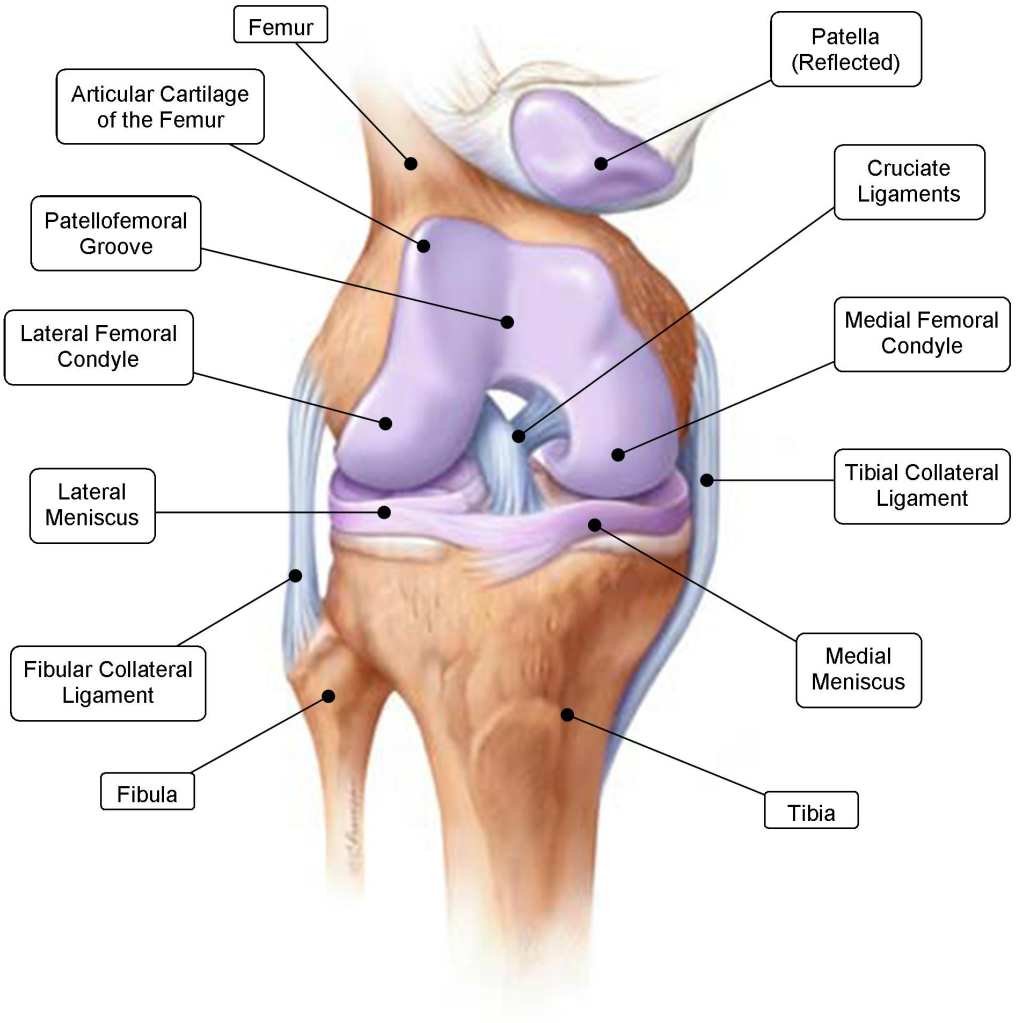

Figure 2.1: Anatomy of the Knee (Illustration: 2001 Christy Krames)

pain and may result in loss of function in the affected joint. Surgical treatment options intended to alleviate symptoms associated with an arthritic knee include, among others, procedures such as arthroscopy, high tibial osteotomy (HTO), unicondylar knee arthroplasty (UKA), and total knee arthroplasty (TKA).

Arthroscopy is intended to treat various conditions pertaining to the articular cartilage and cruciate ligaments. It is a minimally invasive procedure in which an arthroscope is used in order to provide visual feedback. The joint is distended using irrigation fluid, thereby creating room in which to execute the procedure. Arthroscopy is commonly employed to relieve pain due to osteoarthritis of the knee, although uncertainty remains concerning the physiological basis for success of such a procedure (Moseley *et al.*, 2002).

HTO refers to a surgical procedure in which a section of the proximal

surface of the tibia is cut and repositioned in order to change its alignment. This has traditionally been intended to treat medial osteoarthritis in younger, active men (Emerton and Burton, 2001). It has, however, been shown that unicompartmental knee implants perform better in terms of function and survival within comparable age groups (Weale and Newman, 1994), and that it is easier to revise a UKA to a TKA than it is to revise a HTO to a TKA (Jackson *et al.*, 1994).

UKA is a procedure in which a unicondylar knee prosthesis is implanted, replacing the corresponding articular surfaces of a single condyle of the femur and tibia, as shown in Figure 2.2. It has gained in popularity primarily as a result of the development of the mini-incision technique in recent years (Bert, 2005). When compared to TKA, UKA, in conjunction with the mini-incision technique, has the benefits of allowing for the preservation of bone stock, affecting less damage to soft tissue, a faster rate of recovery, a range of motion that is closer to that of a healthy knee, and decreased costs (Callahan *et al.*, 1995; Newman *et al.*, 1998; Price *et al.*, 2001; Shakespeare and Jeffcote, 2003). Current accepted indications for UKA include localised symptoms of arthritis in either the medial or lateral compartment of the knee that warrants TKA, while absolute contraindications include inflammatory arthropathy, previous HTO, and non-localized pain (Bert, 2005; Emerton and Burton, 2001).

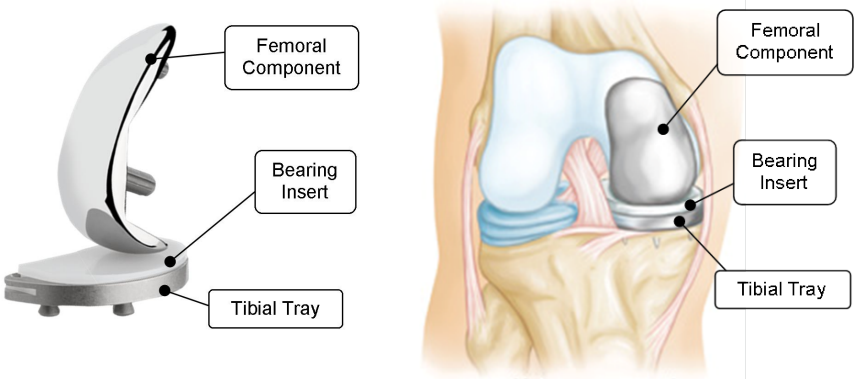

(a) Zimmer High-Flex Knee System (Photo: Zimmer, Inc)

(b) *In-Vivo* (Illustration: American Academy of Orthopaedic Surgeons (1995))

Figure 2.2: Unicompartmental Knee Implant

TKA describes a procedure during which a prosthesis, as illustrated in Figure 2.3, is implanted that replaces both the medial and lateral articulating surfaces of the femur and tibia, as well as the cartilage of the patellofemoral groove, with optional patellar resurfacing. Depending on the design of the implant, either one, or both, of the cruciate ligaments may be retained. Indications for TKA include severe non-localised knee pain, osteoarthritis or rheumatoid arthritis, and joint instability (Mancuso *et al.*, 1996). Even though it is

suggested selection for UKAs receive precedence over TKAs within younger patients, as prosthetic implants are more likely to fail within the lifetime of said patient group (Weale *et al.*, 2001) and revision of TKAs do not compare favourably with revision of UKAs to TKAs (Saldanha *et al.*, 2007), the ratio of primary UKAs to TKAs performed, based on data compiled and collected by the Lund University Hospital, Department of Orthopedics (2010) over the past decade, appears to be much in the favour of TKAs.

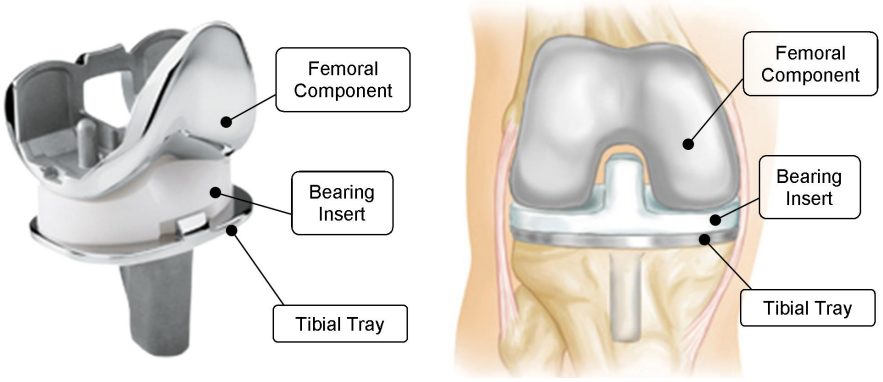

(a) Zimmer LPS Flex Mobile Knee (Photo: Zimmer, Inc)

(b) *In-Vivo* (Illustration: American Academy of Orthopaedic Surgeons (1995))

Figure 2.3: Total Knee Implant

Variations on the knee arthroscopy theme are not limited to replacing either one or all three articular compartments of the knee, as in the cases of UKA and TKA, respectively. Bi-unicondylar arthroplasties employ two unicondylar knee implants to replace the corresponding articular surfaces of both the lateral and medial condyles of the femur and tibia, whereas bicompartmental knee implants replace either the medial or lateral condyle's articular surface, as well as that of the patellofemoral groove. Such prostheses are intended to facilitate patient-specific treatment options, thereby potentially minimising sacrifice of healthy tissue during an arthroplasty procedure.

2.3 Joint-Type Simulator Design

As per DesJardins *et al.* (2000), quantifiable measures of an implant's expected use is required to further its design. Evaluation of implants *in-vitro* has the advantage of facilitating the measurement and control of specific variables to a greater degree than easily possible *in-vivo* (Moran, 2005), thereby assisting the identification and investigation of such measures.

This section therefore attempts to provide an overview of the design ethos of joint-type knee simulator design, as such a device has been deemed most

appropriate for investigating the measure of interest, namely wear. For a discussion regarding different types of *in-vitro* knee evaluation devices and their uses as reported in literature, refer to Appendix B.

2.3.1 Coordinate System

The design of joint-type simulators are centred around the focus of applying forces and motions to the implant in terms of a coordinate system that facilitates adequate description of *in-vivo* knee joint kinetics and kinematics, while disregarding the anatomy of the lower limb as a whole.

One such coordinate system, as proposed by Grood and Suntay (1983), has indeed been adopted by the ISO 14243 standards, allowing measurement of movement of a three dimensional system along six degrees of freedom, namely three translations and three rotations. As per Figure 2.4, the axes about which movement occurs are defined such that two are fixed within the femur and tibia, on the flexion/extension (F/E) axis and tibial long or mechanical axis respectively, and the third is defined as being perpendicular to both the fixed axes, resulting in what is known as a 'floating' axis. Advantages of this coordinate system are that the joint displacements are independent of the order in which translations and rotations occur, and that it is defined in such a way as to represent physiological movement of the joint, as per Table 2.1.

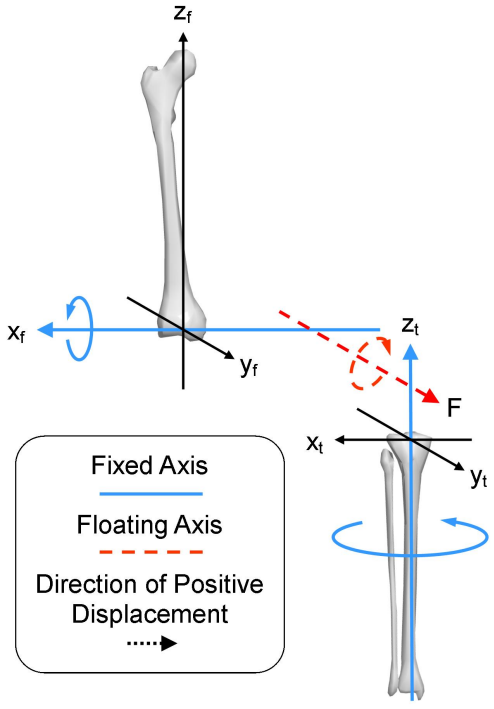

Figure 2.4: Right Knee Coordinate System (Adapted from Grood and Suntay (1983))

Table 2.1: Clinical Description of Knee Joint Movement (Grood and Suntay, 1983)

		Movement Relevant to Axis	
Axis	**Description**	**Translation**	**Rotation**
x_F	Femoral Fixed Axis	Medial/Lateral	Flexion/Extension
F	Floating Axis	Anterior/Posterior	Varus/Valgus
z_T	Tibial Fixed Axis	Distraction/Compression	Internal/External

The ISO 14243 standards detail procedures to determine the location of the fixed axes, also defining the relevant reference position, of a total knee implant. Accurate positioning of an implant relative to the axes along which actuation occurs is of critical importance in ensuring valid reproduction of *in-vivo* conditions, and the design of a joint-type knee wear simulator should facilitate such positioning. Figure 2.5 shows a single station of a joint-type knee wear simulator, illustrating actuation of an implant along the relevant axes.

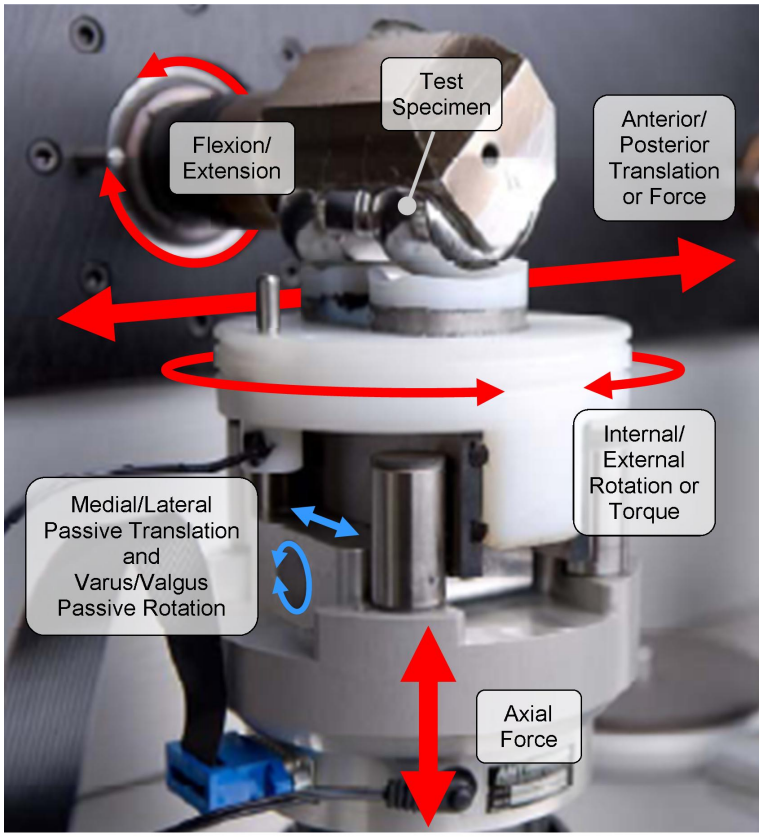

Figure 2.5: Joint-Type Simulator Loads and Motions (Photo: AMTI Force and Motion (2011)

2.3.2 Control Methodology

Joint-type simulators apply either load or displacement control, although neither is implemented using 'purely' load or displacement input parameters. As per the ISO 14243 standards, both methodologies apply axial load and F/E rotation as primary inputs. The distinction is achieved by additionally implementing secondary profiles such as either anterior/posterior (A/P) load and internal/external (I/E) torque, or A/P translation and I/E rotation. Actuation of such secondary inputs is necessary to adequately simulate implant wear, as both linear and rotational sliding have been identified as contributing factors (Blunn *et al.*, 1991; McEwen *et al.*, 2005; Wasielewski *et al.*, 1994). Figure 2.6 shows the various ISO input profiles.

Walker *et al.* (1997) initially adapted input variables for a load controlled quasi-static knee simulator from the work of Morrison (1969; 1970). A methodology for the testing of TKR wear as detailed in the then draft ISO 14243-1 load control standard, based on the same source, was later published (Walker *et al.*, 2000), although the finalised form of the load profiles contained in the ISO 14243-1:2002 first appears in work by DesJardins *et al.* (2000). *In-vitro* TKR wear achieved in simulators based on ISO load control has been shown to correspond well with *in-vivo* wear results reported in retrieval studies (Walker *et al.*, 2000). Furthermore, despite the fact that Morrison not only applied simplifying assumptions to determine the kinetics of the knee joint, but also did not study subjects with implants, it has been found that the ISO load profiles induce *in-vitro* joint kinematics statistically similar to those of active TKR subjects (DesJardins *et al.*, 2007).

Furthering the premise that implant wear is largely a result of the relative kinematics between the joint's solid bodies (Walker *et al.*, 2000), some studies directly effect displacement control towards this end (Affatato *et al.*, 2008; Harman *et al.*, 2010). Though a standardised protocol for displacement control simulators, the ISO 14243-3:2004 standard, has been developed, considerable controversy exists regarding the use of generalised displacement profiles. This is due to concerns such as abnormal motions being forced on a particular implant design (Barnett *et al.*, 2002) as its kinematic response is not inherently determined in this case by the geometry thereof (Walker *et al.*, 2000), and the effect implant conformity may have on loads applied by a simulator in order to achieve said motions (DesJardins *et al.*, 2007). Recent studies also found significant differences between not only the motions exhibited by TKR subjects *in-vivo* and the ISO displacement profiles (Ngai and Wimmer, 2009), but also between the kinematics of cadaveric knees, which were tested in joint-type simulators under ISO load control, and the displacement profiles (Sutton *et al.*, 2010). Such profiles might, however, be more appropriately applied if tailored to suit individual implant designs - something which is inherently difficult if a new design, or one for which there is no data available, is being investigated (Houtem *et al.*, 2006).

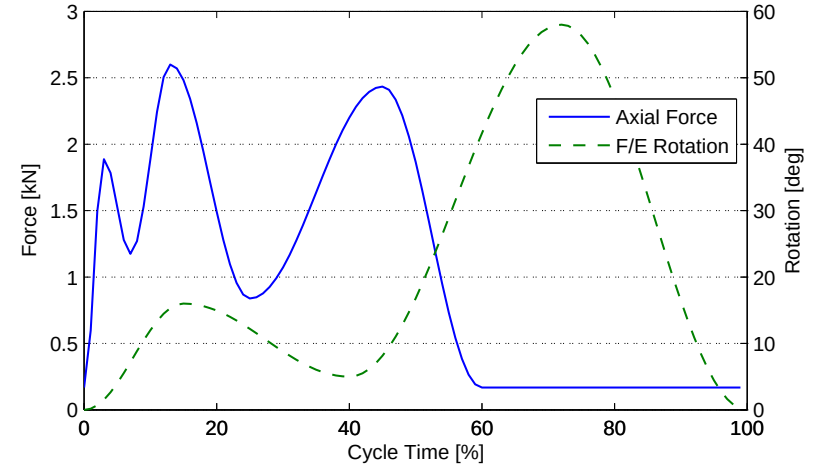

(a) Primary Profiles

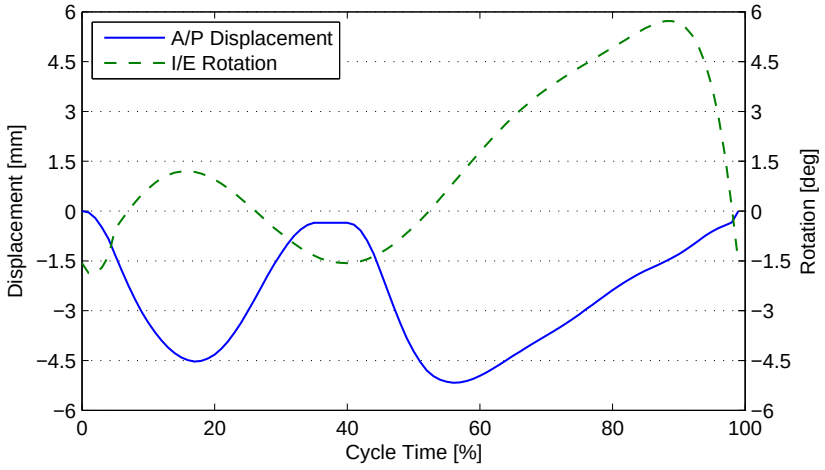

(b) Secondary Displacement Profiles

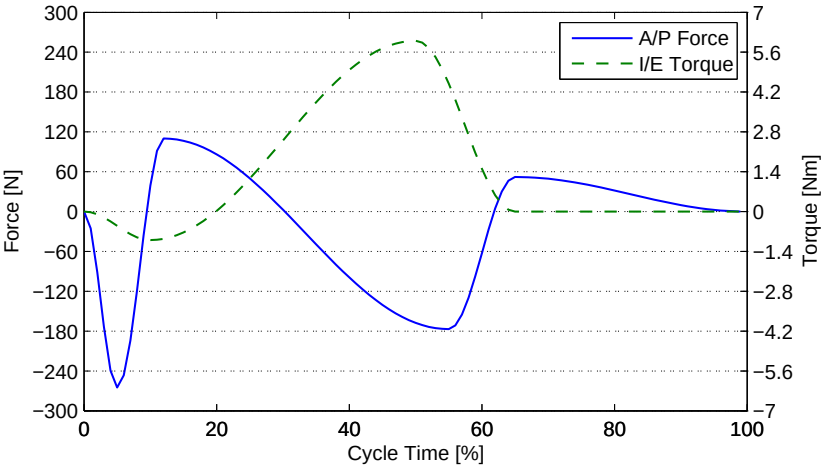

(c) Secondary Load Profiles

Figure 2.6: ISO Profiles (International Organization for Standardization)

Design of knee simulators, therefore, must not only ensure adequate actuation of motions and loads as specified by the requirements of the intended study, but must facilitate the evaluation and verification of actual joint kinetics and kinematics in order to aid validation of said study's methodology (DesJardins *et al.*, 2007). Practically, this dual design focus in terms of specific actuation inputs may firstly be achieved by enforcing operational tolerances on the relevant profiles, such as in the case of wear studies conducted according to ISO protocol, $\pm 5\%$ of the maximum magnitude value. Secondly, issues regarding study methodology may be addressed by incorporating 'redundant' sensory outputs - redundant, at least, from a control perspective. This would serve to aid the comparison of both *in-vitro* loads and motions to physiological conditions, regardless of the control methodology implemented.

2.3.3 Soft-Tissue Modelling

While displacement controlled studies are complicated by the difficulty associated with determining and actuating appropriate input profiles, the load control methodology requires the simulation of the restraining effects of soft tissue (Walker *et al.*, 1997). It should be noted that soft tissue restraints are a non-issue with displacement control strategies, as implant motions are inherently restricted by the controller itself.

Walker *et al.* (2000) originally employed linear springs to simulate the restraining effects of the cruciate ligaments on movement in the A/P translation and I/E rotation directions. The values for the coefficients of stiffness for these springs were based on work by, among others, Fukubayashi *et al.* (1982) and Markolf *et al.* (1981), and were later employed in a validation study of the load control methodology (DesJardins *et al.*, 2007). Although the exact values for the coefficients of stiffness differ, the ISO 14243-1:2002 standard prescribes a similar methodology for implementing soft tissue restraints.

In order to verify the use of linear springs during wear simulation, Houtem *et al.* (2006) mounted cadaveric knees in a joint-type machine and actuated them according to the ISO gait cycle, comparing the resulting motions with the cruciate ligaments intact, cut, and with different combinations of linear springs. It was found that no single combination of linear springs adequately restored normal kinematics to the knee after the cruciates were cut for both the A/P and I/E motions, and a compromise was suggested using intermediate spring stiffness coefficients, although not evaluated. Note, however, should be taken that the Instron/Stanmore knee simulator employed in said study uses a single set of springs to affect restraint on both A/P translation and I/E rotation, as shown in Figure 2.7, resulting in coupling thereof (Kretzer *et al.*, 2010). The conclusions reached, therefore, may not be relevant to a machine that restrains such secondary motions separately.

The use of linear elastic components to model restraint during *in-vitro* simulation studies may be additionally undermined by the inherent non-linear

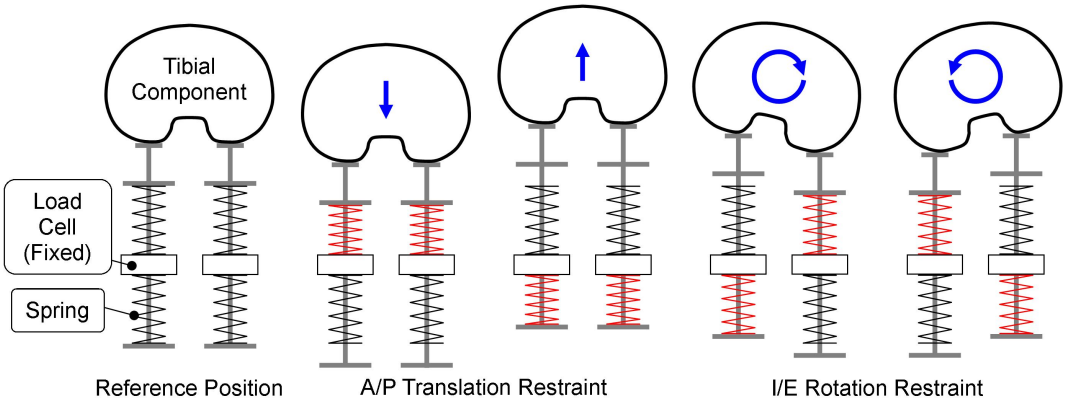

Figure 2.7: Instron/Stanmore Knee Simulator Restraint System Schematic

behaviour of soft tissue *in-vivo*. Haider *et al.* (2006) attempts to better model this non-linearity by mounting elastic components with a gap such that movement along the relevant secondary input's axis may initially occur unrestricted. This is intended to approximate the near-zero elasticity of soft tissue about the neutral position. The ISO 14243-1:2009 standard indeed also prescribes such a configuration. Furthermore, both the previously mentioned study and the latest load control standard details lower coefficients of stiffness for linear elastic elements mounted along actuation directions in which the relevant acting cruciate ligament would be absent *in-vivo*, as resection may be required by the specific implant's design. Figure 2.8 illustrates the behaviour of the ISO 14243-1:2002 and 2009 A/P soft tissue restraint models, with the *in-vivo* data presented by Fukubayashi *et al.* (1982) shown for comparison.

Virtual soft tissue restraint models, such as that developed by White *et al.* (2006) and later also implemented by Kretzer *et al.* (2010), have the potential to not only simplify the mechanical design of a load controlled wear simulator by bypassing the need for complex elastic element arrangements, but also to facilitate the implementation of more anatomically correct models. While successful implementation of such models have been described by the previously mentioned authors, comparative studies demonstrating the usefulness of virtual tissue simulation in aiding the accurate reproduction of physiological implant wear *in-vitro* are, to the best of the author's knowledge, still lacking at present.

A further difficulty with soft tissue restraint modelling which could potentially be overcome by in silico implementation thereof is the *in-vivo* variation of stiffness with the angle of flexion. Figure 2.9 shows the variation of A/P laxity for cruciate retaining knees with F/E angle, based on the data presented by Fukubayashi *et al.* (1982). The behaviour of the relevant model detailed in ISO 14243-1:2009 is superimposed for reference.

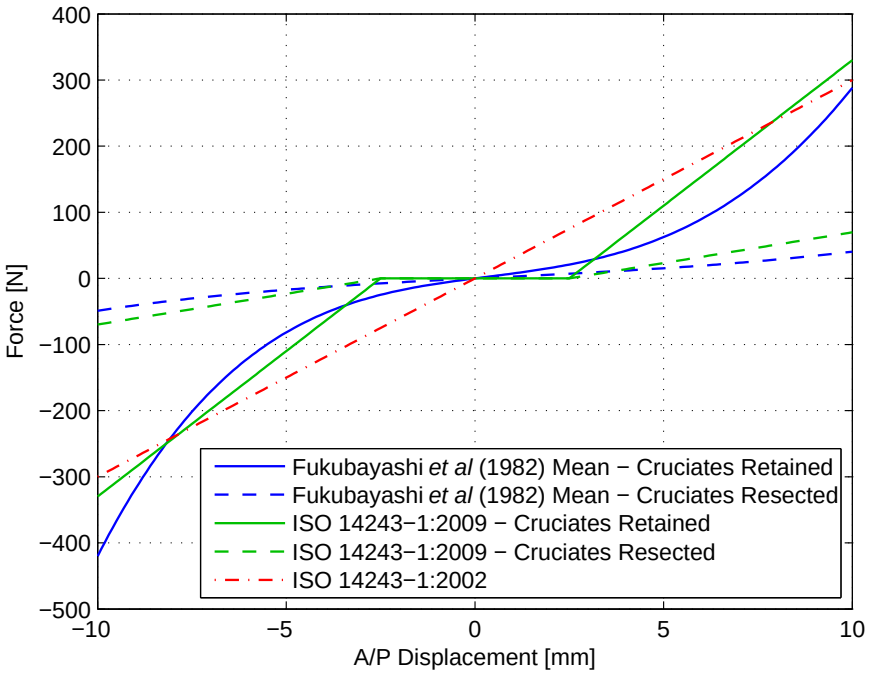

Figure 2.8: Effect of Cruciate Resection on Soft Tissue Restraint

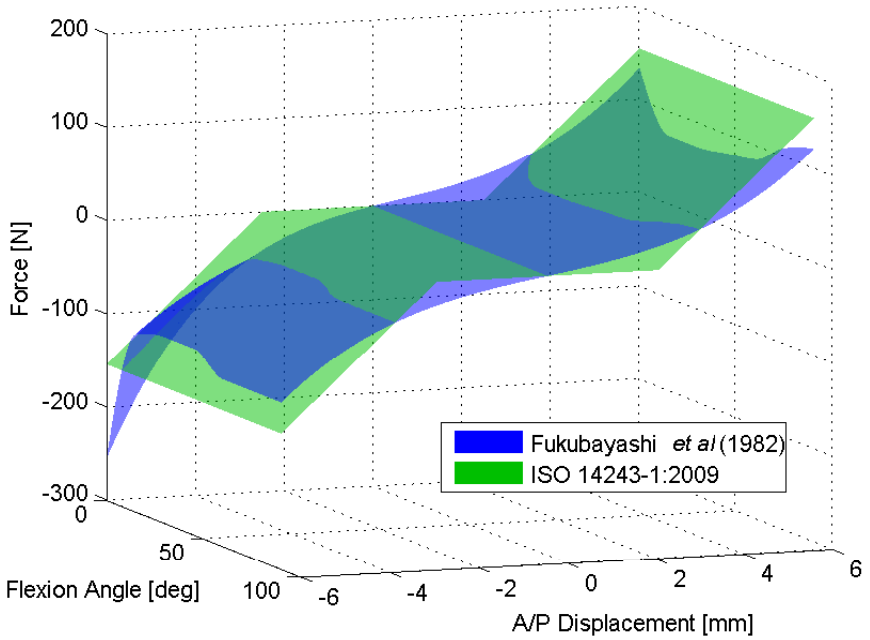

Figure 2.9: Effect of Flexion on Soft Tissue Restraint

Soft tissue characteristics may additionally differ not only between patients, but also pre- and post-implantation (Houtem *et al.*, 2006), which could in fact

be the case for a number of input parameters of any *in-vitro* simulation. Therefore, in light of such factors adding uncertainty with regards to the usefulness of available data, the potential value of increasing a system's complexity by modelling variation of soft tissue restraint with the F/E angle appears questionable if it would interfere with reasonable progress. Indeed, the author is not aware of any attempts to model the variance of laxity with F/E rotation.

2.3.4 Actuation Method

As per Bishop (2002), actuators have the purpose of influencing a system being controlled so as to achieve the desired action by converting some primary source of energy to mechanical motion. Actuators are mainly classified as either electromechanical, hydraulic or pneumatic, the distinction made based on the type of energy source employed. Needless to say, electric power serves as the source for electromechanical actuators, whereas the fluid actuators are powered by hydraulic fluid or compressed gas, respectively. Commercially available joint-type prosthesis wear simulators employ either one or a combination of the aforementioned types of actuators, and therefore other types of energy, while available, will not be considered here.

Electromechanical actuators not only has a lower power to weight ratio when compared to fluid power actuators (Ali *et al.*, 2009), but also requires the conversion of rotary motion to linear translation for certain applications, whereas fluid power actuators allow linear translation to be carried out directly (Bishop, 2002). While rotary electromechanical actuators do allow greater maximal rotary speeds in comparison with hydraulic motors, such motors typically fall short of the maximum power output achievable by their comparable hydraulic counterparts (Janocha, 2004).

The different fluid mediums employed further results in distinct differences between hydraulic and pneumatic actuators. Pneumatic actuators tend to be cheaper, easier to handle and maintain and, if compressed air is used as a medium, negates the need to collect exhaust (Ali *et al.*, 2009). Actuators making use of hydraulic fluid, on the other hand, typically operate at much higher pressures (Janocha, 2004) and are less susceptible to non-linearities introduced by the compressibility of the medium and friction.

Adequate frequency response is especially important in order to ensure proper actuation of the high force peak at initial heal strike, and Walker *et al.* (1997) suggests only using pneumatic actuators for systems with an overall frequency of less than 2 Hz. Indeed, Barnett *et al.* (2002) was not able to reproduce said signal component on their pneumatically actuated machine. Burgess *et al.* (1997) also claims superior response and fine closed-loop control for servo-hydraulic systems.

Another important consideration during the design of joint-type simulators, and especially during actuator selection, is fatigue. When performing wear tests, 30 million simulated gait cycles have been proposed as an equivalent to

10 to 20 years of *in-vivo* use (Seedhom and Wallbridge, 1985), which may take months to complete, even at accelerated rates. Many simulators also have a number of testing stations that allow implants to be tested simultaneously, thereby facilitating the acquisition of statistically significant data, and saving time. Considerations such as whether such stations should be individually actuated or not, therefore, also comes into play.

2.3.5 Environmental Conditioning

In order to reproduce not only physiologically similar wear rates, but also the mechanisms by which said wear occurs, the implant must be enclosed in an environment that mimics *in-vivo* conditions during testing, specifically those arising from the effects of fluid secreted by the synovial membrane encapsulating the joint. This is achieved by submersing the articular surfaces of the implant within a suitable lubricant while maintaining the temperature thereof at approximately 37°C, as shown in Figure 2.10.

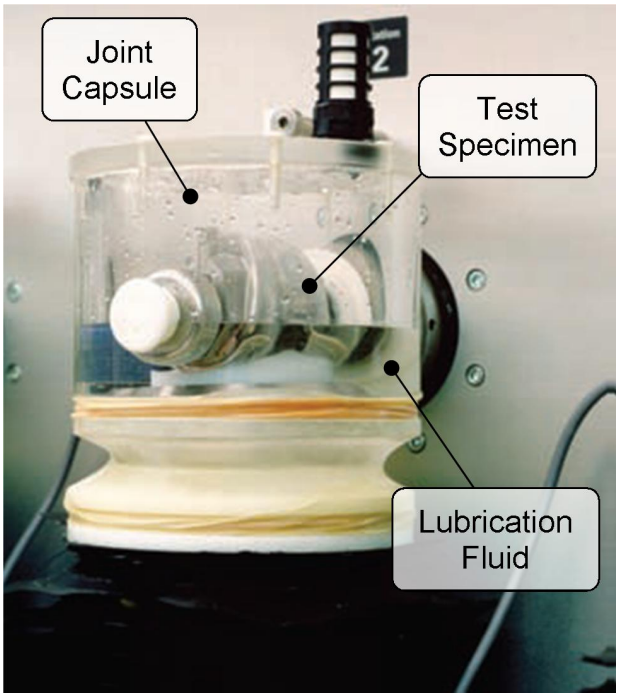

Figure 2.10: Encapsulated Knee Implant (Photo: MTS Systems)

According to Brown and Clarke (2006), since synovial fluid is only found in very small quantities *in-vivo*, this would necessitate a large number of patient donations due to the comparatively much greater fluid requirements of a wear simulator, and therefore a substitute must be used. Such 'pseudo-synovial' fluids include de-ionized water, mineral oil, gelatin solutions, saline, bovine or calf

serum, plasma and various artificial lubricants. It has, furthermore, become apparent that in order to reproduce *in-vivo* wear mechanisms, any lubricant used *in-vitro* must contain proteins similar to those found within synovial fluid (Saikko, 2003). Bovine serum, which comes closest to reproducing *in-vivo* results, is therefore most commonly used (Liao *et al.*, 1999). There is, though, at this stage no clear consensus concerning the optimal protein concentration, resulting in bovine serum being diluted to various degrees for different studies (Saikko, 2003).

Employing bovine serum during long term wear tests is not without additional difficulties. In terms of the design of the chamber encapsulating the joint, not only must said chamber minimise the fluid volume used due to the high costs associated with obtaining and processing the serum, the chamber must also remain inert, corrosion resistant and facilitate cleaning (Burgess *et al.*, 1997). The serum itself is susceptible to degradation and bacterial contamination (Brown and Clarke, 2006), necessitating fluid replacement after a fixed number of wear cycles.

Finally, to account for the effects of absorption, soak control specimens are employed, as per good scientific practice and the ISO 14243 standard. These are implants identical to those undergoing wear testing that are submersed within lubrication fluid at the same temperature for the duration of the test. Such soak control stations are either passive, meaning no load is applied, or active, in which case axial load only is applied. Wear may therefore be more accurately determined by comparing the test specimens to the soak control specimens.

2.3.6 Simulator Comparison

Due to the advanced nature of the field of *in-vitro* simulation, various companies provide solutions for knee implant wear testing. Listed in Tables 2.2 and 2.3 are some of the most prominent commercially available joint-type simulators, with their various features outlined for comparison with each other and for evaluation against the previously discussed topics, where available. The aim is to provide a broad overview of the current state of the art.

Table 2.2: Knee Wear Simulator Comparison - Part 1

	Simulator			
Feature	ADL Knee Simulator	ADL Force Five	Instron Stanmore Knee Simulator	Shore Western Knee Simulator
Company	AMTI Force and Motion	AMTI Force and Motion	Instron	Shore Western Manufacturing
Actuation	Servo-hydraulic	Servo-hydraulic	F/E electromechanical, servo-pneumatic otherwise	Servo-hydraulic
Test Stations	Two banks of three, motion-linked (six total)	Single	Four, motion-linked	Two banks of three, independent (six total)
Controlled DOF	AxF, F/E, A/P, I/E	AxF, F/E, A/P, I/E	AxF, F/E, A/P, I/E	AxF, F/E, A/P, I/E
Free DOF	V/V, M/L	V/V, M/L	V/V, M/L	V/V, M/L
Fixed DOF	None	None	None	None
Control Method	Load or displacement	Load or displacement	Load	Load or displacement
Measured DOF: Load	All six DOF	All six DOF	AxF, A/P, I/E	Customer specific
Measured DOF: Displacement	AxF, F/E, A/P, I/E	F/E, A/P, I/E	F/E, A/P, I/E	Customer specific
Cycle Frequency	2 Hz	2 Hz	1 Hz	2 Hz
Soft Tissue Modelling	In silico	In silico	Linear spring arrangement	In silico
Soak Stations	Four active	None	None	Six active
Suitable Lubrication Fluids	Bovine serum, saline solution, water	Bovine serum, saline solution, water	Bovine serum	Bovine serum, saline solution, water
Fluid Temp	Controlled	Controlled	Controlled	Controlled
Comments	Non-ISO axis setup: Axial load is not distributed medially	Hip implant wear may also be simulated	Specifications determined from literature	Adjustable M/L pivot point

Table 2.3: Knee Wear Simulator Comparison - Part 2

Feature	Simulator			
	Bionix Knee Wear Simulator	Bionix Knee Wear Subsystem	ProSim Pneumatic Knee Simulator	ProSim Electromechanical Knee Simulator
Company	MTS Systems Corporation	MTS Systems Corporation	Simulation Solutions	Simulation Solutions
Actuation	Servo-hydraulic	Servo-hydraulic	F/E electromechanical, servo-pneumatic otherwise	Electromechanical
Test Stations	Two banks of three, motion-linked (six total)	Single	Two banks of three, independent (six total)	Two banks of three, independent (six total)
Controlled DOF	AxF, F/E, A/P, I/E	AxF, F/E, A/P, I/E	AxF, F/E, A/P, I/E	AxF, F/E, A/P, I/E
Free DOF	V/V, M/L	V/V, M/L	V/V	V/V
Fixed DOF	None	None	M/L	M/L
Control Method	Load or displacement	Load or displacement	Load or displacement	Load or displacement
Measured DOF: Load	AxF, A/P, I/E	AxF, A/P, I/E	AxF, A/P, I/E	AxF, A/P, I/E
Measured DOF: Displacement	F/E, A/P, I/E	F/E, A/P, I/E	F/E, A/P, I/E	F/E, A/P, I/E
Cycle Frequency	2 Hz	1 Hz	1.5 Hz	1.5 Hz
Soft Tissue Modelling	In silico	In silico	Linear spring arrangement	In silico
Soak Stations	Standalone active partner device	None	Available on request	Six active
Suitable Lubrication Fluids	Bovine serum	Bovine serum	Bovine serum	Bovine serum
Fluid Temp	Controlled	Controlled	Not specified	Controlled
Comments	Separate fixtures for ISO 14243 testing required	Designed for use with Bionix load frame and FlexTest controller	Unable to perform ISO compliant tests	N/A

2.4 Servo-Pneumatic Component Modelling

Traditionally, pneumatic actuators were primarily used in process control applications requiring displacement of loads to its end positions (Richer and Hurmuzlu, 2000). Such devices' applicability to the automation of manufacturing and distribution systems stems from their relatively high speed, low cost, high power-to-weight ratio and use of a non-pollutant energy medium. Prior to the development of sophisticated non-linear control techniques and adequate electronic hardware, however, the non-linearities present within a pneumatic circuit due to the compressibility of air, valve behaviour and piston-seal friction prevented their use in applications requiring high accuracy. Such characteristics render classical control techniques unable to reproduce the comparatively good results achievable with other 'well behaved' actuators such as electromechanical devices (Carneiro and de Almeida, 2006*a*).

The past decades have, however, witnessed much progress concerning non-linear control theory and application, and, not surprisingly, accompanying interest in the use of pneumatic actuators in precision applications. Presented in the following paragraphs, therefore, is a cursory introduction to literature concerning theoretical and, in certain cases, empirical models that describe said non-linear characteristics of a pneumatic circuit's components; namely the actuator, the control valve, and the connection tubing and fittings.

Concerning pneumatic cylinders, higher order theoretical models describing the heat transfer and rate of pressure change within the chambers are unsuited to on-line control applications due to their computational expense (Carneiro and de Almeida, 2006*b*). Therefore, many studies implement reduced order models, assuming either adiabatic, isothermal or tunable polytropic processes to simplify the equations. As per Carneiro and de Almeida (2006*b*), further simplification is often achieved by assuming the chamber temperature remains constant. Such reduced order models are both sufficiently accurate and computationally inexpensive to warrant on-line implementation thereof.

Another consideration relevant to pneumatic actuators is friction due to the piston and rod's seals. Friction is considered one of the most important non-linearities within the actuator, affecting all regimes of operation (Nouri *et al.*, 2000). Modelling thereof is difficult, to say the least, as no universal approach exists - model choice is based on inspection of the data, which in turn is highly susceptible to variations within the operating conditions (Harris *et al.*, 2011). This has resulted in earlier studies neglecting friction entirely which, consequently, had an adverse effect on tracking performance (Richer and Hurmuzlu, 2000). Alternatively, friction within pneumatic cylinders has often been modelled via quasi-static approaches (Richer and Hurmuzlu, 2000; Andrighetto *et al.*, 2006; Harris *et al.*, 2011), without taking into account effects such as frictional lag, dwell time and varying static friction. While a quasi-static approach is sufficient for applications which vary slowly with time, more complex models that address said dynamic parameters are indeed pre-

sented in literature. These include the Seven Parameter (Armstrong-Hélouvry *et al.*, 1994) and Generalised Maxwell Slip (GMS) (Lampaert *et al.*, 2003) models.

Servo-pneumatic valve modelling has seen considerable development since St. Venant and Wantzel (1839) first derived the relation for mass flow through an ideal, well-rounded orifice. Subsequent work constituted the inclusion of a discharge coefficient to adapt said equations for flow through thin, sharp edged orifices, as typically found within commercially available valves (Beater, 2007). Furthermore, the subsonic portion of the flow function which describes non-linear mass flow through the orifice has been approximated by a quarter section of an ellipse, as per the ISO 6358:1989(E) standard. This facilitates modelling of a concatenated series of orifices, which is in general a better approximation of most commercially available valves (Beater, 2007). Various authors modify the flow function even further by including additional parameters (Nouri *et al.*, 2000; Harris *et al.*, 2011). Characteristics such as the cracking pressure ratio, namely the pressure ratio at which a check valve starts to operate, are thus accounted for.

The mass flow model as described previously is derived for a constant orifice opening, yet it is applied successfully to proportional valves in numerous studies with no apparent consideration for the effects of varying opening areas (Richer and Hurmuzlu, 2000; Bubert, 2009; Nouri *et al.*, 2000). The only consideration relating to the servo-valve's dynamic behaviour found in literature is the effect of the mechanism actuating its spool, though even this is often neglected due to the comparatively low bandwidth achievable by the system as a whole (Carneiro and de Almeida, 2006*a*).

Finally, a number of models relating to flow through connection tubing and similar restrictions may be found in literature (Richer and Hurmuzlu, 2000; Beater, 2007; Bubert, 2009). While the modified orifice mass flow equation is particularly suited to account for the cascaded effects of a number of restrictions in series (Harris *et al.*, 2011), separate modelling of connection tubing and other fittings would result in a more modular approach. This would serve to simplify adaptation of the model to real-world changes. Connection tube models are typically either static or transient (Beater, 2007), merely attenuating mass flow amplitude or additionally including time delay present within long lines (Richer and Hurmuzlu, 2000). Both these effects, however, are negligible within short elements.

Chapter 3

System Development Overview

The following chapter starts with an overview of the design of the simulator's mechanical, pneumatic and electronic subsystems, as well as the various safety precautions implemented. In each case, previous work is presented in short, with new work continued in greater detail thereafter, if applicable. This serves to familiarise the reader with the basic functioning of the simulator. Following this is a description of a versatile experimental setup upon which the various tests, as described here and within Chapter 4, may be performed. Presented afterwards is the hardware and software components of the test setup in general.

The work within this chapter is therefore aimed at satisfying, entirely or in part, the second, third and fourth objectives: designing and implementing electronic hardware, software and safety subsystems, gaining insight towards their suitability for application within the simulator as a whole, and preparation for performance evaluation and parameter investigation experiments.

3.1 Mechanical Subsystem

As previously mentioned, the design of the SU simulator has been completed as part of an undergraduate project (Van der Merwe, 2009). Figure 3.1 illustrates the functional assembly of the simulator, with the directions of actuation superimposed thereon.

Axial force and I/E actuation are applied along the same axis, as shown. In order to decouple rotation about the axis caused by the I/E actuator, a thrust bearing assembly is placed in series between the rotating portion of the shaft and the axial force actuator. Furthermore, translation along the shaft is negated with respect to the I/E actuator via a link equipped with rolling units, mounted between two opposing, parallel plates attached to said actuator's sled. A/P actuation is directed by mounting the upper portion of the functional assembly upon two parallel rails, and F/E rotation occurs about an axis corresponding to that of the implant itself. For a detailed description

of the design process, function and specifications of the simulator refer to the report by Van der Merwe (2009).

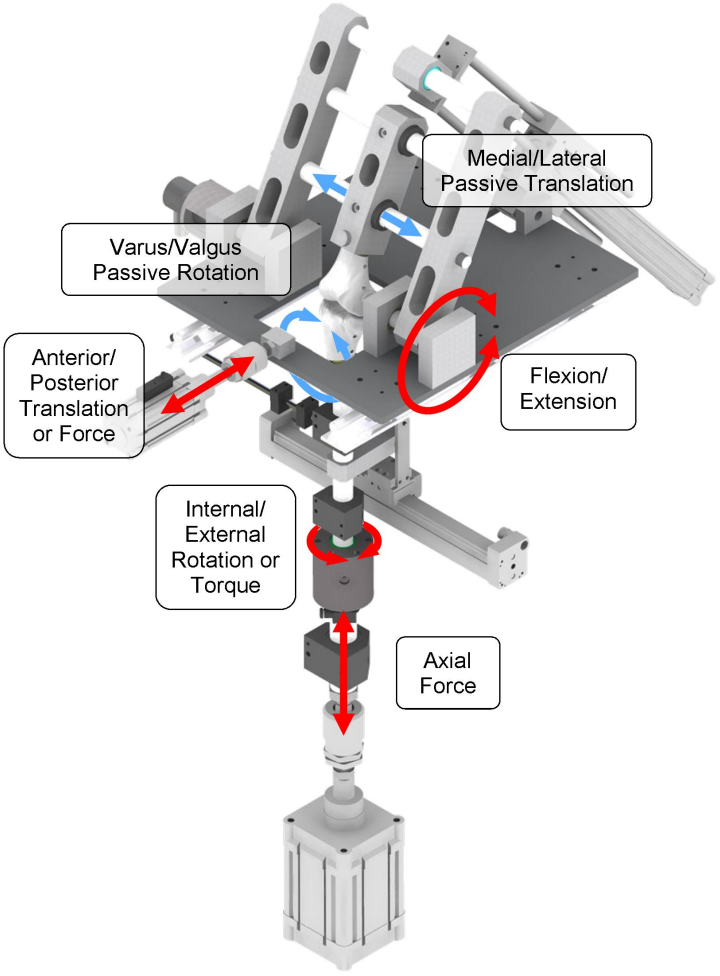

Figure 3.1: Functional Assembly

Before commencement of the current work, construction of the simulator has been commissioned and completed, to the extent that all mechanical components detailed by Van der Merwe (2009), as well as the pneumatic actuators, have been assembled as shown in Figure 3.2. Additionally, as a matter of interest, refer to Appendix C for a short description of the 'calibration knee', a device designed to facilitate investigation of the system's behaviour as a whole, as well as controller development.

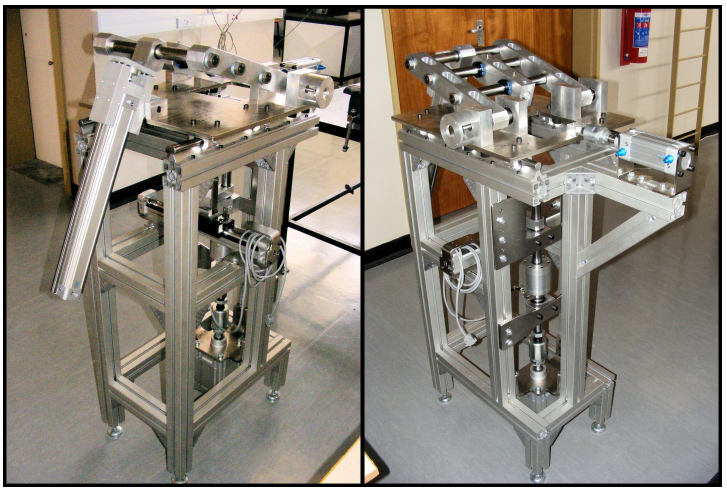

Figure 3.2: Mechanical Assembly

3.2 Pneumatic Subsystem

Pneumatic actuator selection was made based on the required maximum force to be effected by each actuator at a constant supply pressure of three bar. The unknown effects of cross-talk between the various actuators due to the geometry and friction of the implant being tested as well as supply pressure variations, supports the requirement of adequate safety factors. Hence, at a constant supply pressure of three bar, the smallest safety factor is just below 1.5, while at the upper design limit of ten bar, it approaches five. Proportional flow and pressure control valves were selected, as deemed appropriate, for each of the actuators.

Table 3.1 provides a cursory description of the main components, along with their part numbers to aid identification. Refer to the design report for greater detail concerning the development of the pneumatic subsystems, as well as the values of the parameters indicated in italics (Van der Merwe, 2009).

Table 3.1: Pneumatic Component Description

Part Number	Description
DNC-[*diameter*]-[*stroke*]-PPV-A	Pneumatic cylinder
DGC-[*diameter*]-[*stroke*]-KF-PPV-A	Rodless pneumatic cylinder
MPYE-5-3/8-010-B	Proportional directional flow control valve
MPPE-3-1/4-6-010-B	Proportional pressure regulator
U-[*thread*]	Silencer
MN1H-2-3/8-MS	Normally-closed solenoid valve
QH-3/8	Ball valve
OD [*outside diameter*]	Connecting tube

The overall pneumatic circuit, as shown in Figure 3.3, consists of four servo-pneumatic subcircuits, each including an actuator, a proportional control valve and the necessary connectors and tubing. This circuit has been adapted from the original design to include a normally closed solenoid-valve in series with the pneumatic supply to allow it to be cut off electronically. A further modification is the addition of ball valves in series with the supply of each of the separate subcircuits. This allows circuits that are inactive to be disconnected from the system.

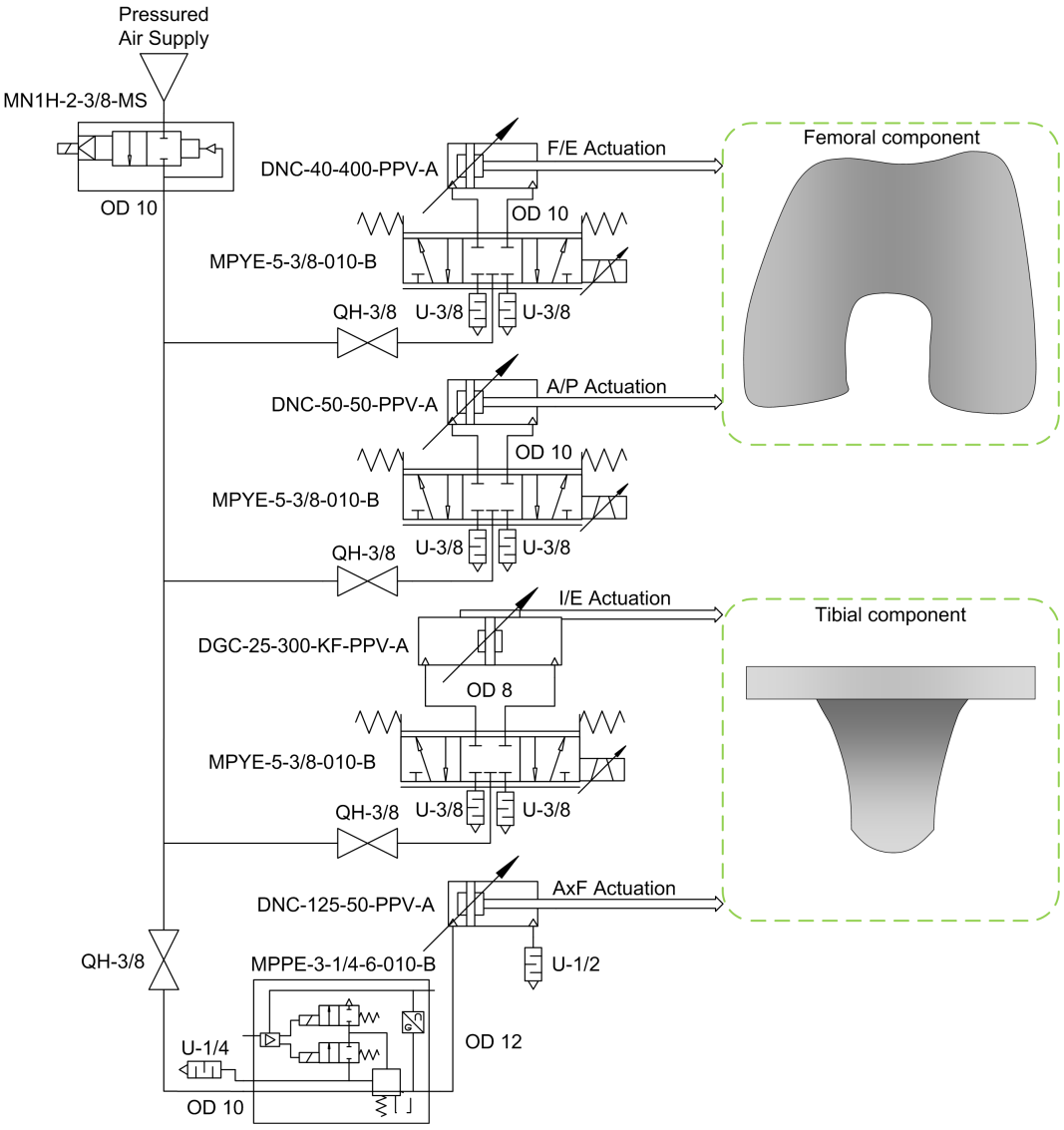

Figure 3.3: Pneumatic Circuit

3.3 Electronic Subsystems

The sensors listed in Table 3.2 were selected based on the required range of actuation and accuracy for each profile, as detailed by Van der Merwe (2009).

Table 3.2: Sensor Specification

Sensor	Supplier	Part Number	Actuation
Load Cell	HBM	U2B/5kN	Axial Force
Rotary Encoder	Hengstler	RI58-O/10000EQ.42RB	F/E Rotation
Position Sensor	Festo	SMAT-8E-S50-IU-M8	A/P Translation
LVDT	HBM	WA/200	I/E Rotation

The electronic control hardware has to be capable of adequately sampling the inputs of the sensors, both in terms of resolution and speed, while at the same time generating control inputs for the proportional valves based on the applicable setpoint. The original work utilised a Schneider Electric TSX Momentum PLC, in conjunction with Wonderware's InControl software in order to implement PID control in an attempt to actuate the A/P profile while the cylinder itself remained unloaded. Not only was PID control found to be unsuited to executing the profile, the setpoint, and hence the control signal, was evaluated and generated much slower than would be feasible during long term wear testing. Following this, a purpose built micro-controller-based system was briefly investigated, but discarded due to the amount of time required to construct, program and debug such a system.

Since the specific PLC and micro-controller based approaches have proved infeasible, it has been decided to use a commercially available data acquisition (DAQ) system for monitoring and control purposes. The system selected was National Instrument's cDAQ chassis, shown in Figure 3.4, which features interchangeable input/output (I/O) cards, enabling greater versatility in customising the system to suit the appropriate purpose. A further consideration for selecting this system was the availability of National Instrument's LabView software, a versatile graphics-based programming environment specifically designed for use with their products.

Table 3.3 lists the various I/O cards selected to match the sensor input and control signal output requirements outlined in the design report (Van der Merwe, 2009). Each I/O card is capable of sampling at a much higher rate than the required rate of 1 kHz. This value is a design variable based on the number of samples to generate and record per second stipulated for each ISO 14243 setpoint profile, which is one hundred, afterwards multiplied by ten in order to ensure that the design requirement is sufficiently larger than the Nyquist criterion. Finally, a solid-state relay card was included in order to

(a) NI cDAQ 9174 Chassis (b) NI I/O Cards

Figure 3.4: National Instruments DAQ (Photo: National Instruments™)

provide a means of executing software-based control over the power circuitry as a potential safeguard against malfunction.

Table 3.3: DAQ I/O Specification

Description	Part No	Channels	Operation	Rate	Range
Analogue In	NI 9205	16	16 Bit ADC	250 kHz	±10 V
Analogue Out	NI 9264	16	16 Bit DAC	25 kHz	±10 V
Digital I/O	NI 9401	8	5 V/TTL	30 MHz	5 V Logic
Relay	NI 9485	8	NO SSR	1 Hz	60 V DC

The cDAQ chassis is connected to a standard desktop computer (PC) via a USB cable. The system is such that the program in use is executed on the computer, while the DAQ system is merely the interface between the sensors and proportional valves. It has therefore been found that, while the cDAQ is capable of generating and sampling signals at the required rates, the cDAQ-to-PC system is unsuited to real-time control tasks as the time required for signal processing and data logging between each iteration tends to be longer than the minimum required sampling time. This was confirmed after consultation with National Instrument's technical personnel. The system as such was, however, more than capable of performing the tests outlined in the following chapters at suitable resolutions and sampling speeds without loss of data, as there was no need to perform real-time processing.

A possible solution that would ensure the execution of real-time monitoring and control would be to employ National Instruments' cRIO system. While similar in some respects to the cDAQ, it has been specifically designed for the purpose of real-time input/output (RIO). It achieves this by storing the program in its memory and executing it via dedicated on-board processors, while its connection to the computer merely serves as a user interface. The

I/O cards described previously are interchangeable between the cDAQ and cRIO systems.

3.4 Safety Precautions

In order to prevent damage to the system due to malfunctions, power is supplied to the various valves and sensors via a circuit controlled by a mechanical relay, as shown in Figure 3.5. The coil of the relay is excited once the start button is pressed, momentarily completing the circuit between the supply and ground. Once the circuit is completed, a normally open switch of the relay closes, maintaining contact even after the start button has been released. The circuit may be broken by pressing either of the stop or the latching emergency stop buttons, by causing the control software to open the solid state relay of the DAQ, or if supply to the mechanical relay's coil is interrupted, such as in the case of a power failure. A freewheeling diode is connected in parallel with the coil of the relay in order to negate the effects of the sudden voltage spike that occurs once an inductive load is disconnected from the source.

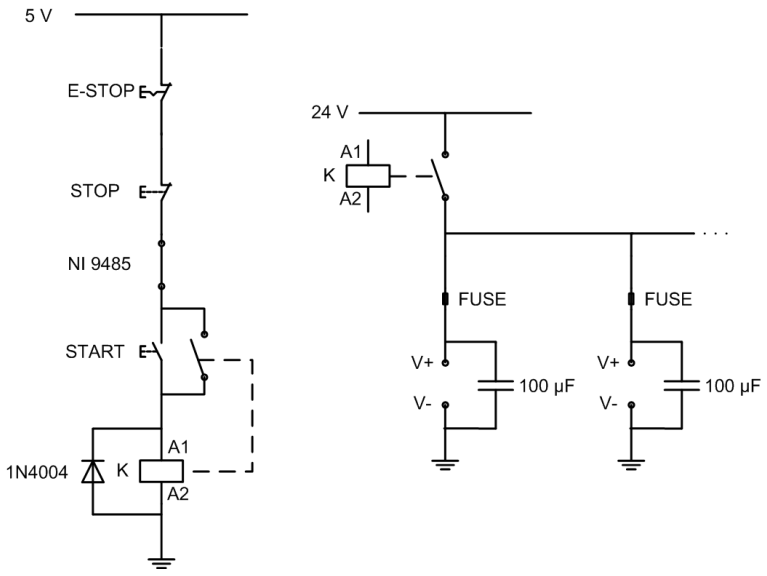

Figure 3.5: Safety Circuit

Once the relay's coil is excited, the circuit connecting the power supply to the various components is closed. In order to protect sensitive components such as the sensors from short circuits, fuse protection is provided for each pair of terminals. Finally, to negate the effects of sudden changes in supply voltage, such as when the relay coils are activated or deactivated, appropriately sized capacitors are connected in parallel with each pair of terminals.

As previously mentioned, a normally closed solenoid valve is connected in series with the pnuematic system's supply pressure. This enables the supply to be closed off should the valve's solenoid cease to be excited. By connecting the solenoid valve to the power terminals controlled via the mechanical relay described previously, the supply pressure will be closed off when any of the conditions that would cause the relay's coil to be disconnected occur, such as possible malfunction detected by the user or the software, power failure or the end of the test is reached.

3.5 Experimental Setup

Various experiments are to be conducted on the pneumatic circuits and their respective components, as outlined in Chapter 4, in order to aid the investigation of the suitability of servo-pneumatics for the intended purpose. In this section a discussion is presented concerning the design of an adequate experimental setup to facilitate the process. Concerns regarding variations in supply pressure, and the attempts made to negate the potentially detrimental effects thereof during experimental testing, are discussed separately in Appendix E.

3.5.1 Performance Requirements

As per the third objective, each pneumatic circuit will initially be tested while isolated from the overall system in order to negate the effects of interference from sources external to the circuit itself. Quantifiable measures therefore need to be adapted from the overall intended system behaviour in order to facilitate the evaluation of the individual circuits' performance. In order to derive such measures, the ISO 14243 standards' profiles are considered.

Obvious performance measures include the maximum required load amplitudes and ranges of motion present during actuation of the profiles, which form the basis of actuator selection. The speed at which the system must be able to respond gives rise to the additional measures of maximum rate of change for both load and displacement. Table 3.4 lists the specific values as derived from the ISO 14243 standards' profiles.

Furthermore, while the standards require actuation of the profiles at one Hertz (Hz), the frequency content of the profiles themselves tend to be higher, with a maximum of approximately 2 Hz, as shown in Figure 3.6. Therefore, tests designed to evaluate the performance of each circuit in terms of the values previously listed, must ensure that the control input is such that the measured parameter exhibits an overall frequency content of at least 2 Hz if an indication is to be given of the ability of the circuit to contribute adequately to the overall system's behaviour.

Table 3.4: Performance Requirements

Maximum	Load		Displacement	
	Amplitude	Rate of Change	Range of Motion	Rate of Change
AxF	2.6 kN	89.99 kN.s^{-1}	N/A	N/A
F/E	N/A	N/A	58°	54.17 rpm
A/P	265 N	8.34 kN.s^{-1}	5.17 mm	53 mm.s^{-1}
I/E	6 Nm	62.72 Nm.s^{-1}	7.59 °	28.33 rpm

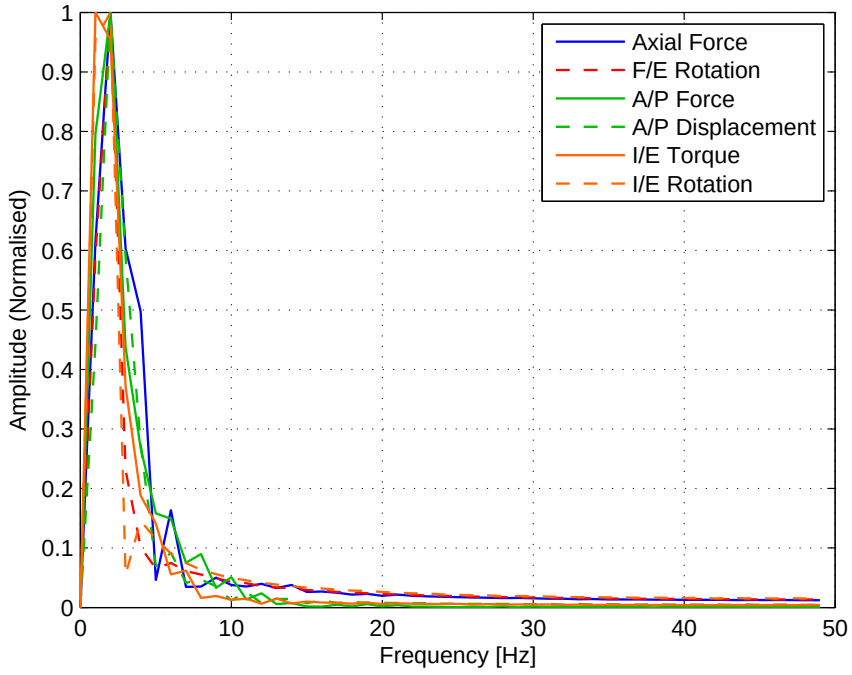

Figure 3.6: ISO Profile Frequency Content

3.5.2 Hardware

Figure 3.7 depicts the experimental setup designed for use during the various tests. The cylinder, valve, load cell and linear variable differential transducer (LVDT) are mounted on an extruded profile via easily removable stainless steel brackets, facilitating reconfiguration of the setup as per the individual requirements of each test and different cylinders. Note that the setup shown is that which is used to evaluate the maximum load as well as its rate of change, hence the need for a load cell. The LVDT is of no use during this particular test, requiring the removal of the load cell assembly if tests are to be conducted where the piston rod is free to move. The particular configurations of each test are described in Chapter 4.

The National Instruments cDAQ system discussed in Section 3.3 is em-

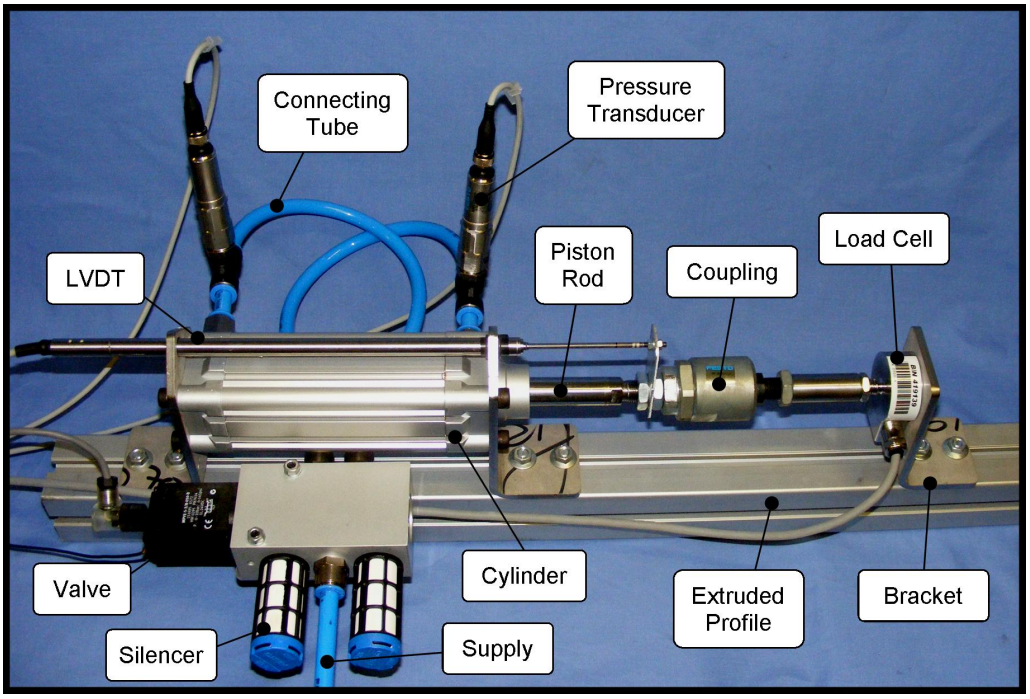

Figure 3.7: Experimental Setup

ployed here, with the various sensors' inputs connected to the NI 9205 analogue input card as needed, while the control signal to the proportional valve's spool is relayed by the NI 9264 analogue output card. Table 3.5 presents the sensors used.

Table 3.5: Sensor Specification

Sensor	Supplier	Part Number	Resolution
Load Cell	HBM	U2B/5kN	2 $mV.V^{-1}$
LVDT	HBM	WA/200	80 $mV.V^{-1}$
Pressure Transducer	Festo	SDET-22T-D10-G14-U-M12	9.9 $mV.kPa^{-1}$

3.5.3 Software

National Instrument's LabView 2009 software was used to develop a program that allows simple control signal generation and data logging of multiple channels simultaneously. A producer/consumer loop approach was implemented, which is based on a master/slave pattern. This methodology facilitates data sharing between different loops that are executed at different rates, while communication between the loops are effected by data queues in order to prevent loss of data. Refer to Figures D.1 and D.2 (Appendix D) for an illustration of

the program's consumer and producer block diagrams, or virtual instrument (VI) as it is otherwise known, respectively.

A producer loop is termed such as it generates data - in the case of the program being described, one such loop generates the control signal while another reads the input from the various sensors. Consumer loops, on the other hand, 'uses' the data produced. One such loop is implemented in order to both graphically display the captured signals and to perform data logging. Data is written in text format to the desktop computer's hard drive for post-processing.

The current program is such that it monitors four analogue inputs and one digital counter input, while producing a single analogue output signal. The analogue inputs are used to monitor the pressure transducers, as well as the bridge amplified LVDT and load cell outputs, as required, while the digital counter reads the rotary encoder input. The analogue output channel produces the control signal for a proportional valve.

A graphical user interface, as shown in Figure D.4 (Appedix D), enables control of various aspects relating to data acquisition and signal generation such as the sampling rates of both the input and output channels, the type, frequency, amplitude and offset of the control signal, and the filepath to which data is logged. Additionally, a timer enables automated recording of all data inputs with respect to a predefined number of control signal cycles.

For the purposes of this thesis, all tests were performed with data capture occurring at 1 kHz, while control signal samples were generated at 100 Hz. Furthermore, data corresponding to eleven cycles of the control signal was captured and logged so that the signals could be cyclically averaged afterwards.

Chapter 4

Modelling and Parameter Identification

This chapter presents the various models of a servo-pneumatic circuit's components, along with methods with which to identify the unknown parameters of each, as per the final objective listed in Chapter 1. Each model is verified not only in terms of accuracy, but also under conditions intended to evaluate their performance as per the relevant requirements developed in Chapter 3, either separately or as part of an integrated system. This is intended to investigate the ability of the pneumatic circuit in question to conform to the ISO 14243 series of standards' protocol, thereby completing the third objective.

Firstly, the basic components of a pneumatic circuit that require modelling are introduced, after which assumptions and equations relating to use of air as an energy medium is discussed. Furthermore, the actuator itself is presented with models describing the piston-rod assembly's dynamics, the chamber's rate of charge and the effects of friction. Many of the relevant parameters may be obtained from the manufacturer's datasheets, though the friction model is experimentally identified. Following this, three models detailing mass flow through an orifice are outlined, identified and evaluated to determine the most suitable. The model selected was particularly suited to cascaded identification of both the valve orifice and connection tubing, as discussed in the applicable section. Finally, the integrated system model is presented and evaluated for both quasi-static and dynamic scenario's.

4.1 Servo-Pneumatic Circuit

A pneumatic circuit consists of basic elements such as an actuator, a command device and connectors, employing compressed air as a medium with which to store or transfer energy. Figure 4.1 illustrates a servo-pneumatic configuration, in which case the actuator is a double acting pneumatic cylinder, the command

device a proportional flow control valve and the connectors are appropriate fittings and tubes.

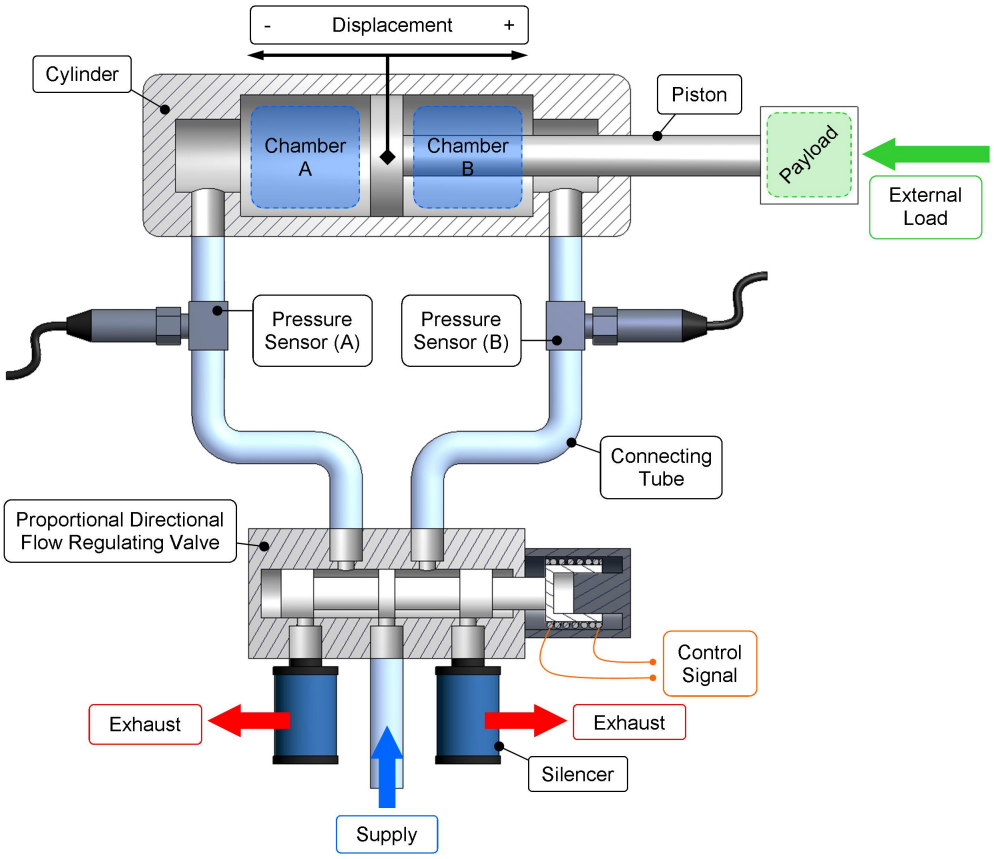

Figure 4.1: Servo-Pneumatic Flow Control Circuit

The cylinder's respective chamber pressures determine the position of the piston as well as the load applied thereto. Controlling these pressures, in turn, is the proportional flow control valve illustrated conceptually in Figure 4.2. A control signal causes the electronics (not shown) to magnetically actuate a coil, thereby displacing the spool attached to it in order to vary the airflow through the valve's orifices. The valves used in this work each receive a variable voltage input ranging between 0 and 10 V, with flow closed off at an input of 5 V. Channel B is therefore connected to the supply pressure when the control signal ranges between 0 and less than 5 V, while the other is open to the atmosphere via the exhaust port. The channels switch roles when the signal ranges from more than 5 V to 10 V.

Models are therefore required that describe the behaviour of the medium, namely air, as well as the relationship between mass flow, the input control signal and the pressures within the cylinder's chambers. The following sections describe such models, taking into account the effects of friction, the difference

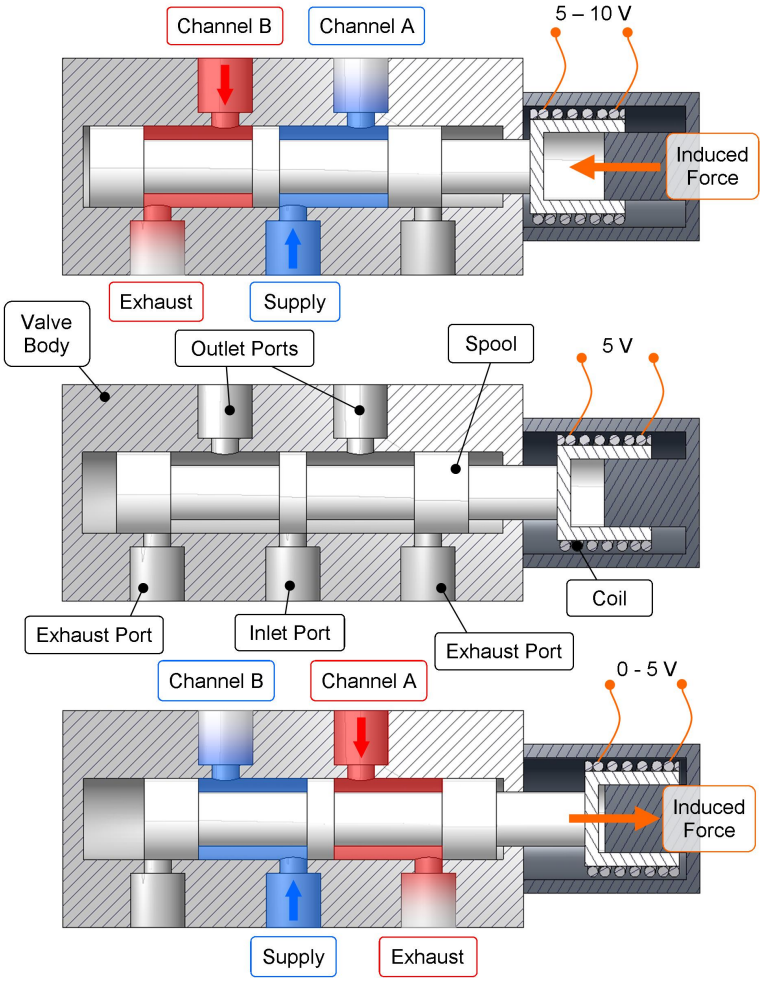

Figure 4.2: Proportional Directional Flow Control Valve Function

in effective areas on either side of a rodded piston, the inactive volumes present at the piston's stroke ends, the differing heat transfer characteristics for the flow inlet and exhaust processes of the cylinder's chambers, and the flow delay and amplitude attenuation caused by the connecting tubes.

4.2 Air Model

The use of compressed air in pneumatic systems necessitates an adequate description of its properties in order to sufficiently investigate the behaviour of the system as a whole. For the purposes of this work, it is assumed that the quantities of interest are fully defined throughout the entire air volume, and that they vary in a continuous manner between different points in the flow. Atmospheric conditions are taken at the standard technical reference as described by the ISO 6358:1989(E) standard, listed in Table 4.1.

Table 4.1: Sensor Specification

Property	Symbol	Value
Atmospheric pressure	P_a	10^5 Pa
Room temperature	T_0	293.15 K
Density	ρ_0	1.185 kg.m^{-3}
Relative humidity	ϕ	65%

Pressure, temperature and volume are interrelated as each affects the mean velocity of the gas molecules. One method to determine the relationship between these parameters is the use of tabulated data sets. While this approach yields accurate results, it tends to be time consuming. Alternatively, use of the ideal gas law, as shown in Equation 4.1 is proposed, where P is the absolute pressure, V is the gas volume, m is the mass, R is the gas constant and T the temperature. Underlying assumptions for the ideal gas law are that the molecules possess mass but no volume, collide elastically, and experience no loss of kinetic energy or linear momentum during such collisions.

$$PV = mRT \tag{4.1}$$

Beater (2007) evaluated the suitability of using the ideal gas law model for the purposes of modelling pneumatic devices by comparing calculated values for density with measured data. It was found that, for temperatures ranging between 200 - 800 K, and pressures between 0.1 - 10 MPa, the model yields values with a relative error of less than 5 %. The ideal gas law is therefore deemed able to adequately describe the behaviour of air for the intended operational conditions.

4.3 Pneumatic Cylinder Model

A double acting pneumatic cylinder, as shown in Figure 4.3, converts energy to linear work via the pressure difference on either side of its piston. Newton's second law describes the dynamic behaviour of the piston-rod assembly as per Equation 4.2.

$$(m_L + m_p + m_r)\,\ddot{x} + F_L + F_f = F_p \tag{4.2}$$

Here $\ddot{x}$ is the piston-rod assembly's acceleration, m_L, m_p and m_r are the masses of the payload, piston and rod, respectively, while F_L, F_f and F_p represent the external load, friction force due to the piston and rod's seals and force acting on the piston due to the pressure differential between the chambers. While the external load may influence the behaviour of the cylinder, its origins are based outside its boundaries. Only models that describe the loading due to chamber pressures and friction effects will therefore be discussed in this

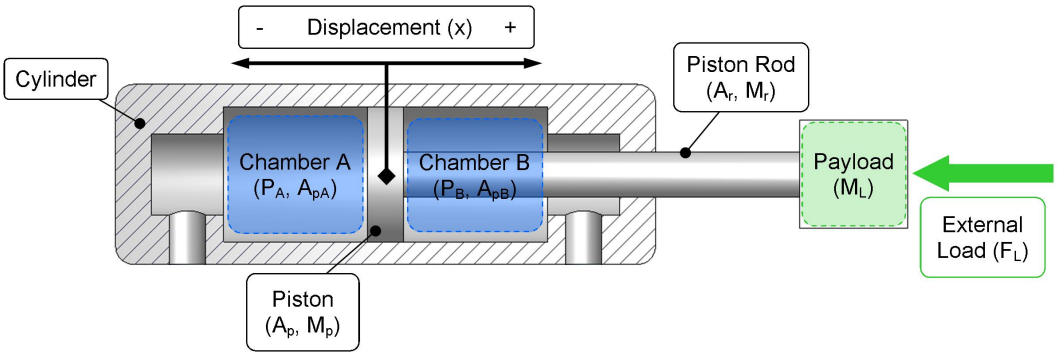

Figure 4.3: Cylinder Chambers

section. Assuming that all load parameters are known, as well as the relevant masses which are easily measured, Equation 4.2 may be solved for the piston-rod assembly's acceleration. Numerical integration would then yield the speed $\dot{x}$, and the translation x.

4.3.1 Cylinder Chambers

Equation 4.3 describes the relationship between the absolute pressures on either side of the cylinder's piston, P_A and P_B, and the force exerted thereon, F_p.

$$F_p = P_A A_{p_A} - P_B A_{p_B} - P_a A_r \tag{4.3}$$

The difference in areas A_{p_A} and A_{p_B} upon which the pressures in chambers A and B acts is due to the presence of the rod, the active area of chamber B being the difference between the piston's circumferential area, or A_{p_A}, and the cross-sectional area of the rod, namely A_r. This also represents the minimum active area used when calculating the maximum required force based on available supply pressure during cylinder selection. Furthermore, the effects of atmospheric pressure, P_a, are also taken into account, where it acts on an area effectively equal to the rod's cross section.

Richer and Hurmuzlu (2000) derives relationships for the rate of pressure change within each chamber, taking into account the different thermal characteristics present during the charging and discharging processes. This phenomenon was studied by Al-Ibrahim (1991), who found experimentally that, for charging, the temperature of air within the relevant chamber approached the adiabatic case, while for discharging the assumption of isothermal behaviour proved more accurate. Based on this, as well as the assumptions that air is a perfect gas, the temperatures and pressures within the cylinder are homogeneous, and that the kinetic and potential energy terms of air are negligible, Richer and Hurmuzlu (2000) presents the following equations for the rates of pressure change within the chambers:

$$\dot{P}_A = \frac{RT}{V_{0_A} + A_{p_A}\left(\frac{1}{2}L + x\right)}\left(\alpha_{in}\dot{m}_{t_{in}} - \alpha_{ex}\dot{m}_{t_{ex}}\right)_A - \alpha\frac{P_A A_{p_A}}{V_{0_A} + A_{p_A}\left(\frac{1}{2}L + x\right)}\dot{x}$$

$$\dot{P}_B = \frac{RT}{V_{0_B} + A_{p_B}\left(\frac{1}{2}L - x\right)}\left(\alpha_{in}\dot{m}_{t_{in}} - \alpha_{ex}\dot{m}_{t_{ex}}\right)_B + \alpha\frac{P_B A_{p_B}}{V_{0_B} + A_{p_B}\left(\frac{1}{2}L - x\right)}\dot{x} \tag{4.4}$$

V_{0_A} and V_{0_B} denotes the inactive volumes present at the end of stroke and inlet ports for the respective chambers, L is the piston's stroke length, T is the temperature of the gas at the supply and in the chambers, and α_{in}, α_{ex} and α are the heat transfer coefficients. These coefficients are bounded between one and γ, the ratio of specific heats as per Equation 4.5 in which cp and cv are the specific heat capacities at constant pressure and volume, respectively. For air, γ has a value of 1.4.

$$\gamma = \frac{cp}{cv} \tag{4.5}$$

For charging, α_{in} is assumed to have a value of close to γ, denoting an adiabatic process, and α_{ex} a value close to one for isothermal behaviour during discharge. The coefficient α, which represents the thermal characteristic for the compression/expansion process due to piston movement, is assigned a value of 1.2, as per Al-Ibrahim (1991).

Considering 4.4, the first term of each pressure derivative describes the effects of flow of air either in or out of the cylinder, while the second term accounts for the rate of pressure change due to the movement of the piston, causing either compression or expansion of the control volumes depending on the direction of translation. Here, translation of the piston towards the payload is deemed positive, with the origin defined at the centre of the stroke.

Mass flow into or out of each chamber may occur either due to the intended operation of the control element, namely the valve, as per Section 4.4, or due to the effects of leakage. Leakage may be present in the valve itself, but for the purposes of modelling the cylinder air is considered to either escape via the rod-seal interface, or to pass between the adjoining chambers themselves, should one chamber be at a higher pressure than the other. As per Richer and Hurmuzlu (2000), leakage may be neglected when modelling standard cylinders with rubber seals, an assumption confirmed by Beater (2007). Its effects can, however, be significant for cylinders with low friction seals and, should this be the case, it is suggested that leakage be modelled in a manner similar to that used for the valve orifices (Richer and Hurmuzlu, 2000).

4.3.2 Friction

As mentioned in Chapter 2, friction is one of the most important non-linearities within the actuator (Nouri *et al.*, 2000), requiring adequate modelling to ensure positional accuracy and improved bandwidth (Belforte *et al.*, 2003). The absence of an universal friction model makes this difficult (Nouri, 2004), necessitating that model selection instead be based on inspection of the data (Harris *et al.*, 2011).

The classical Coulomb friction model describes a discontinuous relationship between the friction force and velocity (Tjahjowidodo *et al.*, 2007) as per Equation 4.6.

$$F_f = \begin{cases} F_p & \text{if } \dot{x} = 0 \text{ and } F_p < F_{sf} \\ F_{sf} & \text{if } \dot{x} = 0 \text{ and } F_p \geq F_{sf} \\ F_{cf} + C_{vf}\dot{x} & \text{if } \dot{x} \neq 0 \end{cases} \tag{4.6}$$

Here the static friction is denoted by F_{sf}, Coulomb friction by F_{cf} and the viscous component by C_{vf}. The Coulomb model, while applicable in certain cases (Nouri, 2004), is unable to accurately describe the variation in behaviour evidenced by the different velocity regimes as per Armstrong-Hélouvry *et al.* (1994), should such behaviour become prevalent. These regimes are detailed as follows:

I) Static Friction Here friction force is a function of displacement, as opposed to velocity, due chiefly to the elastic deformation of asperity contacts.

II) Boundary Lubrication At low velocities a fluid film is not yet present, and friction force is mainly due to the shearing of solid-to-solid asperity contacts. Friction is therefore heavily affected by the material's surface properties and lubricant chemistry.

III) Partial Fluid Lubrication For rising velocities, lubricant is drawn into the load-bearing region. Its viscosity prevents pressure from expelling all of the lubricant, resulting in the formation of a fluid film between the opposing surfaces. The film height, however, is still less than the average maximum asperity height, therefore resulting in some solid-to-solid contact.

IV) Full Fluid Lubrication Here friction is a function of velocity as affected by the lubricant's viscosity. The fluid film is fully formed, resulting in complete separation of the opposing surfaces.

Figure 4.4 illustrates the aforementioned regimes as approximated by the Stribeck curve of Equation 4.7. Note that neither the Coulomb model nor

the Stribeck curve makes provision for displacement occurring during regime I, otherwise known as pre-sliding behaviour.

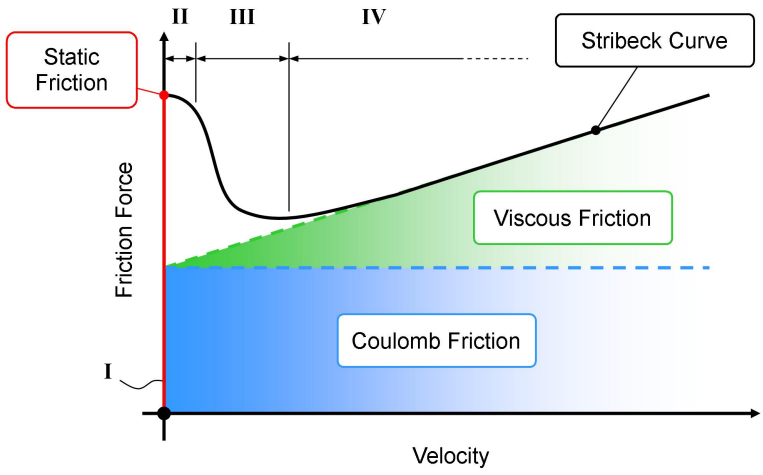

Figure 4.4: Friction Velocity Regimes
(Adapted from Andrighetto *et al.* (2006); Armstrong-Hélouvry *et al.* (1994))

The Stribeck curve $S(v)$ contains a velocity weakening component, bounded by the static friction at zero velocity and a lower limit equal to the Coulomb friction. Other familiar parameters include the constant F_{cf} as well as the viscous component C_{vf}. Additionally, though, Equation 4.7 details the Stribeck velocity $\dot{x}_s$ and an arbitrary exponent δ, constants used to adapt $S(v)$ to the data at hand.

$$S(v) = F_{cf} + C_{vf}\dot{x} + (F_{sf} - F_{cf})\, e^{-\left(\frac{\dot{x}}{\dot{x}_s}\right)^{\delta}} \tag{4.7}$$

By substituting Equation 4.7 into the appropriate case of Equation 4.6, a friction model suitable for control purposes may be derived. The model used in this work, however, is that of Tjahjowidodo *et al.* (2007), as it negates the effects of the discontinuity near zero velocity by introducing a line of finite slope up to a small threshold ε. The resulting model is as follows:

$$F_f = \begin{cases} S(v) & \text{if } |\dot{x}| > \varepsilon \\ \\ \frac{\dot{x}}{\varepsilon} S(v) & \text{if } |\dot{x}| \leq \varepsilon \end{cases} \tag{4.8}$$

Apart from the fact that the Stribeck curve takes the sliding velocity regime's behaviour into account, an additional advantage is that appropriate parameter selection could result in a wide variety of curve shapes as per Andrighetto *et al.* (2006). Still, due to the complex nature of friction, the relatively simple model presented by Equation 4.8 leaves many potential behaviour-influencing aspects un-modeled. While some of these aspects may

have negligible effects when compared to others, it is difficult to determine prior to some form of experimental investigation which of them may be ignored, and which of them must be included within an appropriate model. Therefore, friction modelling and parameter identification within the scope of this thesis will be concerned only with adequately implementing the model of Equation 4.8 and, to an extent, identification of significant un-modeled aspects for future consideration. Some of these aspects, as discussed in literature, are listed here:

Pre-Sliding Behaviour As previously mentioned, friction within regime I is primarily a function of position, additionally exhibiting hysteretic behaviour with non-local memory (Tjahjowidodo *et al.*, 2007).

Frictional Lag Hysteretic behaviour during gross-sliding results in the over-estimation of friction force during acceleration and its under-estimation during de-acceleration with respect to the steady state function which, in this case, is the Stribeck curve of Equation 4.7 (Al-Bender, 2010).

Dwell Time Static friction rises with dwell time up to an identifiable maximum, the ultimate static friction (Armstrong-Hélouvry *et al.*, 1994)

Chamber Pressure Variations in chamber pressure affects the contact forces between the piston seals and the walls of the chamber, causing the resultant static or breakaway friction to vary accordingly (Nouri, 2004).

Positional Dependency Friction force may vary along a piston's displacement due to machining tolerances, surface roughness and uneven distribution of lubricant (Belforte *et al.*, 2003).

4.3.3 Parameter Identification

Parameters relating to the physical and geometric properties of the actuator used, namely Festo's DNC-50-160-PPV-A double acting piston rod cylinder, were determined by perusing the manufacturer's data-sheet where possible. The only parameters not identified in this manner are the dead volumes of either chamber. These values may be determined by calculation using detailed drawings of the cylinder, by filling the respective chambers with the piston at the stroke end in question with a suitable fluid, and then measuring said fluid's volume, or by estimation and tuning to obtain a best fit of the data. Last mentioned approach was chosen, and implemented during validation of the entire pneumatic circuit described in Section 4.6.

Furthermore, it was assumed that the temperature of the gas both in the supply and chambers remained constant at the standard atmospheric reference condition, as used in Equation 4.4. The heat transfer coefficients α_{in}, α_{ex} and α were assumed to have values as detailed by Richer and Hurmuzlu (2000).

Refer to Table I.1 (Appendix I) for a complete list of the various parameters relating to the specific actuator used.

The friction model of Equation 4.8 requires identification of the static friction F_{sf}, Coulomb friction F_{cf}, frictional viscosity C_{vf}, Stribeck velocity $\dot{x}_s$ and the arbitrary exponent δ parameters. An important observation is that a pneumatic cylinder may exhibit different friction characteristics for opposing directions of movement due to anisotropies in the material or geometry (Armstrong-Hélouvry *et al.*, 1994). Friction parameters must therefore be identified separately for both directions of piston displacement.

In order to set up a quasi-static friction-velocity map similar to Figure 4.4, numerous constant-velocity tests within the range of interest must be executed while measuring friction force. A drawback of such an approach is the difficulty associated with controlling the velocity prior to model identification (Nouri, 2004). Andrighetto *et al.* (2006) circumvents this issue by assuming that for a fixed valve orifice opening, the velocity would remain approximately constant. A similar approach is followed here, with the validity of said assumption investigated shortly.

The test setup used during friction parameter identification is that of Figure 4.1, with the actuator's cushioning spears and seals removed as per the discussion in Appendix F. A square wave input signal which oscillates about the neutral voltage of 5 V was applied to the proportional valve, causing the orifices obstructing the flow paths to open to the supply and atmosphere, respectively. Each chamber of the cylinder is therefore either charged or discharged, causing the piston to be displaced cyclically in both the positive and negative directions. Figure 4.5 shows an example of an input control signal, with the corresponding cyclic displacement. The full test protocol is detailed in Table H.1 (Appendix H).

During each test, the respective chamber pressures are recorded along with the piston's displacement for eleven control signal cycles. These results were then cyclically averaged in order to reduce signal noise and negate the effects of potential disturbances. Velocity is determined from the slope of a linear fit applied to the displacement signal portions that relate to the piston's movement between end positions, disregarding the transient signal components at the stroke ends.

The assumption of constant velocity results in the disappearance of the inertial term from Equation 4.2. As no external load is applied, friction force may then be solved from said relation by calculating the piston force as per Equation 4.3. This was done by considering the recorded chamber pressures during the corresponding mid-stroke displacement of the piston, and taking the mean of the subsequently estimated F_f in order to obtain a single friction force value per constant velocity. Figure 4.6 illustrates the resulting friction-velocity map for both positive and negative velocities.

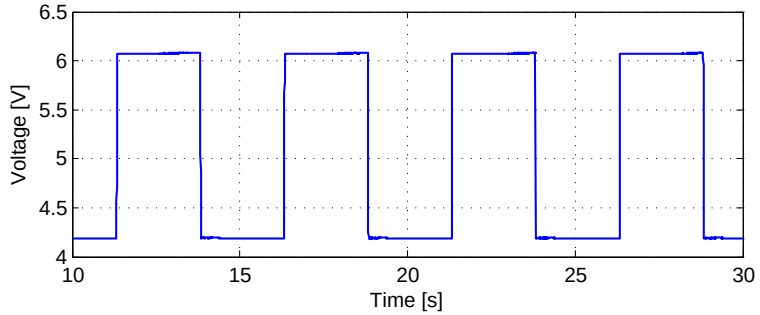

(a) Control Signal

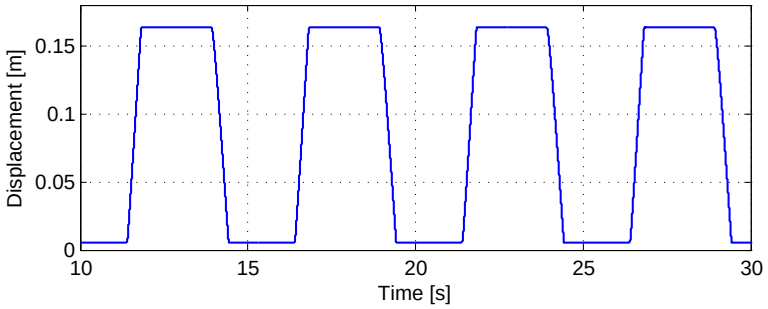

(b) Piston Displacement

Figure 4.5: Displacement Cyclic Average Example

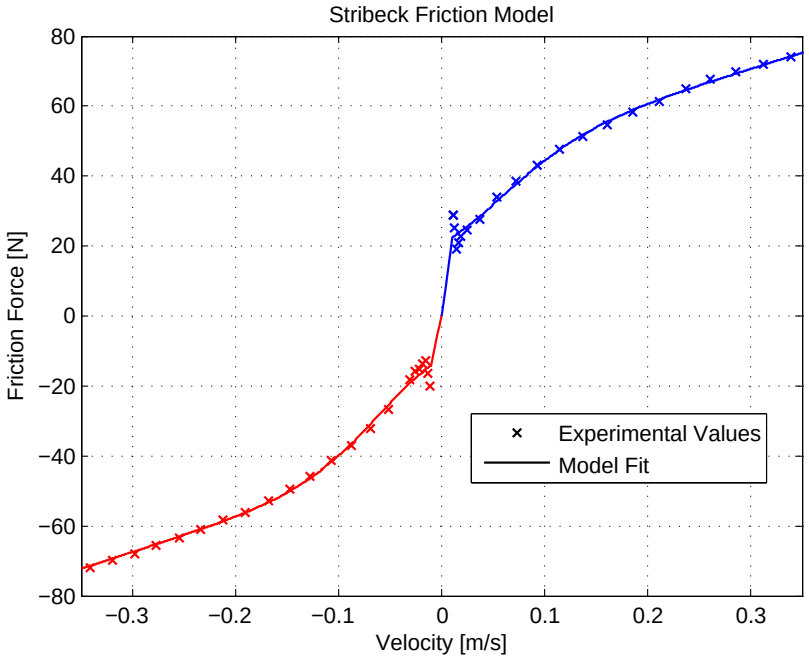

Figure 4.6: Quasi-Static Friction-Velocity Map

Here the parameters of Equations 4.7 and 4.8 are solved using Matlab's `lsqcurvefit` function which performs non-linear curve fitting based on minimisation of the least-squares error. The values identified thus are listed in Table I.2. Investigation of the obtained parameters reveal a Coulomb friction value lower than that of the identified static friction. While contrary to expectations, these particular values results in the Stribeck velocity component being converted to a velocity-strengthening component in order to account for the convex shape of the data-values during the transition between the partial and full fluid lubrication regimes III and IV. This shape is in contrast to the concave curve illustrated in Figure 4.4.

To obtain a more realistic model in terms of the values of F_{sf} and F_{cf}, and to better reproduce the transition from the boundary lubrication regime II to regime III, Equation 4.7 may be expanded to include an additional exponential term, similar to the Stribeck component bounded by the static and Coulomb friction parameters, with an independent amplitude parameter. This term would then account for the convex shape of the transition between regimes III and IV, while the Stribeck velocity-weakening component may be applied to the transition of regimes II and III as intended. Though said process would be in accordance with the statement that friction model selection should be based on investigation of experimental data (Harris *et al.*, 2011), it is not considered in this work due to time constraints.

Finally, it should be noted that the range of velocities investigated well exceeds the performance requirement for the A/P circuit, for which the current actuator is intended, as listed in Table 3.4 (Chapter 3). In this particular case, however, the velocity-requirement may only serve as a guideline since the system is investigated in terms of a quasi-static model, its applicability to dynamically varying signals being evaluated shortly.

4.3.4 Validation

This section is concerned only with the validation of the friction model and, to the extent that it is applicable to friction, the equation of motion, and not the cylinder chambers' model. The latter will be verified indirectly for the case of a fixed volume in the section concerning the valve orifice models, and in its entirety as part of the overall pneumatic circuit verification. As a matter of interest, refer to Carneiro and de Almeida (2006*b*) for an in depth evaluation and comparison of the various cylinder chamber models used in literature.

Firstly, the assumption that piston velocity remains constant for a fixed orifice opening is investigated. This was done by calculating the mean absolute error (MAE) between the linear fit on the piston's mid-stroke displacement and the actual recorded data values, as per Equation 4.9.

$$MAE = \frac{1}{n}\sum_{i=0}^{n}|f_i - y_i| \tag{4.9}$$

Here n is the number of data samples, f_i is the estimated value and y_i the relevant recorded value. Using this approach, a single value illustrating error between the estimation function and experimental data may be obtained for each dataset used to identify the unknown parameters. The results are shown in Figure 4.7 for displacement relating to both positive and negative velocities.

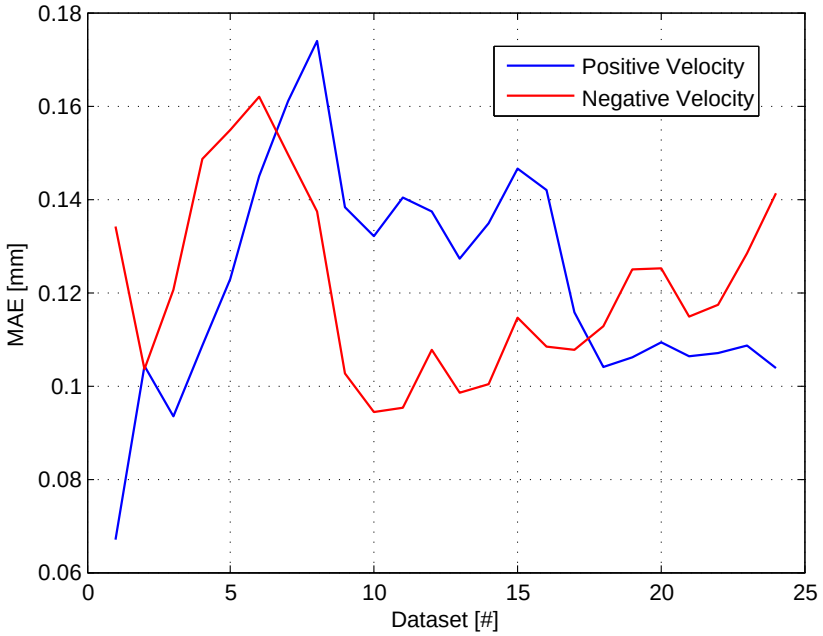

Figure 4.7: Linear Fit MAE

From the figure it is clear that the maximum MAE value is less than 0.26 mm, the allowable tolerance on the A/P profile as specified by the ISO 14243:2004(E) standard. This gives an indication that the relevant assumption may prove adequate for parameter identification procedures, though it is not the only source of error within the method outlined previously. The fact that a mean value for the friction force is used to obtain a single data point for each constant velocity value may result in the introduction of additional inaccuracies as the recorded chamber pressure values used to estimate F_f do not remain constant within the interval of interest.

Therefore, using the discrete derivative of the piston's displacement within the portion of mid-stroke used to identify the friction parameters as velocity input to the model of Equation 4.8, MAE values are determined for each dataset. Inputs to Equation 4.9 are the predicted values of the model and the friction force based on the recorded chamber pressures, prior to calculating the mean thereof. The results are shown in Figure 4.8.

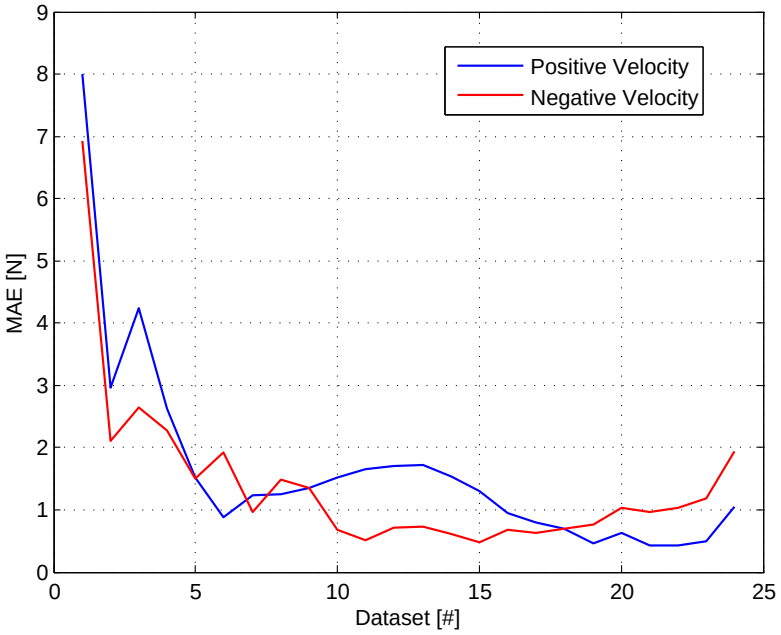

Figure 4.8: Quasi-Static Friction MAE

The datasets are arranged in terms of increasing orifice openings and, therefore, increasing resultant velocity magnitudes. Datasets corresponding to low velocities are thus located towards the origin of Figure 4.8's axes. As the highest MAE are located in this region, indications are that the model's behaviour deteriorates for decreasing velocities. The possibility exists that the poor correlation between the model prediction and the experimental data within this region is due to the inadequate modelling of the transition between regimes II and III of the Stribeck curve, as previously discussed, and not so much the variation of the chamber pressures. For increasing velocities, where the model fit is improved, the MAE values are significantly lower. Still, the maximum MAE value is less than 13 N, the allowable tolerance specified by the ISO 14243:2009(E) standard.

Finally, the dynamic friction behaviour of the actuator is briefly investigated, as shown in Figure 4.9. The experimental friction-velocity map shown is obtained by applying a sinusoidal control signal to the proportional valve. Said signal is biased to vary about the neutral closed off position of the valve, with the amplitude selected such that the resulting velocity covers a sufficiently large range. Care must be taken to ensure the piston oscillates well within mid-stroke, as back-pressure build-up near the end positions may occur even though the pneumatic cushioning components have been removed. Also, in order to account for the inertial term in Equation 4.2, displacement data is twice differentiated. Cyclic averaging and adequate smoothing results in

a sufficiently noise-less estimate of acceleration, though high frequency signal components may be lost in the process. Measuring acceleration directly could, however, allay this concern (Nouri, 2004).

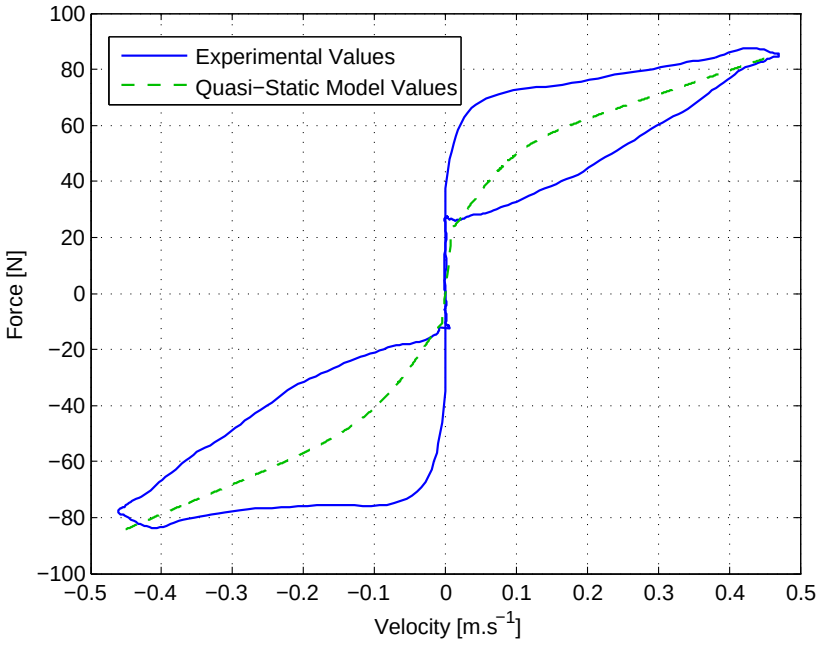

Figure 4.9: Dynamic Friction Velocity Map

Note the distinct hysteresis behaviour during gross-sliding, manifesting as an overestimation of the quasi-static model's result during acceleration and its underestimation during de-acceleration. The model of Equations 4.7 and 4.8 is, needless to say, unable to account for the apparently significant effects of frictional lag. Furthermore, since the ISO 14243 standards describe A/P profiles that result in relatively low velocities, and specifically velocity inversion, Tjahjowidodo *et al.* (2007) strongly recommends explicit modelling of the pre-sliding behaviour as well.

To conclude, the method used to determine the quasi-static model parameters of Equation 4.8 appears reasonably accurate for medium to high constant velocities. While poor model performance is evident for low velocities, the discrepancy is suspected to arise from inadequate model choice and not necessarily the identification procedure. Furthermore, the quasi-static model is inadequate in the presence of dynamically varying velocity inputs. The dominant un-modelled component appears to be frictional lag, with pre-sliding behaviour expected to play a role for lower velocities that exhibit inversion. It is therefore recommended that identification of a dynamic friction model, such as the Generalised Maxwell Slip model (Lampaert *et al.*, 2003; Al-Bender *et al.*,

2005), which explicitly accounts for these aspects in addition to quasi-static friction behaviour, is investigated.

4.4 Valve Orifice Flow Rate Model

A proportional control valve affects mass flow by varying its exposed orifice area, hence the need for a model describing said relationship between orifice and flow. St. Venant and Wantzel (1839) first presented one for free discharge through a well rounded orifice in which no flow contraction occurs, illustrated by Equation 4.10. This was derived from first principles under the assumptions that gas behaves ideally, no heat exchange occurs, the upstream pressure and temperature remains constant, and that the approach velocity is negligible.

$$\dot{m} = A\psi P_u \sqrt{\frac{2}{RT_u}} \tag{4.10}$$

Here $\dot{m}$ is the mass flow, A is the orifice area, and P_u and T_u are the upstream pressure and temperature, respectively. The flow function ψ is given by Equation 4.11, where P_u is the downstream pressure.

$$\psi = \sqrt{\frac{\gamma}{\gamma - 1}\left[\left(\frac{P_d}{P_u}^{\frac{2}{\gamma}}\right) - \left(\frac{P_d}{P_u}^{\frac{\gamma+1}{\gamma}}\right)\right]} \tag{4.11}$$

Figure 4.10 plots the flow function for a constant upstream pressure versus the relevant, varying pressure ratio $\frac{P_d}{P_u}$. The maximum, ψ_{max}, occurs at a pressure ratio of 0.528, otherwise known as the critical pressure ratio P_{cr}. This is the point where mass flow reaches sonic velocity.

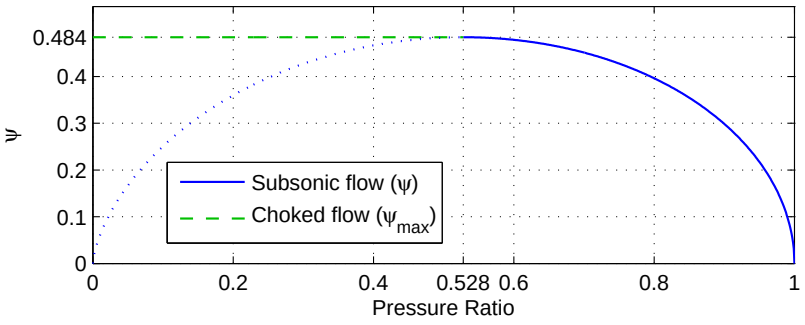

Figure 4.10: Flow Function

As per Beater (2007), once sonic velocity is attained, decreasing values of pressure ratio below the critical value does not result in an increase of velocity into the supersonic range. A constant corresponding to the value of ψ_{max} is

therefore used to represent the flow function in this, the choked flow region. Equation 4.12 depicts the resulting flow function model used.

$$\psi = \begin{cases} \left(\frac{2}{\gamma+1}\right)^{\frac{1}{\gamma-1}} \sqrt{\frac{\gamma}{\gamma+1}} & \text{if } \frac{P_d}{P_u} \leq P_{cr} \text{ (choked)} \\ \sqrt{\frac{\gamma}{\gamma-1}\left[\left(\frac{P_d}{P_u}\right)^{\frac{2}{\gamma}} - \left(\frac{P_d}{P_u}\right)^{\frac{\gamma+1}{\gamma}}\right]} & \text{if } \frac{P_d}{P_u} > P_{cr} \text{ (subsonic)} \end{cases} \tag{4.12}$$

Furthermore, the use of thin, sharp edged orifices as opposed to those that are well rounded, as is indeed the case with the valves used for this work, requires taking into account various factors that affect a reduction in mass flow rate. Such factors, which include jet contraction, friction and heat losses (Beater, 2007), may be modelled for turbulent flow by introducing a discharge coefficient, Cd, into Equation 4.10, resulting in this, the traditional orifice flow equation:

$$\dot{m} = ACd\psi P_u \sqrt{\frac{2}{RT_u}} \tag{4.13}$$

As per Beater (2007), while the discharge coefficient approaches a constant value for incompressible flow with high Reynolds numbers, for compressible flow it is a function of the pressure ratio. Pugi *et al.* (2004) presents Equation 4.14 for Reynolds numbers greater than 100,000. The fact that constant discharge coefficient values have been used to model compressible flow with alleged success (Richer and Hurmuzlu, 2000; Zhu, 2006) does, however, merit attention.

$$Cd = 0.8414 - 0.1001\frac{P_d}{P_u} + 0.8415\frac{P_d}{P_u}^2 - 3.9\frac{P_d}{P_u}^3 + 4.001\frac{P_d}{P_u}^4 - 1.6827\frac{P_d}{P_u}^5 \tag{4.14}$$

Figure 4.11 shows the effect of varying the discharge coefficient according to Pugi *et al.*'s relation on mass flow rate, as opposed to using some constant value. Note that the mass flow is affected to well within the choked flow region.

Nevertheless, the model presented in the ISO 6358:1989(E) standard lumps together both the orifice area and discharge coefficient within a single constant, namely the sonic conductance C as shown:

$$C = \frac{CdA}{\rho_0}\sqrt{\frac{\gamma}{RT_0}\left(\frac{2}{\gamma+1}\right)^{\frac{\gamma+1}{\gamma-1}}} \tag{4.15}$$

Note the use of the standard reference temperature T_0 and density ρ_0. Rewriting Equations 4.13 and 4.12 for use with Equation 4.15 yields the result of Equation 4.16.

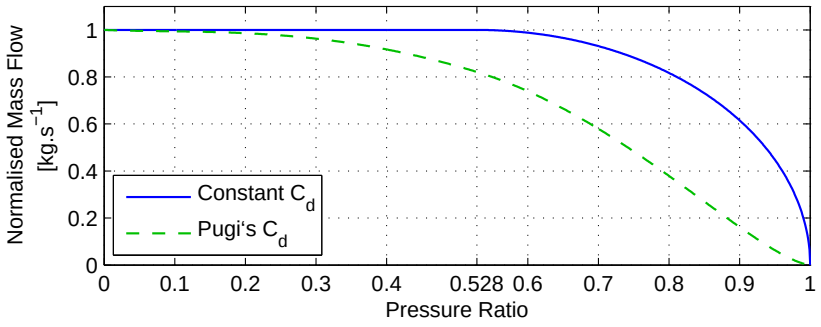

Figure 4.11: Effects of Variable Discharge Coefficient

$$q = CP_u\sqrt{\frac{T_0}{T_u}}\psi_{ISO} \tag{4.16}$$

Where q is the volume flow rate through the orifice, as opposed to the mass flow rate given by Equation 4.13, while the flow function's subsonic portion is approximated by a quarter section of a curve, as per Equation 4.17:

$$\psi_{ISO} = \begin{cases} 1 & \text{if } \dfrac{P_d}{P_u} \leq b \text{ (choked)} \\ \sqrt{1 - \left(\dfrac{\frac{P_d}{P_u} - b}{1-b}\right)} & \text{if } \dfrac{P_d}{P_u} > b \text{ (subsonic)} \end{cases} \tag{4.17}$$

Here the critical pressure ratio is given by b, which differs from the theoretical value indicated by P_{cr} for many commercial valves because such valves' flow paths typically contain more than one orifice in series. This effectively reduces the critical pressure ratio for the given component (Beater, 2007). Regardless of this limitation, the theoretical orifice mass flow model is still widely used in literature for the modelling of complex flow paths (Harris *et al.*, 2011).

The ISO 6358:1989(E) model's flow function has recently been further expanded to include two additional parameters, namely the cracking pressure ratio a and the subsonic flow index β (Harris *et al.*, 2011), as shown in the following equation:

$$\psi_{ISO} = \begin{cases} 1 & \text{if } \dfrac{P_d}{P_u} \leq b \text{ (choked)} \\ \left[1 - \left(\dfrac{\frac{P_d}{P_u} - b}{a-b}\right)\right]^{\beta} & \text{if } \dfrac{P_d}{P_u} > b \text{ (subsonic)} \end{cases} \tag{4.18}$$

The cracking pressure ratio, a term descendent from the minimum upstream pressure at which a check valve will operate, accounts for a situation where flow may cease before the downstream to upstream pressure ratio has

reached unity. The subsonic index allows for greater flexibility when modelling a flow path as a concatenated series of orifices as opposed to a single restriction.

In order to retain the ability to model the discharge coefficient as a function of the pressure ratio, while additionally including the effects of parameters b, a and β, Equation 4.12's subsonic case has been replaced by the relevant quarter-section-ellipse approximation of Equation 4.18. Noting that the only discrepancy between Equations 4.12 and 4.18 apart from that introduced by the approximation itself is the choked flow constant's magnitude, the following relation is presented for use in conjunction with Equation 4.13:

$$\psi_e = \begin{cases} \left(\frac{2}{\gamma+1}\right)^{\frac{1}{\gamma-1}} \sqrt{\frac{\gamma}{\gamma+1}} & \text{if } \frac{P_d}{P_u} \leq b \text{ (choked)} \\ \left(\frac{2}{\gamma+1}\right)^{\frac{1}{\gamma-1}} \sqrt{\frac{\gamma}{\gamma+1}} \left[1 - \left(\frac{\frac{P_d}{P_u} - b}{a-b}\right)\right]^{\beta} & \text{if } \frac{P_d}{P_u} > b \text{ (subsonic)} \end{cases} \tag{4.19}$$

The effects of varying the critical and cracking pressure ratios, as well as that of the subsonic index, are illustrated in Figure 4.12. By setting these parameters to 0.528, 1 and $\frac{1}{2}$ respectively, and by neglecting the discharge coefficient, it may be shown that the extended flow function equation in conjunction with Equation 4.10 approaches the theoretical model's results for a well rounded orifice with an error of only 0.33% (Beater, 2007).

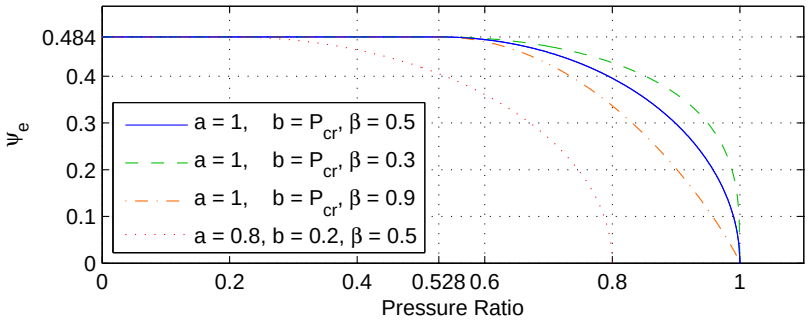

Figure 4.12: Extended Flow Function with Varying Parameters

Finally, for the purposes of this work, the dynamics of the valve's spool is neglected as part of the model due to the large bandwidth of a typical proportional valve, 65 Hz in this case, as compared to the relatively low bandwidth achievable in pneumatic servo-systems, which is not more than 10 Hz (Ning and Bone, 2005).

4.4.1 Parameter Identification

In order to set up a valve orifice model based on Equations 4.13 and 4.19, parameters that need to be determined are the discharge coefficient Cd, the orifice area A, the critical pressure ratio b, the cracking pressure ratio a and the subsonic index β.

To start with, identification of the discharge coefficient is discussed. As previously mentioned, Cd is considered a function of the downstream to upstream pressure ratio, though constant values of this parameter are also frequently used. Methods have been presented to determine this value (Richer and Hurmuzlu, 2000; Zhu, 2006), but the manufacturer of the valves (Festo) has, upon request, supplied a document in which the sonic conductance and critical pressure ratio, as evaluated in accordance with the ISO 6358:1989(E) standard, are listed (anon., 2006). Assuming that these values hold for the maximum geometric orifice area $A_{max} = \pi\frac{1}{4}D_h^2$ where D_h is the nominal bore radius, and that during testing the inlet and exhaust flow paths were identical, by rewriting Equation 4.15 the discharge coefficient may be determined. Use of this constant value of Cd will be compared to that of Pugi *et al.* (2004), Equation 4.14.

The effects of the additional components present in the valve's flow paths, such as fittings and silencers, may be modelled as a concatenated series of orifices by considering the flow path assembly as a whole (Beater, 2007). Since the discharge coefficient has already been determined based, per assumption, on the effects of the valve alone, the identified orifice area will no longer represent the restriction of just the valve's orifices, but the combined effect of all components present in the relevant flow path. Henceforth, it will therefore be referred to as the effective orifice area A_{eff}. This has to be solved simultaneously with b, a and β, as these parameters are included with the express purpose of further adapting the flow function to each flow path assembly's unique behaviour (Harris *et al.*, 2011), and are interrelated.

That said, by investigating the manner in which the orifice areas of the proportional valve are delimited by the spool depending on the input control signal, insight may be obtained concerning the expected values of the these parameters. Such an approach is discussed in Appendix G. Experimentally identified values of A_{eff} are expected to display a similar order of magnitude, though probably lower exact values due to added restrictions within the flow path. The shape of the curve corresponding to that of Figure G.2 should also be identifiable.

Continuing, the expected values of parameters b, a and β may additionally be estimated. First, considering the critical pressure ratio b, note that it will be equal to the corresponding theoretical value of 0.528 for the ideal case of a single orifice. This is also the expected maximum, as any additional restrictions within the flow path will contribute to a reduction of b's value. Should b be negative, choked flow will never occur (Nouri *et al.*, 2000).

The cracking pressure ratio a is considered to be unity for the theoretical and ISO flow function models, as this represents the situation where the downstream pressure has reached the value of the upstream condition. This will normally be the maximum value, except in certain cases such as where shock waves may develop as a sudden inflow of air reaches an end restriction. The models presented here, unfortunately do not account for this phenomenon. The minimum value of a is given by considering atmospheric pressure as downstream with the supply as upstream. Using absolute pressure values, this will never become zero.

The last parameter to consider before identification commences is the subsonic index β. A value of $\frac{1}{2}$ reproduces the theoretical and ISO flow function models. Otherwise, upper and lower limits of β are difficult to determine as it was introduced purely to increase the flexibility of the extended flow function model (Harris *et al.*, 2011), as opposed to parameters b and a, the addition of which is based on observed phenomenon.

The ISO 6358:1989(E) standard details an experimental setup which may be used to investigate parameters pertaining to mass flow through an orifice. This method requires large amounts of air (Beater, 2007) in addition to a number of experiments to identify parameters for a single orifice opening, resulting in a great expense of energy and effort if a proportional flow control valve's flow paths are to be investigated in a step-wise manner with sufficient resolution across the input signal's range. Therefore an alternative setup, as presented by Guang-zheng and Wei (2005) and Bubert (2009) and shown in Figure 4.13, is used.

In this configuration, the pressure vessel is connected to the valve's channel being investigated, while the other is sealed off to negate the effects of leakage. Festo's SDET type pressure transducers are used to measure the supply and chamber pressures as shown, respectively, with the supply set at 7 bar absolute pressure. Connecting tubes are kept short in order to support the assumption that flow losses within them may then be considered negligible. The control signal is cycled as a square wave in such a manner that the relevant channel's orifice is either gradually opened towards the supply in an iterative fashion for each test, or fully opened to the atmosphere. This is done for both charge and discharge of the chamber in order to investigate mass flow through each channel's inlet and exhaust paths separately.

For instance, when mass flow to and from the pressure vessel is effected via channel A, control signal values of between 5 and 10 V causes the relevant orifice to open to the supply, while a value of below 5 V connects the pressure vessel to the atmosphere. Therefore, in order to record the vessel pressure during charging, and hence determine parameters relating to the inlet flow path of channel A, the previously mentioned square wave is set up with an appropriate bias, amplitude, frequency and duty cycle so that before each charge at values of, for example 5.2, 5.4, 5.6 and so forth to a maximum of 10 V, the chamber is fully exhausted by applying a control signal of 0 V to the

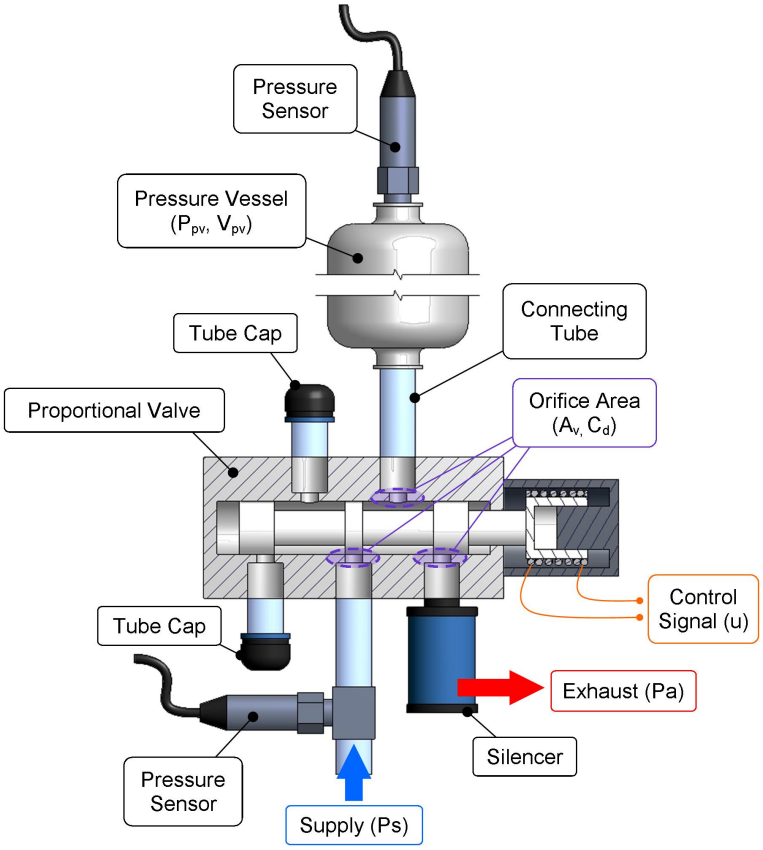

Figure 4.13: Effective Orifice Area Experimental Setup

valve.

To examine the exhaust flow process, similar tests may be conducted. For this case, however, the pressure vessel is considered the source and it is therefore fully charged by an input of 10 V before pressure therein is recorded for values such as 4.8, 4.6 and 4.4 to a minimum of 0 V as air is exhausted to the atmosphere. Channel B is tested in the same manner, except that the vessel is charged for control signal inputs of between 0 and 5 V, while discharge occurs for values of between 5 and 10 V. Figure 4.14 shows examples of control signals and the recorded vessel pressures for channel A's charge and discharge identification processes. The full test protocol is detailed in Table H.2 (Appendix H).

Note that, in each case, the vessel is charged and discharged via the applied square wave control signal in a cyclic manner in order to allow data averaging as mentioned in Chapter 3. The purpose of this is to lessen the effects of potential disturbances and noise.

Bubert (2009) then continues by modifying Equation 4.4 to yield the rate of pressure change for a fixed volume pressure vessel as follows:

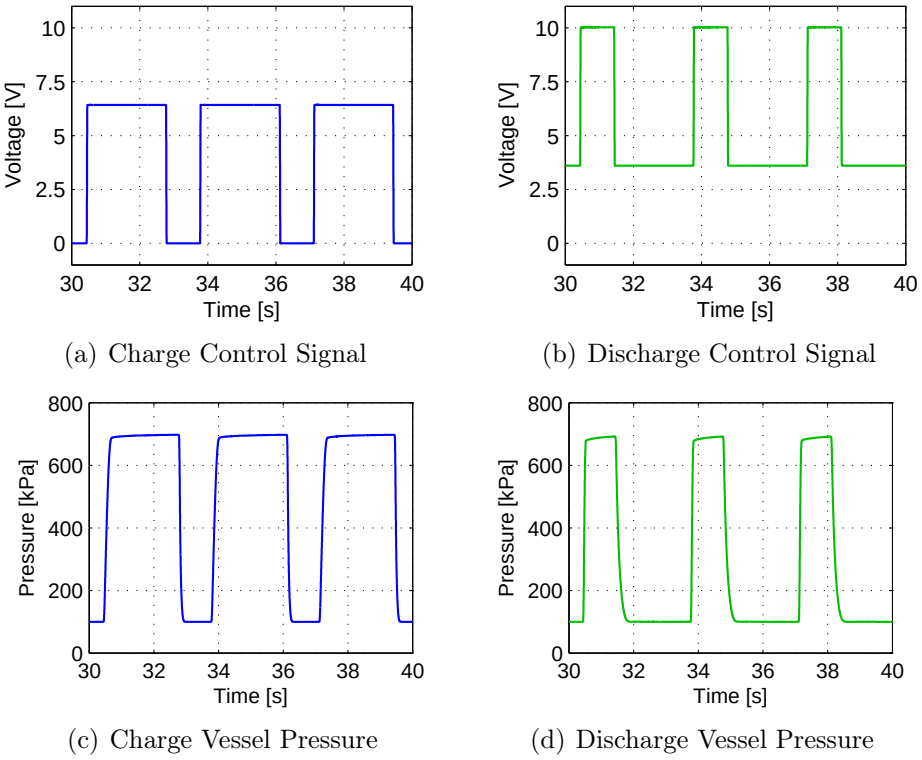

(a) Charge Control Signal

(b) Discharge Control Signal

(c) Charge Vessel Pressure

(d) Discharge Vessel Pressure

Figure 4.14: Channel A Cyclic Test Example

$$\dot{P}_v = \frac{RT}{V}\alpha_i \dot{m} \tag{4.20}$$

Where $\dot{P}_v$ is the pressure derivative in question, V is the chamber volume and α_i denotes the relevant α_{in} or α_{ex} term depending on the direction of mass flow. By considering only choked flow, and therefore substituting the relevant application of Equations 4.13 and 4.19 into Equation 4.20, the effective orifice area may be determined by solving the following relation:

$$\dot{P}_v = A_{eff}\, Cd \psi_{choked} P_u \alpha_i \frac{\sqrt{2RT_u}}{V} \tag{4.21}$$

For charging, the upstream pressure P_u is the supply, while the vessel pressure P_v is downstream. Note that for the choked flow case, the flow function ψ is a constant value, and Equation 4.4 therefore describes a relationship which is a function of P_u only. Should the upstream pressure, the supply in this case, be considered constant, the vessel pressure derivative $\dot{P}_v$ may be obtained by performing a least squares linear fit to the choked flow section of the data as shown in Figure 4.15(a), and determining the slope thereof. As mentioned in Appendix E the supply pressure did not, however, remain constant during testing, though the matter was resolved to some extent. Though the validity of this method may therefore be questioned, it was found that a model supplied

with parameters identified thus was able to accurately predict charging of the vessel even in the presence of sudden, large orifice openings which would result in the most severe supply pressure drops.

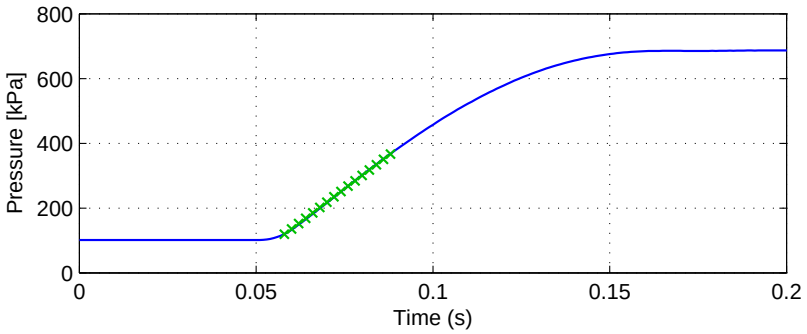

(a) Charge

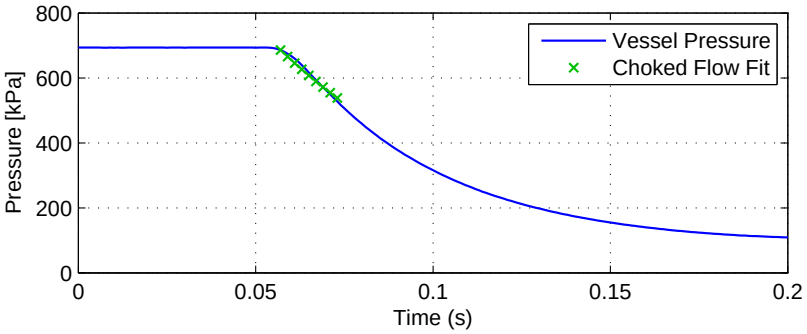

(b) Discharge

Figure 4.15: Choked Flow Fit

During discharge, the upstream pressure is that of the pressure vessel, which does not remain constant as air is exhausted. Bubert (2009) therefore describes a method which involves first taking the Laplace transform of Equation 4.20 with the choked flow case of Equation 4.13 substituted accordingly to yield:

$$P_v(s) = \frac{P_v(0)}{s + A_{eff}\, Cd\alpha_i\psi_{choked}\frac{\sqrt{2RT}}{V_v}} \tag{4.22}$$

Taking the inverse Laplace of Equation 4.22 the upstream- or vessel pressure may now be given as a function of time as follows:

$$P_v(t) = P_v(0)e^{-A_{eff}\, Cd\alpha_i\psi_{choked}\frac{\sqrt{2RT}}{V_v}t} \tag{4.23}$$

Here $P_v(0)$ is the initial vessel pressure value and time t is zeroed at the instant the chamber starts to discharge. Using Matlab's `lsqcurvefit` function, Equation 4.23 may be optimised for A_{eff} as illustrated in Figure 4.15(b).

The advantage of using this method is that it precludes discrete derivation of the vessel pressure data which may yield excessively noisy results in certain situations. It is, however, unsuited to the determination of the subsonic index as this parameter affects only the subsonic flow region and cannot be determined easily via inspection as might be the case for the pressure ratio terms b and a. Therefore, use of this method is limited to determining the effective orifice area in conjunction with the flow function ψ_e of Equation 4.19 where parameters a and β are set to unity and $\frac{1}{2}$ respectively. The pressure ratio b is either set equal to P_{cr} to denote the theoretical flow function of Equation 4.12, or determined based on inspection to approximate the effects of additional resistances present on the flow path, as per the ISO 6358:1989(E) standard's model.

An alternative approach intended to overcome the shortcomings of Bubert's method would be to optimise the unknown parameters of the model to produce the best data fit for a region of interest that includes both choked and subsonic flow. Using the data acquired with the experiments described previously, and once again considering the inlet and exhaust flow paths of each channel separately, Matlab's `lsqcurvefit` function may be used to optimise an orifice mass flow model by fitting Equation 4.21, where the ψ_{choked} term is replaced by the entire extended flow function ψ_e, to a discrete derivative of the vessel pressure curve.

As discussed previously, cyclically averaging the data results in a less noisy signal which may be further smoothed using a moving average filter given that the region of interest does not include high frequency components of importance. It was found that the discrete derivative could then be calculated in a manner that would not necessarily inhibit the parameter identification procedure if sufficient care is taken.

Still, while the current parameter identification approach may yet be influenced by signal noise, and while solving a number of variables simultaneously may additionally increase the solutions' sensitivity, this method has the advantage of lending itself to the investigation of either the theoretical, ISO or extended flow function models by merely substituting the values shown in Table 4.2 for each relevant case. The upper and lower limits of each parameter as fed to the `lsqcurvefit` function and that was found to yield the best results, are also shown.

Note that an attempt has been made to increase the robustness of the approach by predetermining the cracking pressure ratio as the maximum recorded value of the downstream to upstream pressure ratio, with an upper limit of unity. While this turned out to be a viable method to determine a for small orifice openings, care must be taken that the vessel pressure levels out at some constant value to ensure that the cracking pressure limit has indeed been reached for small-to-medium orifice openings. Furthermore, prior definition of the discharge coefficient also serves to preserve the robustness of this parameter identification method.

Table 4.2: Flow Function Model Parameters

	Flow Function Model			Parameter Limits	
Parameter	**Theoretical**	**ISO**	**Extended**	**Upper**	**Lower**
A_{eff}	Solve	Solve	Solve	1×10^{-2}	0
b	P_{cr}	Solve	Solve	P_{cr}	0
a	1	1	Solve	1	$\min\left(\frac{P_d}{P_u}\right)$
β	$\frac{1}{2}$	$\frac{1}{2}$	Solve	1	0

Figure 4.16 shows the values of the effective orifice area obtained in this manner for both channels, using the constant discharge coefficient determined based on the manufacturer's data (anon., 2006) in conjunction with the extended flow function case illustrated in Table 4.2.

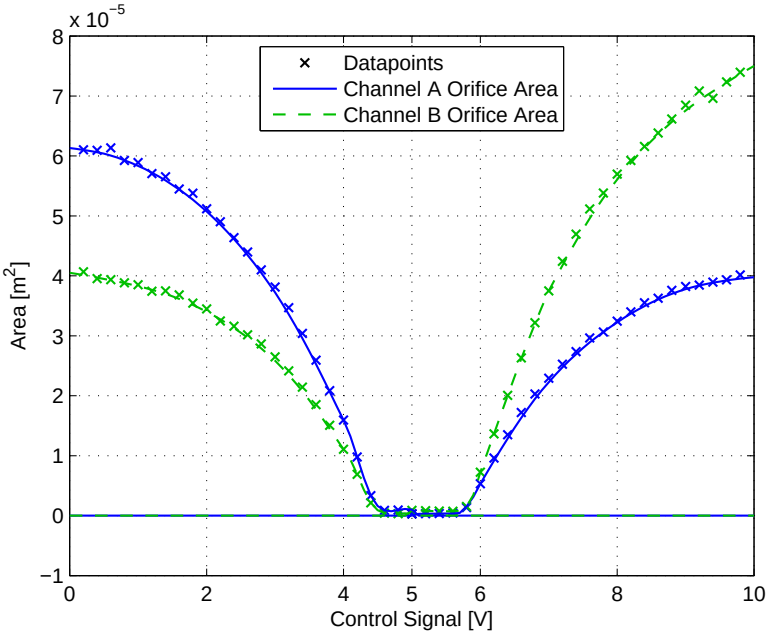

Figure 4.16: Effective Orifice Area

The discharge coefficient as given by Pugi *et al.* (2004) and Equation 4.14 was also implemented, yielding results similar to that of Figure 4.16, albeit of slightly lesser magnitude due to the correspondingly higher values of Cd when the effective orifice area is determined.

Note here the similarity between the shape of the curves of Figure 4.16 and that shown in Figure G.2 (Appendix G) namely the expected results based on an investigation of the valve's flow path geometry. The order of magnitude is similar in both cases, though the experimentally determined values are less by about half that produced by the geometric approach. This is due to the

additional restrictions introduced by the various fittings and other components on the flow path in question. These effects also manifest in the apparent asymmetric shape of Figure 4.16, as the restrictions differ for the inlet and exhaust paths. Most notably, the exhaust path contains a silencer to reduce noise when the system vents to the atmosphere, which the inlet path does not. Finally, a small offset from the intended neutral position at 5 V is noted, which in reality appears closer to 5.1 V.

The critical and cracking pressure ratios, as well as the subsonic index, remain within the bounds set for them, and do not justify plotting versus the control signal here. Refer to Tables I.3 to I.15 (Appendix I) for detailed lists of all identified parameters.

Finally, tests beyond the intended charge and discharge control signal ranges for each channel were not conducted. Such tests may serve to quantify the leakage present within the valve. If deemed necessary, the model is capable of accommodating simultaneous charge and discharge of a chamber as per Equation 4.4, and identification procedures similar to that presented here may be conducted to acquire the relevant parameters.

4.4.2 Validation

In order to verify the behaviour of the valve orifice model, the relevant equations and identified parameters for a single channel were implemented in Matlab's Simulink environment, the block diagram of which is illustrated in Figure 4.17.

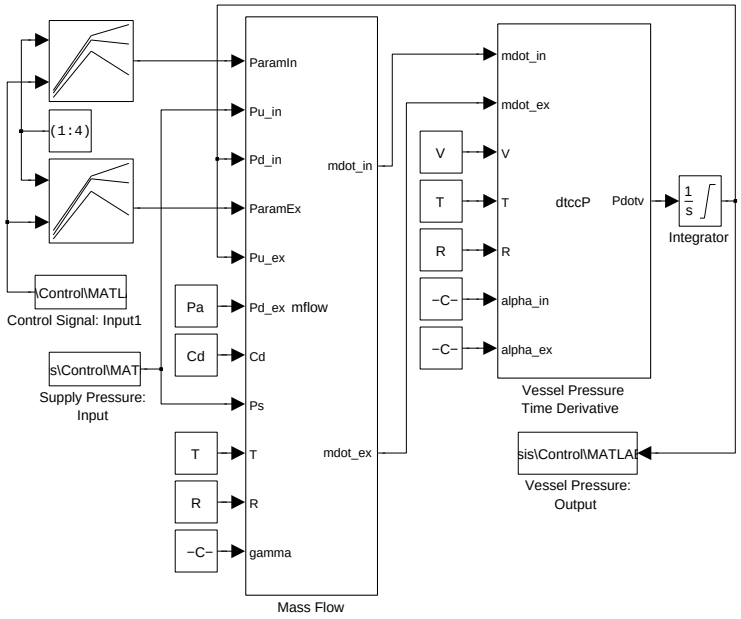

Figure 4.17: Aeff Test Setup Blockdiagram

The identified parameters' values were stored in the lookup tables `Aeff`, `b`, `a` and `ms`, where values pertaining to the inlet and exhaust flow paths are denoted by `in` and `ex` respectively. Parameter selection occurs via interpolation based on the input signal. Mass flow as per Equations 4.13 and 4.19 are modelled in the `mflow` block, while the fixed volume's rate of pressure change is calculated within the `dtccP` block as per Equation 4.20. Its output is numerically integrated to obtain the vessel pressure, and written to the specified output file. Inputs to the model are the cyclic averages of the control signal and supply pressure from the experimental data that is being evaluated.

The performance of the theoretical, ISO and extended flow function models were evaluated in conjunction with Equation 4.13 for both a constant *Cd* value as per the manufacturer's data, and that of Pugi *et al.* (2004). This was done by calculating the mean absolute error for the vessel pressure as per Equation 4.9 to obtain a single value illustrating goodness of fit between the relevant model and each experimental dataset used to identify the unknown parameters.

First, consider the results for the theoretical and ISO flow function models illustrated in Figures 4.18 and 4.19. Note that the *MAE* values are plotted against the relevant control signal investigated, similar to Figure 4.16. Also, each plot shows said errors obtained for charging and discharging of the specified channel, using both Festo and Pugi *et al.*'s discharge coefficients.

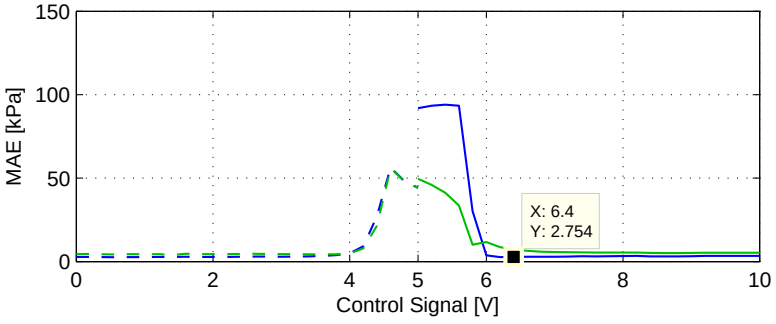

(a) Channel A

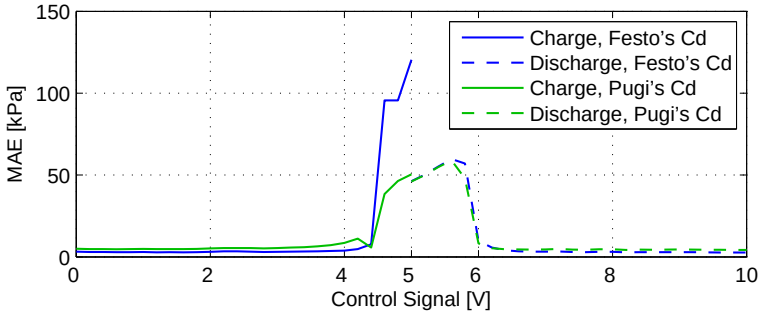

(b) Channel B

Figure 4.18: Theoretical Model Mean Absolute Error

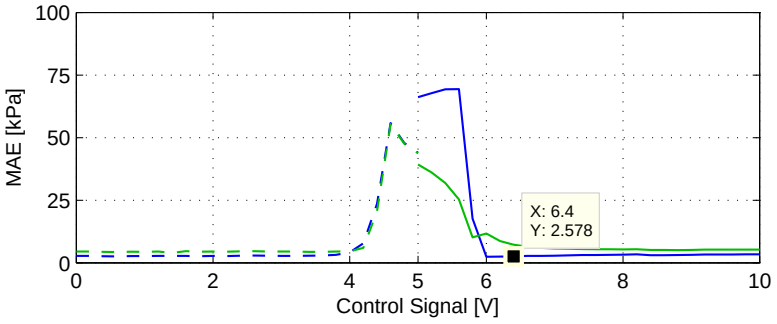

(a) Channel A

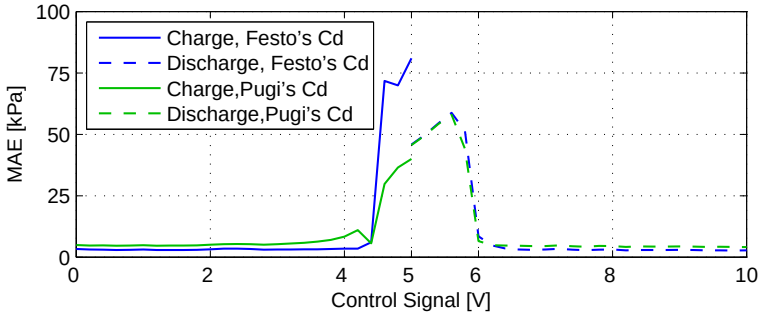

(b) Channel B

Figure 4.19: ISO Model Mean Absolute Error

It is apparent that both the theoretical and ISO model performs well for control signals resulting in medium to large orifice openings, with the constant Cd performing only marginally better than that of Pugi *et al.*. Here the MAE values remain typically well below 5 kPa, which is significant considering that the maximum vessel pressure is equal to that of the supply, namely 700 kPa. For smaller orifice openings, however, the situation severely deteriorates, where errors of more than 50 kPa are present.

The reason for this is that neither the theoretical nor the ISO model takes into account the effects of the cracking pressure, which manifests as the levelling off of the vessel pressure at a value lower than that of the supply as can be seen in Figure 4.20(a). Here only the theoretical model's output is illustrated, though that of the ISO model is similar. Again, mention is made of the supply pressure being set at 700 kPa for all tests performed here.

Furthermore, for vessel charging, the variable discharge coefficient of Equation 4.14 yields better results than a constant value, as can be seen by inspecting Figure 4.20(a) and the relevant sections of Figures 4.18 and 4.19. This may be due to the effect of Pugi *et al.*'s Cd approximating that of the cracking pressure ratio and the subsonic index, which becomes apparent when comparing Figures 4.11 and 4.12. It is possible, though, that the identified parameters for the theoretical and ISO models for the charging case of small orifice openings and a constant Cd may be negatively influenced by the optimisation technique

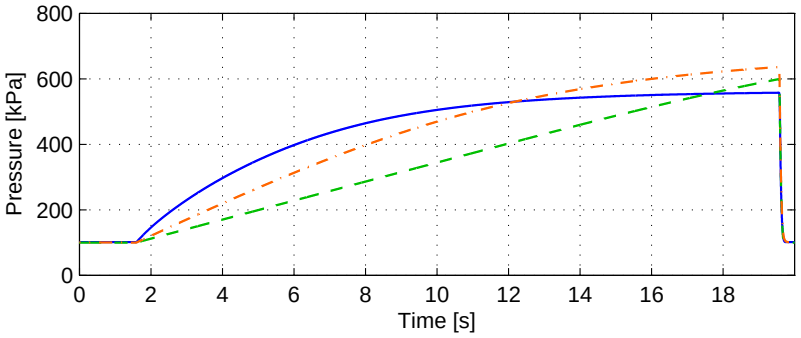

(a) Small Opening

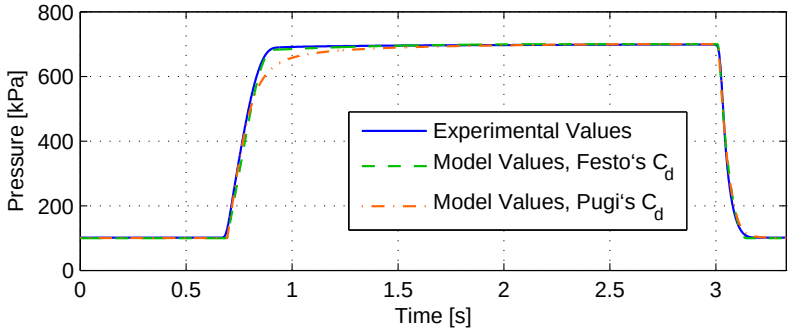

(b) Midsize Opening

Figure 4.20: Theoretical and ISO Model Verification

itself. This presumption stems from the fact that both Festo's and Pugi *et al.*'s discharge coefficients produce very similar *MAE* values for discharge in both models.

Still, the discrepancy between a model with Pugi *et al.*'s discharge coefficient and the actual data remains large, as the discharge coefficient is dependant on the orifice in question's geometry (Beater, 2007). Equation 4.14 therefore probably only holds for the specific orifice used to evaluate it, and is therefore less applicable to valves with differing geometry. Even so, reference to this relation still appears in literature (Beater, 2007; Bubert, 2009).

Figure 4.20(b) shows the theoretical model's result compared to the experimental data for medium to large orifice openings. As mentioned, the ISO model performs similarly within this region, as becomes evident by inspecting the data-points added to Figures 4.18 and 4.19. This is significant in that the introduction of a variable critical pressure ratio as per the ISO 6358:1989(E) standard does not appear to significantly improve the flow function's ability to adequately affect the predicted mass flow, at least for medium to large orifice openings and short pipe lengths.

Furthermore, for such orifice openings, a model using Festo's *Cd* better approximates the test results during the final stages of pressure vessel charging, as is evident from Figure 4.20(b). As mentioned previously, Pugi *et al.*'s

discharge coefficient affects flow within the subsonic region, thereby further decreasing the output beyond the reduction introduced by the flow function itself. This therefore is manifested as an under-estimation of the vessel's rate of pressure change.

The *MAE* values of the extended flow function model are shown in Figure 4.21. While the errors for medium to large orifice sizes are similar to that of the theoretical and ISO models, the discrepancies between the modelled and experimental data are significantly lower in this case for control signals close to the neutral value of 5 V.

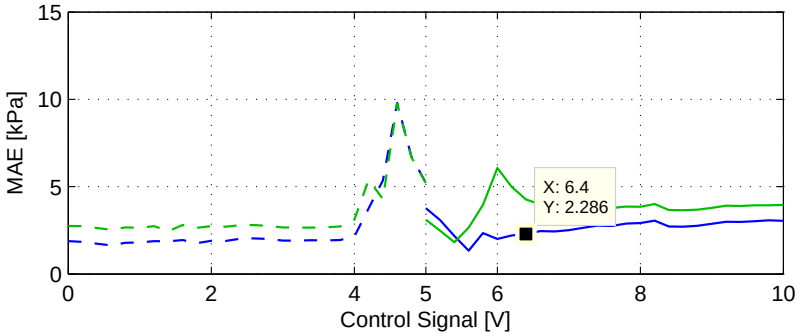

(a) Channel A

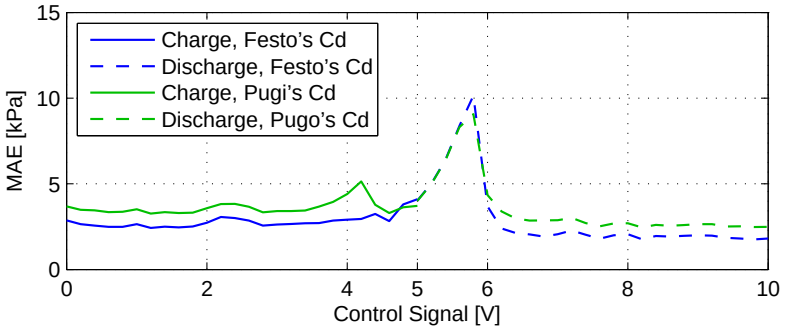

(b) Channel B

Figure 4.21: Extended Model Mean Absolute Error

Illustrated in Figure 4.22(a) are the extended model's predicted values superimposed on the test results for a small orifice opening. Excellent agreement is noted for both the constant and variable *Cd* parameters. Also, the levelling off of the vessel pressure at a value lower to that of the supply is properly modelled by the inclusion of the cracking pressure ratio term a. As previously mentioned, this term is determined by setting a equal to the maximum value of the downstream to upstream pressure ratio, should said maximum be less than one. Premature discharge of the vessel may therefore result in the cracking pressure being set to a erroneous value, as the pressure within the vessel would have continued to rise had it been allowed to. This may be the source of the

spikes within the plotted curves of Figure 4.21. The case illustrated here, however, shows that determining the cracking pressure ratio as described is indeed a viable method if adequate care is taken during experimental test procedures.

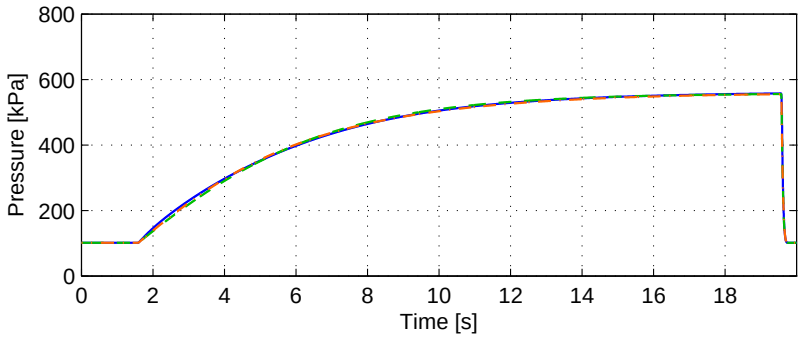

(a) Small Opening

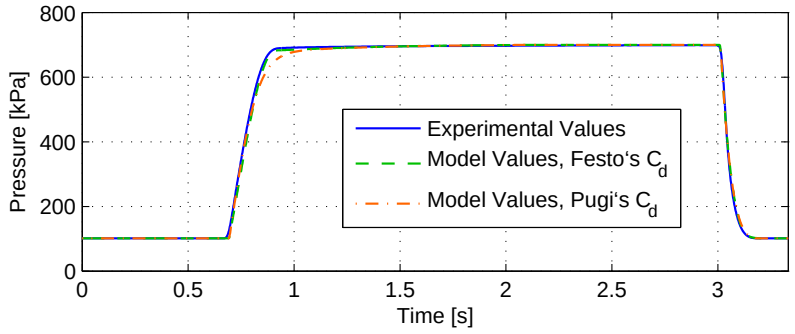

(b) Midsize Opening

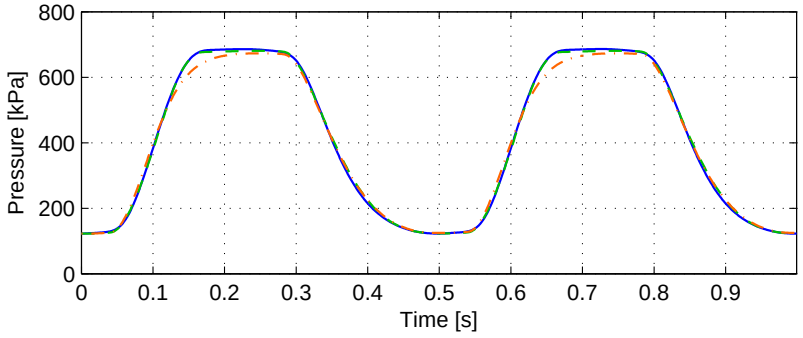

(c) Cyclic Input

Figure 4.22: Extended Model Verification

Figure 4.22(b) shows the same model's results for a mid-sized orifice opening. Again, both Festo and Pugi *et al.*'s discharge coefficients result in good agreement of the predicted and experimental results, though, as before, the constant *Cd* parameter performs better within the final stages of vessel charging. It is of interest to note that this particular discrepancy only manifests

itself for pressure ratios approaching unity, as this is the range which Equation 4.14 most severely affects, as per Figure 4.11. For small orifice openings that display the cracking pressure characteristic, this effect of Pugi *et al.*'s *Cd* would therefore be negated, as is evident from Figures 4.20(a) and 4.22(a).

Continuing, the extended flow function model's ability to predict the result of a dynamically varying input signal was briefly investigated, and shown in Figure 4.22(c). Here a sinusoidal control signal with an amplitude of 2.5 V about the 5 V neutral position bias was applied. The frequency was set to 2 Hz in order to evaluate the response at the expected operating conditions prevalent during the performance of wear tests, as per Chapter 3.

Festo's discharge coefficient outperforms that of Pugi *et al.*, with a mean absolute error of only 3.88 compared to a value of 11.61. In fact, this is the case in general for the extended model, as is evident from the *MAE* plot of Figure 4.21. Therefore, the potential advantage that a properly identified variable *Cd* has over a constant value for said parameter in the theoretical and ISO models is negated by the introduction of the a and β terms. The only apparent benefit that identifying the discharge coefficient as a function of the pressure ratio has for a given orifice would therefore be to model some effect within the choked flow region, which the cracking pressure ratio and subsonic index do not directly influence.

So, to conclude this section, the extended flow function as per Equation 4.19, in conjunction with the mass flow relationship of Equation 4.13 and a constant discharge coefficient determined based on the manufacturer's data, is thus considered the most appropriate model for the purpose of this thesis. Identification of this model is done by simultaneously optimising the effective orifice area, the critical pressure ratio and the subsonic index parameters, with the cracking pressure ratio predetermined as discussed, to fit the vessel pressure data for both inlet and exhaust flow of each channel. Additionally, setting the relevant parameter values to that listed in Table 4.2, the theoretical and ISO models may be identified, though these models agree less well with the data than the extended model.

4.5 Connecting Tube Model

Flow through connection tubing experiences a decrease in energy due the presence of friction. Though there are various approaches to modelling of tubes (Richer and Hurmuzlu, 2000; Beater, 2007; Bubert, 2009), the extended flow function model lends itself well to the representation of the amplitude attenuation mass flow undergoes within long lines (Harris *et al.*, 2011). Therefore, following the procedure outlined previously, the respective tubes and valve orifices may be modelled as a cascaded system by merely including the tube itself during the parameter identification procedure.

The tubes used for this work are kept short by locating the valve close to the pressure vessel and, eventually, the pneumatic cylinder. Their effects on the overall system is therefore small enough as to be negligible. For the purposes of illustration however, refer to Figure 4.23, which shows the extended model fitted to a system with a 5.5 m long tube connecting the valve and cylinder in a setup similar to that of Figure 4.13. Tables I.16 and I.17 (Appendix I) list the relevant identified parameters.

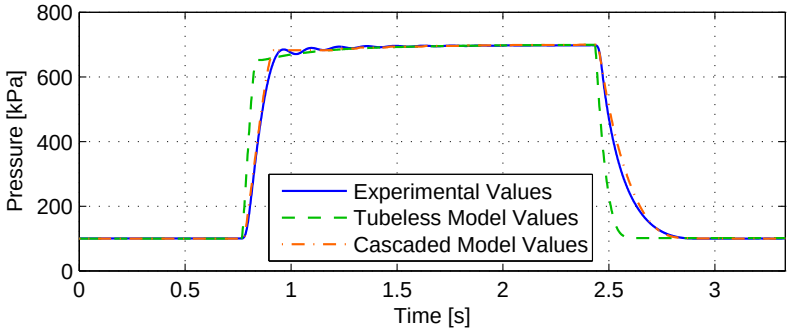

Figure 4.23: Connecting Tube Model Comparison

Note that the predicted values of a model that has been identified without including the tube effects do not compare well with the experimental data, while those of the model fitted specifically to said data performs better. An additional advantage of this type of modelling approach is that all effects of connectors and, in the case of exhaust lines, the silencers, are included by extension.

Drawbacks relating to cascaded modelling of a pneumatic system using Equations 4.13 and 4.19 are, firstly, its inability to account for reflection from the end of the tube occurring for large, sudden valve openings, manifesting as oscillations which may be detected on the vessel pressure curve of Figure 4.23. Secondly, should the system be changed by, for instance, using a different length or diameter tube, parameter identification has to be repeated for the new setup. A cascaded modelling approach is, of course, inherently non-modular.

To continue, not yet mentioned is the required addition of a delay term, as mass flow propagating as a wave along a tube requires a finite amount of time to reach its end. Again, this only becomes significant for greater tube lengths, and a constant delay equal to $\frac{L_t}{c}$ is suggested (Richer and Hurmuzlu, 2000; Bubert, 2009; Harris *et al.*, 2011).

Finally, the definitions of 'long' and 'short' tubes are somewhat unclear. As mentioned, Figure 4.23 illustrates the effects of a 5.5 m tube, compared to a model with parameters identified based on a short tube of less than 10 cm. Clearly 5.5 m may be considered 'long', and 10 cm 'short'. Tubes of up

to half a metre were also used, and was found to correspond well to results obtained with the 10 cm tubes. Tube diameter and wall roughness may further influence any attempt at such a descriptive classification of pneumatic tubing. It is therefore concluded that, while it may be difficult to identify a clear boundary between 'short' and 'long' tubes, best practice would simply be to identify the orifice model parameters with the pneumatic circuit - tubes and all - set up as it will be applied in practice.

4.6 Pneumatic Circuit Model Integration

The pneumatic circuit of Figure 4.1 is modelled in Simulink as shown in Figure 4.24. Here the extended mass flow model of Equations 4.13 and 4.19 is recreated in the `mflow` block, the relevant identified parameters stored in two-dimensional lookup tables. The lookup tables receive as input control signals as recorded during experimental testing. The chamber pressure derivative model of Equation 4.4 is accounted for by the `dtccP` block, while the `acc` component accounts for the actuator's dynamics, the piston force and friction effects as per Equations 4.2, 4.3 and 4.8 respectively. The `sparam` variable contains the identified parameters of the Stribeck curve.

The output from the `mflow` block is directly fed to the chamber derivative `dtccP` block's input, its result in turn being integrated to obtain the respective chamber pressures. Additional inputs to Equation 4.4 are the piston's position and velocity. The `acc` block, upon receiving the chamber pressure values, solves Equation 4.2 to obtain the piston's acceleration as output, with friction determined from the piston's current velocity. Finally, acceleration is twice integrated to solve for the piston's displacement. The `acc` block also outputs piston and friction force values for evaluation purposes.

4.6.1 Validation

In order to first investigate the use of the chamber pressure derivative model, consider the case of a setup as per Figure 3.7 where the actuator's piston is fixed at zero displacement. Load applied to the piston is estimated from Equation 4.3, and its discrete derivative taken for comparison to Equation 4.4's output. While discrepancies in the valve orifice flow model may influence the pressure derivative model's accuracy, effects due to friction are negated as the velocity is kept at zero.

Applying a sinusoidal signal to the valve, the results as per Figure 4.25 are obtained. Apart from noting good agreement between the model output and the data, it is apparent that the actuator in conjunction with the valve appear capable of meeting and exceeding the maximum force requirement of 265 N and the relevant rate of change of 8.34 $kN.s^{-1}$ while maintaining a dominant frequency component sufficiently close to 2 Hz, as per Table 3.4 in Chapter 3.

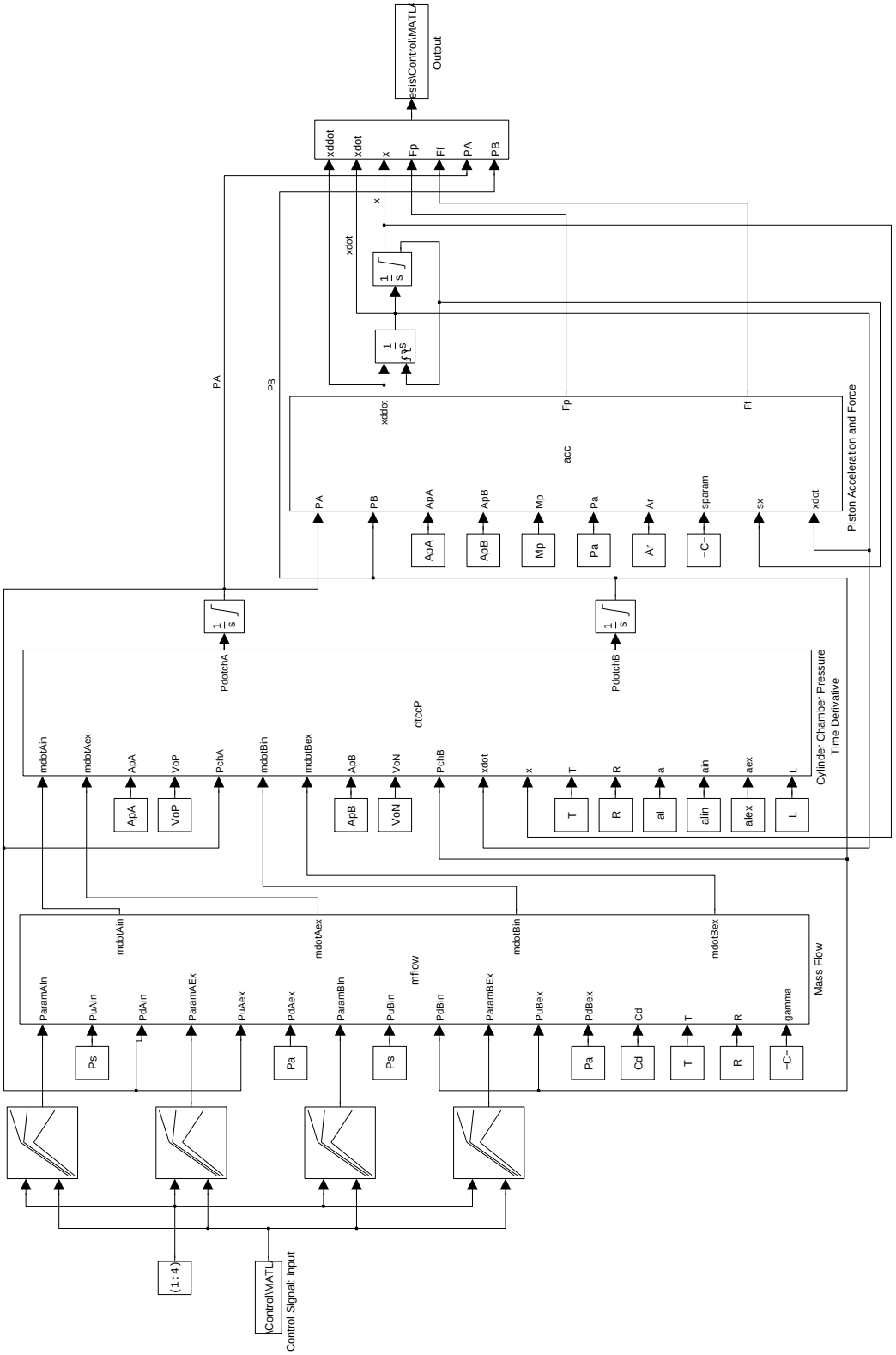

Figure 4.24: Pneumatic Circuit Blockdiagram

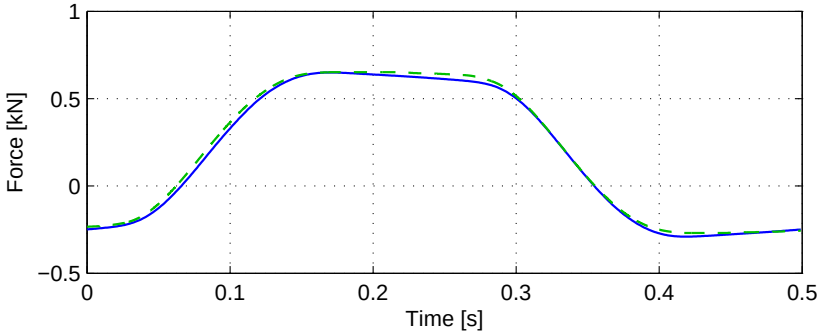

(a) Piston Force

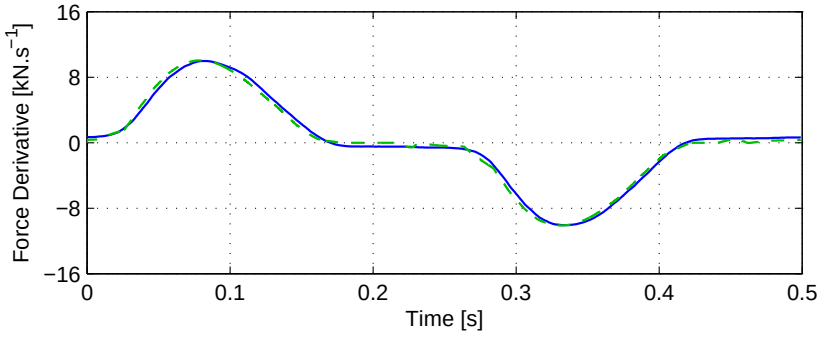

(b) Piston Force Derivative

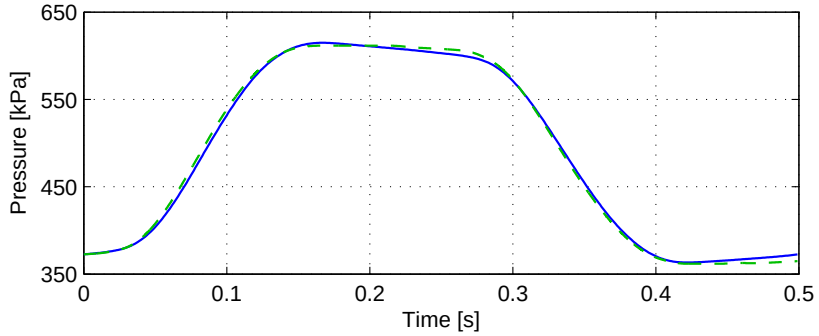

(c) Chamber A Pressure

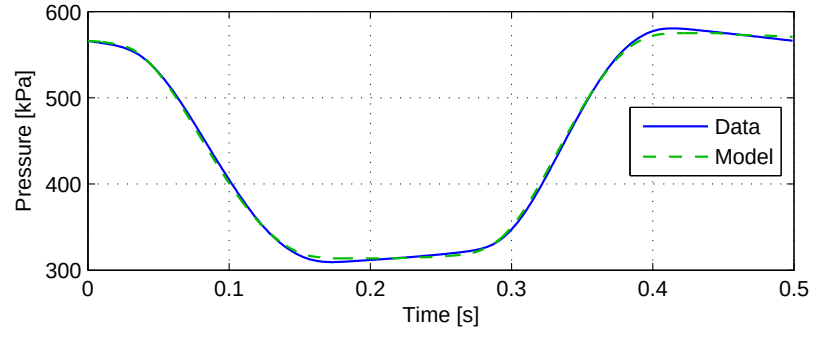

(d) Chamber B Pressure

Figure 4.25: Pneumatic Circuit Dynamic Load Verification

Using the data obtained for the fixed-rod case, values for the dead-volumes at the piston's stroke ends and within the fittings, may be estimated via inspection. This is done by either increasing or decreasing the parameter values to obtain the best fit between the data and modelled chamber pressures. Listed in Table I.1 (Appendix I) is a single dead-volume value for each of the channels A and B, though separate values for use during inlet and exhaust may yield more accurate results as the flow-paths' geometry differs in each case.

Furthermore, tests were conducted with the rod free to move as per Figure 4.1 and a square wave control signal input to elicit predominantly quasi-static behaviour from the system. This allows verification of the model as a whole while negating the un-modelled effects of the pre-sliding regime and frictional lag to a large degree. The results of such a test for positive velocity is illustrated in Figure 4.26, with negative velocity exhibiting similar behaviour.

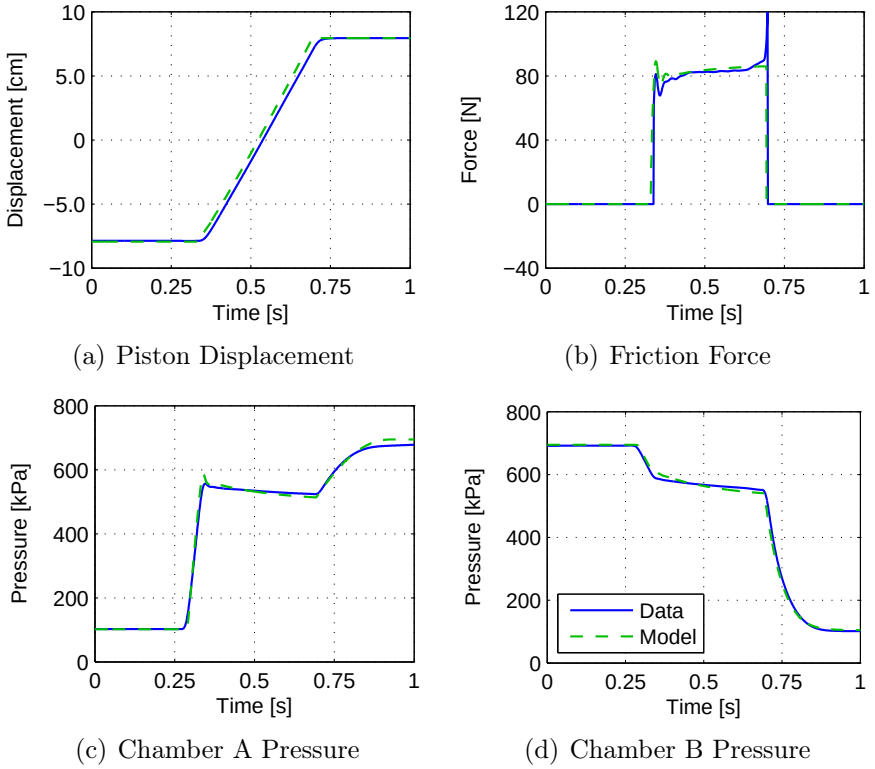

(a) Piston Displacement

(b) Friction Force

(c) Chamber A Pressure

(d) Chamber B Pressure

Figure 4.26: Pneumatic Circuit Quasi-Static Verification

While good correlation between the model estimate and recorded data is achieved, the data follows the relevant prediction by a small time delay. The discrepancy's source may be attributed to un-modelled aspects previously assumed negligible such as valve-spool dynamics, mass flow time-delay (not implemented in this case since the tubes were initially considered short), and transient friction components present at the commencement of displacement.

Last mentioned may have a significant effect even for the quasi-static scenario, as displacement is determined by twice integrating the acceleration term solved from Equation 4.2. This was found to be the case when other datasets were evaluated.

Finally, though the friction model is expected to inadequately reproduce dynamic behaviour as discussed previously, the overall model's output is nevertheless compared to data elicited from the system in response to a varying control signal input. Said signal was sinusoidal, with the frequency and amplitude selected to ensure that the maximum required displacement and speed is met or exceeded while the displacement exhibits a dominant frequency component of 2 Hz. This then demonstrates the physical circuit's ability to attain ISO protocol as per the relevant section in Chapter 3. The results are shown in Figure 4.27, with the friction-velocity map obtained from this specific dataset illustrated in Figure 4.9.

As anticipated, poor tracking is exhibited by the friction force estimation plotted in Figure 4.27(b). This error is magnified in the position signal of Figure 4.27(a) due to twice integrating acceleration determined from Equation 4.2. Since the pneumatic circuit's behaviour is reproduced by an integrated system model, errors are easily transferred between its various components, as is evidenced in the chamber pressure plots of Figures 4.27(c) and 4.27(d) compared to those of Figures 4.25(c) and 4.25(d).

To conclude, this section discussed the procedures followed to validate the overall system model. Good results were obtained for the case in which the cylinder's rod was fixed, suggesting compliance with the requirements listed in Chapter 3. For the quasi-static scenario, adequate tracking is evidenced for the data presented. The integrated model deteriorates, however, in the presence of frictional lag during gross-sliding and significant pre-sliding regime behaviour during inversion and cessation of velocity.

Mention must additionally be made of the integrated model's sensitivity to variations in the input control signal. Slight discrepancies due to sampling errors and interpolation/extrapolation of the lookup tables have been found to have a detrimental effect on model behaviour, particularly piston displacement. Additional errors may be introduced by inaccurate selection of initial conditions. Sufficient care must therefore be taken when the current model is used during controller design in order to ensure effects of aforementioned sensitivities are adequately negated.

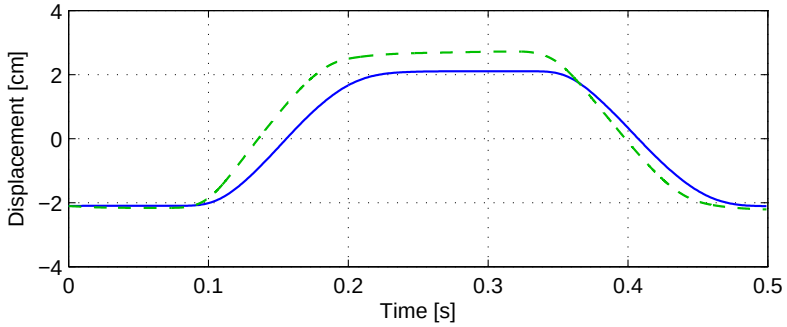

(a) Piston Displacement

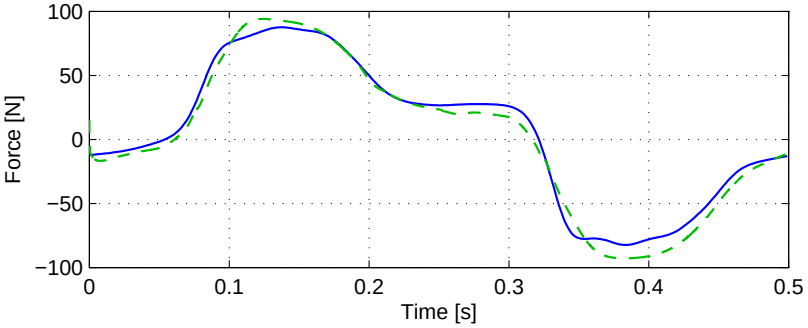

(b) Friction Force

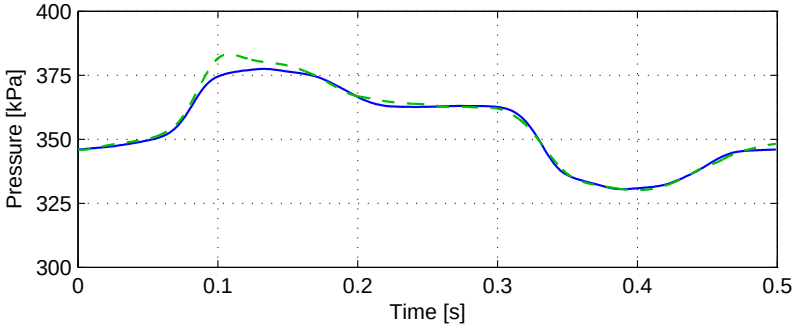

(c) Chamber A Pressure

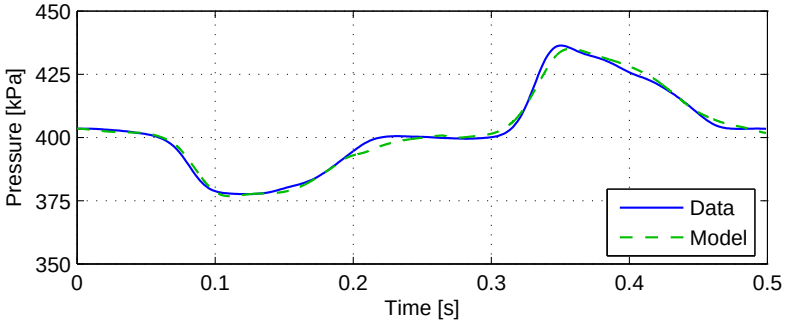

(d) Chamber B Pressure

Figure 4.27: Pneumatic Circuit Dynamic Displacement Verification

Chapter 5

Conclusions and Recommendations

As per Chapter 1, the motivation from which the individual objectives stem is the continued development of the Stellenbosch University joint-type knee wear simulator. The first section of this chapter, therefore, is concerned with the manner in, and extent to which, each of the individual objectives are met. Following this is a discussion outlining suggested future work, with the chapter drawn to a close by the final conclusions.

5.1 Attainment of Objectives

5.1.1 Objective 1

Achieving the first objective is intended to aid simulator development by presenting a thorough review of design-related aspects of such machines. Chapter 2 is devoted to satisfying said aim entirely, while additionally presenting the reader with relevant background information.

Discussed is the ISO 14243 series of standards' coordinate system, adapted from Grood and Suntay (1983), which allows description of applied loads and motions of a three dimensional structure. Thereafter, the various control methodologies applicable to wear simulators as well as their advantages, drawbacks and, to an extent, their origins are presented. In many instances such knowledge is critical not only to simulator design, but also during test protocol development. This is because reproducing physiologically relevant kinetics and kinematics are dependent on implant geometry, which in turn affects the success of the selected control technique. Furthermore, wear tests based on load control requires the additional simulation of soft-tissue restraints. Different methods to implement such considerations are discussed, and while *in-silico* modelling appears to be the most flexible technique, uncertainty as to the exact laxity models and values to be used is illustrated for considera-

tion. Following this, requirements and difficulties of adequate environmental conditioning is presented, subsequent to a discussion regarding the merits and drawbacks of electromechanical, hydraulic and pneumatic simulator actuation. Work towards the first objective is then concluded with a tabulated comparison of commercial join-type knee wear simulators in terms of the design features previously mentioned.

5.1.2 Objective 2

Simulator development is furthered in a more direct manner by work intended to satisfy the second objective, namely the advancement and use of electronic hardware, software and safety subsystems. The physical aspect of such work is detailed in Chapter 3's relevant sections.

After an overview of the previously completed mechanical and pneumatic subsystems' design, new work regarding the electronic hardware is presented. It was found that the selected data acquisition unit was unsuited to real-time control applications, and a viable alternative was suggested. The DAQ subsystem as it is, however, proved adequate for data capture purposes. Last mentioned observations were made during use of an experimental setup detailed within said chapter for experimental validation and parameter identification purposes as per Chapter 4. Finally, safety precautions are shown to have been designed and implemented within the relevant section of Chapter 3, thereby finalising attainment of the second objective as listed in Chapter 1.

5.1.3 Objective 3

Satisfaction of the third objective is illustrated in two parts, the first of which relates to the derivation of performance requirements against which the individual pneumatic circuits may be evaluated.

Such an investigation is intended to illustrate said components' ability to attain ISO protocol as part of the integrated system, prior to its completion. The approach followed assumed that each profile to be actuated has three interrelated measures that must be satisfied simultaneously. These are the overall magnitude of the profile, the maximum rate of change thereof and its dominant frequency component. The procedure and the specific values obtained are detailed in the relevant section of Chapter 3. To illustrate, by considering the load profile describing A/P actuation as per the ISO 14243-1:2009 standard, the required magnitude is 265 N with the the maximum rate of change being 8.34 $kN.s^{-1}$. By considering the frequency content of each profile, the dominant component was identified at 2 Hz.

Secondly, in order to investigate adherence of a pneumatic circuit's behaviour to the previously discussed performance measures, a versatile test setup has been designed and illustrated in Chapter 3. This setup comprises

subsystems intended for use within the simulator as a whole, while data logging is managed by a LabView VI specifically written for the task. Throughout Chapter 4 use of said device to validate the performance of the A/P circuit as well as its models is subsequently illustrated.

Referring to Figure 4.25 (Chapter 4), the A/P circuit's ability to conform to the required maximum load magnitude and rate of change is illustrated in the presence of a sinusoidal signal. Said signal elicits dynamic behaviour that exhibits a dominant frequency component of 2 Hz. This test is conducted with the piston-rod assembly's position fixed in place. It was found that both the load magnitude and rate of change requirements of respectively 265 N and 8.34 $kN.s^{-1}$ are exceeded. Figure 4.27 within the same chapter shows data obtained in a similar manner, but with the piston-rod allowed to move unrestricted. Subsequently, the observation is made that the required displacement and velocity magnitudes of 5.17 mm and 53 $mm.s^{-1}$ are met.

A drawback of the approach used is that the A/P circuit's ability to affect load and displacement was validated in tests which were respectively fixed positionally and un-loaded. This is contrary to the real-world scenario, as both motion and external forces are present regardless of the control methodology implemented. The reason for the approach taken was that it served as an initial method to investigate adherence to performance requirements without complicating the procedure by introducing additional unknowns.

To conclude then, it was demonstrated that the A/P circuit is able to meet the performance requirements listed in Table 3.4 (Chapter 3), for the sufficiently simple fixed and unloaded cases respectively. Whether or not such tests adequately reflect eventual system behaviour remains to be seen, but insight may be obtained from the approach as detailed here. If the circuit was unable to meet the requirements for such simple cases, it is safe to assume it would perform even less well as part of an integrated system and must be redesigned accordingly. An alternative approach to simulating the individual circuit's performance physically would, of course, be to do so *in-silico* once an adequate model has been obtained, as discussed in the following section.

5.1.4 Objective 4

The final objective is concerned with the development of models that are able to adequately reflect a real-world servo-pneumatic circuit's response. As mentioned in the previous section, such models may be used to evaluate a particular design's performance on component, subsystem and with further study, system levels. An increased understanding of parameters which affect simulator behaviour may also lead to more efficient work, not to mention the value accurate models would have in terms of control system design. The theme of continued simulator development is thus carried on in work aimed at satisfying the fourth objective. Chapter 4 describes in detail selected models, relevant parameter identification procedures and validation.

Presented initially are various components comprising a servo-pneumatic circuit which require modelling, followed by a discussion on assumptions and their validity concerning the energy transfer medium, namely air. For the range of temperatures and pressures prevalent in this work, the ideal gas law is considered adequate (Beater, 2007).

Concerning the actuator, the first model detailed is that describing the piston-rod assembly's dynamic behaviour as per Newton's second law. Included terms are the inertial component, friction force and piston loading. Last mentioned is a function of the chamber pressures either side of the piston. The force exerted by each chamber is dependent on the relevant surface areas which are not necessarily equal. The model describing the rate of change for said pressures is presented by Equation 4.4, with inputs such as mass flow rate, piston displacement and velocity. Taken into account are the differing heat transfer characteristics for the charging and discharging cases, as well as the effect of dead-volume present in the cylinder at stroke ends and fittings. Equation 4.4 is shown to yield accurate dynamic response in Figure 4.25, even though concern is expressed in literature regarding its simplified nature (Carneiro and de Almeida, 2006*b*). Temperature was assumed to remain constant during actuation, and the various other parameters were readily determined from either literature or the manufacturer's datasheets.

The piston and rod's seals' friction was then considered, and modelled using a quasi-static approach. A parameter identification procedure in which the piston is displaced at a predominantly constant velocity is presented and validated. It was found that the velocity remains sufficiently constant for a fixed orifice opening, with the Stribeck curve's parameters identified thus correlating well with experimental data for medium to higher velocities, as shown in Figures 4.7 and 4.8 respectively. For lower velocities the model's behaviour deteriorated due to the convex, as opposed to an intended concave shape of the transition between the partial and full fluid lubrication regimes, as may be seen by comparing Figures 4.4 and 4.6. The Stribeck component was forcefully converted by the solver to a velocity-strengthening as opposed to a velocity-weakening term by consequent parameter selection. Modification of said function and its relevance is presented shortly thereafter.

Continuing the discussion regarding friction model behaviour, its validity in the presence of an input eliciting dynamic behaviour is investigated. As evidenced by the friction-velocity maps of Figure 4.9, the quasi-static model is unable to account for frictional lag manifested as an overestimation of the Stribeck model during acceleration and its underestimation for de-acceleration. It is also suggested in literature that the pre-sliding regime's effects may become significant during cyclic inversion and cessation of velocity (Tjahjowidodo *et al.*, 2007), another un-modelled aspect of the quasi-static model.

The next component considered for modelling is the valve. After a summary of relevant model theory, a procedure more suited to identification of a proportional valve's model parameters than that of the ISO 6358:1989(E)

standard is presented. Afterwards, the theoretical, ISO and extended flow function models as per Equation 4.19 and Table 4.2 are compared as all three models appear often in literature. It was found that the extended model as identified yielded the best results, especially for small orifice openings as it takes into account the effects of cracking pressure as illustrated in Figures 4.21 and 4.22(a) respectively. The theoretical and ISO models performed similarly, regardless of the theoretical model's inability to effect the downstream to upstream pressure ratio reduction evidenced by a series concatenation of orifices, as is the case for many commercial proportional valves.

Another parameter used for determination of mass flow through an orifice by Equation 4.13 is the discharge coefficient. Though this coefficient is essentially a function of the downstream to upstream pressure ratio (Pugi *et al.*, 2004; Beater, 2007), many works including the ISO 6358:1989(E) standard details use of a constant. Evaluated thus is the use of either a constant or variable function as the discharge coefficient. The constant value was found to be not only easily identifiable, but also to yield accurate results if used in conjunction with the extended flow function model. Said observation, as well as the resulting orifice model's adequate dynamic performance for a 2 Hz input signal, is illustrated in Figure 4.22(c).

It is furthermore suggested in the relevant section that, for long tubes where mass flow attenuation due to flow resistance becomes significant, orifices and tubes be modelled as a concatenated series of orifices during the same identification procedure. An additional delay term is introduced, equal to the time it is estimated that a mass flow wave takes to propagate through the length of the tube. These effects are illustrated in Figure 4.23. Since the tubes in this work are kept short by mounting the valve close to the actuator, the time delay term is assumed negligible.

Finally, the dynamic performance of the integrated models are evaluated. First, the model estimate is compared to recorded data for the fixed piston-rod case as per Figure 4.25. This effectively considers only the valve and cylinder chamber models, which illustrates good correlation. Allowing unrestricted motion of the cylinder's rod, and applying a square wave signal to elicit predominantly constant displacement thereof, the quasi-static friction model may then be investigated. While the results presented appear to correlate well with the specific dataset, it was found that this is not always the case. At the instant when displacement commences, transient signal components dominate the response - components which the friction model as presented does not take into account. Since velocity and displacement are determined from integration of the piston's acceleration, which is in turn solved from the dynamic model of Equation 4.2 in which friction force is a parameter, inaccurate estimation of the initial friction force would result in propagation and amplification of the subsequent error. Continuing this line of thought, it is shown that the quasi-static friction model is unsuited to reproducing dynamic system behaviour, as evidenced in Figure 4.27.

5.2 Recommendations for Future Work

Much effort still needs to be expended before the simulator will function as a whole. Currently, the only viable direct improvement to its design would be the acquisition and implementation of a controller capable of real-time input-output and data acquisition. The need to first identify and investigate the various pneumatic circuits on a subsystem level precedes any further work on the simulator as a whole, as such a study might lead to a redesign of the complete system.

Concerning the experimental setup used to investigate the performance requirements, adding the ability to perform loaded tests may yield useful insight in terms of system and model behaviour. While all tests were cyclic in nature to allow data averaging, inter-test repeatability remains to be investigated. Furthermore, the piston force was estimated based on the difference between the chamber pressures, with the friction force solved from Equation 4.2 as per Andrighetto *et al.* (2006). Greater accuracy may be achieved if tests are designed in which such values may be measured in a more direct manner. For instance, considering the fixed-piston scenario outlined previously, a load cell could be used to measure piston force. An additional improvement includes mounting an accelerometer to the cylinder's rod, negating the need to derive displacement and the resulting velocity profiles to obtain acceleration information. This has been shown effective by Nouri (2004). Finally, should the effects of pre-sliding be investigated, a position sensor of greater accuracy than the LVDT currently used is required, at least for a limited range of displacement.

Various aspects that are not explicitly accounted for in this thesis may influence behaviour of the models, and should be considered in future endeavours. Included are the effects of leakage within the valve and cylinder chambers, variations in pressure on the friction force of the piston's seals and sampling and time delay errors introduced by the control and valve electronics. The most significant of such aspects are, however, the transient effects of friction. As has been discussed, quasi-static models cannot account for frictional lag during gross-sliding and the behaviour of the pre-sliding regime. Adequate identification and implementation of a suitable dynamic friction model, such as that of Al-Bender *et al.* (2005), would therefore be invaluable to modelling the various pneumatic circuits' behaviour.

Once the integrated pneumatic circuit model displays adequate tracking of dynamic behaviour, and following the identification of all relevant circuit components' parameters, a model detailing the simulator as a whole may be assembled. This would prove useful for continued design validation and non-linear controller development. Previously identified performance requirements may also be evaluated and refined.

5.3 Conclusion

The author is of the opinion that work detailed in this study is in line not only with the objectives as outlined in Chapter 1, but also the overarching theme of continued simulator development. The significance of this theses is in the thorough documentation of literature, theory and design aspects relating to joint-type simulators. The contribution thus made would, in the least, serve as an in-house guide to future work concerning knee wear evaluation devices, both in terms of their design and application to research.

List of References

Affatato, S., Leardini, W., Rocchi, M., Toni, A. and Viceconti, M. (2008). Investigation on wear of knee prostheses under fixed kinematic conditions. *Artificial Organs*, vol. 32, no. 1, pp. 13–18.

Al-Bender, F. (2010). Fundamentals of friction modeling. In: *Proceedings, ASPE Spring Topical Meeting on Control of Precision Systems, MIT, April 11-13, 2010*, pp. 117–122.

Al-Bender, F., Lampaert, V. and Swevers, J. (2005). The generalized maxwell-slip model: a novel model for friction simulation and compensation. *Automatic Control, IEEE Transactions on*, vol. 50, no. 11, pp. 1883–1887.

Al-Ibrahim, A. (1991). *Transient air temperature and pressure measurements during the charging and discharging processes of an actuating pneumatic cylinder*. Ph.D. thesis, University of Wisconsin–Madison.

Ali, H., Noor, S., Bashi, S. and Marhaban, M. (2009). A review of pneumatic actuators (modelling and control). *Australian Journal of Basic and Applied Sciences*, vol. 3, no. 2, pp. 440–454.

American Academy of Orthopaedic Surgeons (1995). *Knee replacement implants*. [Online] (Reviewed September 2010) Available at: `http://orthoinfo.aaos.org` [Accessed 25 March 2011].

AMTI Force and Motion (2011). *ADL knee simulator specifications*. [Online] Available at: `http://www.amti.biz` [Accessed 30 June 2011].

Andrighetto, P., Valdiero, A. and Carlotto, L. (2006). Study of the friction behavior in industrial pneumatic actuators. In: *ABCM Symposium Series in Mechatronics*, vol. 2, pp. 369–376.

anon. (2006). Proportional-Wegeregelventil MPYE-5-...B. Tech. Rep., Festo.

Armstrong-Hélouvry, B., Dupont, P. and De Wit, C. (1994). A survey of models, analysis tools and compensation methods for the control of machines with friction. *Automatica*, vol. 30, no. 7, pp. 1083–1138.

Barnett, P., McEwen, H., Auger, D., Stone, M., Ingham, E. and Fisher, J. (2002). Investigation of wear of knee prostheses in a new displacement/force-controlled simulator. *Proceedings of the Institution of Mechanical Engineers, Part H: Journal of Engineering in Medicine*, vol. 216, no. 1, pp. 51–61.

Beater, P. (2007). *Pneumatic drives: system design, modelling and control*. Springer Verlag.

Belforte, G., Mattiazzo, G., Mauro, S. and Tokashiki, L. (2003). Measurement of friction force in pneumatic cylinders. *Tribotest*, vol. 10, no. 1, pp. 33–48.

Bert, J. (2005). Unicompartmental knee replacement. *Orthopedic Clinics of North America*, vol. 36, no. 4, pp. 513–522.

Bishop, R. (2002). *The mechatronics handbook*. CRC Press.

Blunn, G., Walker, P., Joshi, A. and Hardinge, K. (1991). The dominance of cyclic sliding in producing wear in total knee replacements. *Clinical orthopaedics and related research*, vol. 273, pp. 253–60.

Bourne, R., Masonis, J. and Anthony, M. (2003). An analysis of rotating-platform total knee replacements. *Clinical orthopaedics and related research*, vol. 410, pp. 173–180.

Brown, S. and Clarke, I. (2006). A review of lubrication conditions for wear simulation in artificial hip replacements. *Tribology transactions*, vol. 49, no. 1, pp. 72–78.

Bubert, E. (2009). *Highly extensible skin for a variable wing-span morphing aircraft utilizing pneumatic artificial muscle actuation*. Ph.D. thesis, University of Maryland.

Burgess, I., Kolar, M., Cunningham, J. and Unsworth, A. (1997). Development of a six station knee wear simulator and preliminary wear results. *Proceedings of the Institution of Mechanical Engineers, Part H: Journal of Engineering in Medicine*, vol. 211, no. 1, pp. 37–47.

Callaghan, J. (2003). *The adult knee*, vol. 1. Lippincott Williams & Wilkins.

Callahan, C., Drake, B., Heck, D. and Dittus, R. (1995). Patient outcomes following unicompartmental or bicompartmental knee arthroplasty. *The Journal of arthroplasty*, vol. 10, no. 2, pp. 141–150.

Carneiro, J. and de Almeida, F. (2006*a*). Modeling pneumatic servovalves using neural networks. In: *Computer Aided Control System Design, 2006 IEEE International Conference on Control Applications, 2006 IEEE International Symposium on Intelligent Control, 2006 IEEE*, pp. 790–795. IEEE.

Carneiro, J. and de Almeida, F. (2006*b*). Reduced-order thermodynamic models for servo-pneumatic actuator chambers. *Proceedings of the Institution of Mechanical Engineers, Part I: Journal of Systems and Control Engineering*, vol. 220, no. 4, p. 301.

DesJardins, J., Banks, S., Benson, L., Pace, T. and LaBerge, M. (2007). A direct comparison of patient and force-controlled simulator total knee replacement kinematics. *Journal of biomechanics*, vol. 40, no. 15, pp. 3458–3466.

DesJardins, J., Walker, P., Haider, H. and Perry, J. (2000). The use of a force-controlled dynamic knee simulator to quantify the mechanical performance of total knee replacement designs during functional activity. *Journal of Biomechanics*, vol. 33, no. 10, pp. 1231–1242.

Dienst, M., Greis, P., Ellis, B., Bachus, K. and Burks, R. (2007). Effect of lateral meniscal allograft sizing on contact mechanics of the lateral tibial plateau. *The American journal of sports medicine*, vol. 35, no. 1, pp. 34–42.

Elias, J., Kumagai, M., Mitchell, I., Mizuno, Y., Mattessich, S., Webb, J. and Chao, E. (2002). In vitro kinematic patterns are similar for a fixed platform and a mobile bearing prosthesis. *The Journal of Arthroplasty*, vol. 17, no. 4, pp. 467–474.

Emerton, M. and Burton, D. (2001). The role of unicompartmental knee replacement. *Current Orthopaedics*, vol. 15, no. 6, pp. 406–412.

Freeman, M.A.R. (2001 December). How the knee moves. *Current Orthopaedics*, vol. 15, no. 6, pp. 444–450.

Freeman, M.A.R. and Pinskerova, V. (2005 February). The movement of the normal tibio-femoral joint. *Journal of Biomechanics*, vol. 38, no. 2, pp. 197–208.

Fukubayashi, T., Torzilli, P., Sherman, M. and Warren, R. (1982). An in vitro biomechanical evaluation of anterior-posterior motion of the knee. tibial displacement, rotation, and torque. *The Journal of bone and joint surgery. American volume*, vol. 64, no. 2, pp. 258–264.

Grood, E. and Suntay, W. (1983). A joint coordinate system for the clinical description of three-dimensional motions: application to the knee. *Journal of Biomechanical Engineering*, vol. 105, pp. 136–144.

Guang-zheng, P. and Wei, F. (2005). A new measurement method of the flow-rate characteristics of the regulator. *Proceedings of the 6th JFPS International*, vol. 3, pp. 766–770.

Haider, H. and Walker, P. (2005). Measurements of constraint of total knee replacement. *Journal of biomechanics*, vol. 38, no. 2, pp. 341–348.

Haider, H., Walker, P., DesJardins, J. and Blunn, G. (2006). Effects of patient and surgical alignment variables on kinematics in tkr simulation under force-control. *Journal of ASTM International*, vol. 3, no. 10, pp. 3–16.

Harman, M., Affatato, S., Spinelli, M., Zavalloni, M., Stea, S. and Toni, A. (2010). Polyethylene insert damage in unicondylar knee replacement: a comparison of in vivo function and in vitro simulation. *Proceedings of the Institution of Mechanical Engineers, Part H: Journal of Engineering in Medicine*, vol. 224, no. 7, pp. 823–830.

Harris, P., O'Donnel, G. and Whelan, T. (2011). Modelling and identification of industrial pneumatic drive system. *The International Journal of Advanced Manufacturing Technology*, pp. 1–12. ISSN 0268-3768.

Houtem, M., Clough, R., Khan, A., Harrison, M. and Blunn, G. (2006). Validation of the soft tissue restraints in a force-controlled knee simulator. *Proceedings of the Institution of Mechanical Engineers, Part H: Journal of Engineering in Medicine*, vol. 220, no. 3, pp. 449–456.

Hsu, H., Garg, A., Walker, P., Spector, M. and Ewald, F. (1989). Effect of knee component alignment on tibial load distribution with clinical correlation. *Clinical Orthopaedics and Related Research*, vol. 248, pp. 135–144.

International Organization for Standardization (1989). *Pneumatic fluid power - Components using compressible fluids - Determination of flow-rate characteristics*, ISO 6358:1989(E), International Organization for Standardization, Geneva.

International Organization for Standardization (2000). *Implants for surgery - Wear of total knee-joint prostheses - Methods of measurement*, ISO 14243-2:2000(E), International Organization for Standardization, Geneva.

International Organization for Standardization (2002). *Implants for surgery - Wear of total knee-joint prostheses - Loading and displacement parameters for wear-testing machines with load control and corresponding environmental conditions for test*, ISO 14243-1:2002(E), International Organization for Standardization, Geneva.

International Organization for Standardization (2004). *Implants for surgery - Wear of total knee-joint prostheses - Loading and displacement parameters for wear-testing machines with displacement control and corresponding environmental conditions for test*, ISO 14243-3:2004(E), International Organization for Standardization, Geneva.

International Organization for Standardization (2009). *Implants for surgery - Wear of total knee-joint prostheses - Loading and displacement parameters for wear-testing machines with load control and corresponding environmental conditions for test*, ISO 14243-1:2002(E), International Organization for Standardization, Geneva.

Jackson, M., Sarangi, P. and Newman, J. (1994). Revision total knee arthroplasty: Comparison of outcome following primary proximal tibial osteotomy or unicompartmental arthroplasty. *The Journal of Arthroplasty*, vol. 9, no. 5, pp. 539–542.

Janocha, H. (2004). *Actuators: basics and applications*. Springer Verlag.

Krames, C. (2001). *Knee anatomy - patella reflected to show knee anatomy.* [Image Online] Available at: `http://www.kramestudios.com` [Accessed 24 January 2011].

Kretzer, J., Jakubowitz, E., Sonntag, R., Hofmann, K., Heisel, C. and Thomsen, M. (2010). Effect of joint laxity on polyethylene wear in total knee replacement. *Journal of biomechanics*, vol. 43, no. 6, pp. 1092–1096.

Lampaert, V., Al-Bender, F. and Swevers, J. (2003). A generalized maxwell-slip friction model appropriate for control purposes. In: *Physics and Control, 2003. Proceedings. 2003 International Conference*, vol. 4, pp. 1170–1177. IEEE.

Liao, Y., Benya, P. and McKellop, H. (1999). Effect of protein lubrication on the wear properties of materials for prosthetic joints. *Journal of biomedical materials research*, vol. 48, no. 4, pp. 465–473.

Lund University Hospital, Department of Orthopedics (2010). *The Swedish Knee Arthroplasty Register, Annual Report*. Lund: Wallin & Dalholm AB.

Mahoney, O., Noble, P., Rhoads, D., Alexander, J. and Tullos, H. (1994). Posterior cruciate function following total knee arthroplasty: A biomechanical study. *The Journal of Arthroplasty*, vol. 9, no. 6, pp. 569–578.

Maletsky, L. and Hillberry, B. (2005). Simulating dynamic activities using a five-axis knee simulator. *Journal of Biomechanical Engineering*, vol. 127, pp. 123–133.

Mancuso, C., Ranawat, C., Esdaile, J., Johanson, N. and Charlson, M. (1996). Indications for total hip and total knee arthroplasties: Results of orthopaedic surveys. *The Journal of arthroplasty*, vol. 11, no. 1, pp. 34–46.

Markolf, K., Bargar, W., Shoemaker, S. and Amstutz, H. (1981). The role of joint load in knee stability. *The Journal of bone and joint surgery. American volume*, vol. 63, no. 4, pp. 570–585.

Martelli, S. and Pinskerova, V. (2002 May). The shapes of the tibial and femoral articular surfaces in relation to tibiofemoral movement. *The Journal of Bone and Joint Surgery. British volume*, vol. 84, no. 4, pp. 607–613.

McEwen, H., Barnett, P., Bell, C., Farrar, R., Auger, D., Stone, M. and Fisher, J. (2005). The influence of design, materials and kinematics on the in vitro wear of total knee replacements. *Journal of biomechanics*, vol. 38, no. 2, pp. 357–365.

Mizuno, Y., Kumagai, M., Mattessich, S., Elias, J., Ramrattan, N., Cosgarea, A. and Chao, E. (2001). Q-angle influences tibiofemoral and patellofemoral kinematics. *Journal of Orthopaedic Research*, vol. 19, no. 5, pp. 834–840.

Moran, M. (2005). *Computational and Experimental Assessment of Total Knee Replacement Motion*. Ph.D. thesis, The Pennsylvania State University.

Morrison, J. (1969). Function of the knee joint in various activities. *Biomedical engineering*, vol. 4, no. 12, pp. 573–580.

Morrison, J. (1970). The mechanics of the knee joint in relation to normal walking. *Journal of biomechanics*, vol. 3, no. 1, pp. 51–61.

Moseley, J., O'Malley, K., Petersen, N., Menke, T., Brody, B., Kuykendall, D., Hollingsworth, J., Ashton, C. and Wray, N. (2002). A controlled trial of arthroscopic surgery for osteoarthritis of the knee. *New England Journal of Medicine*, vol. 347, no. 2, pp. 81–88.

MTS Systems (2002). *Bionix Solutions for Biomaterials and Biomechanics Testing*. [Online] Available at: `http://www.mts.com` [Accessed 03 February 2009].

MTS Systems (2008). *Bionix Knee Wear Simulator*. [Online] Available at: `http://www.mts.com` [Accessed 29 September 2009].

Najafi, F., Fathi, M. and Saadat, M. (2009). Dynamic modelling of servo pneumatic actuators with cushioning. *The International Journal of Advanced Manufacturing Technology*, vol. 42, no. 7, pp. 757–765.

Nakagawa, S., Kadoya, Y., Todo, S., Kobayashi, A., Sakamoto, H., Freeman, M.A. and Yamano, Y. (2000 November). Tibiofemoral movement 3: Full flexion in the living knee studied by mri. *The Journal of Bone and Joint Surgery. British Volume*, vol. 82, no. 8, pp. 1199–1200.

Newman, J., Ackroyd, C. and Shah, N. (1998). Unicompartmental or total knee replacement? five-year results of a prospective, randomised trial of 102 osteoarthritic knees with unicompartmental arthritis. *The Journal of bone and joint surgery. British volume*, vol. 80, no. 5, pp. 862–865.

Ngai, V. and Wimmer, M. (2009). Kinematic evaluation of cruciate-retaining total knee replacement patients during level walking: A comparison with the displacement-controlled iso standard. *Journal of biomechanics*, vol. 42, no. 14, pp. 2363–2368.

Ning, S. and Bone, G. (2005). Development of a nonlinear dynamic model for a servo pneumatic positioning system. In: *Mechatronics and Automation, 2005 IEEE International Conference*, vol. 1, pp. 43–48. IEEE.

Nouri, B. (2004). Friction identification in mechatronic systems. *ISA transactions*, vol. 43, no. 2, pp. 205–216.

Nouri, B., Al-Bender, F., Swevers, J., Vanherek, P. and Van Brussel, H. (2000). Modelling a pneumatic servo positioning system with friction. In: *Proceedings of the American Control Conference, 2000*, vol. 2, pp. 1067–1071. IEEE.

Palastanga, N., Field, D. and Soames, R. (2002). *Anatomy and Human Movement*. 4th edn. Butterworth-Heinemann.

Pavlovic, J., Kirstukas, S., Touchi, H. and Bechtold, J. (1994). Dynamic simulation machine for measurement of knee mechanics and intra-articular pressures. *ASME Bioengineering Division Publication BED*, vol. 28, pp. 277–278.

Price, A., Webb, J., Topf, H., Dodd, C., Goodfellow, J., Murray, D. *et al.* (2001). Rapid recovery after oxford unicompartmental arthroplasty through a short incision. *The Journal of arthroplasty*, vol. 16, no. 8, pp. 970–976.

Pugi, L., Malvezzi, M., Allotta, B., Banchi, L. and Presciani, P. (2004). A parametric library for the simulation of a union internationale des chemins de fer (uic) pneumatic braking system. *Proceedings of the Institution of Mechanical Engineers, Part F: Journal of Rail and Rapid Transit*, vol. 218, no. 2, pp. 117–132.

Richer, E. and Hurmuzlu, Y. (2000). A high performance pneumatic force actuator system: Part I - Nonlinear mathematical model. *Journal of dynamic systems, measurement, and control*, vol. 122, pp. 416–425.

Saikko, V. (2003). Effect of lubricant protein concentration on the wear of ultra-high molecular weight polyethylene sliding against a cocr counterface. *Journal of tribology*, vol. 125, pp. 638–642.

Saldanha, K., Keys, G., Svard, U., White, S. and Rao, C. (2007). Revision of oxford medial unicompartmental knee arthroplasty to total knee arthroplasty - results of a multicentre study. *The Knee*, vol. 14, no. 4, pp. 275–279.

Seedhom, B. and Wallbridge, N. (1985). Walking activities and wear of prostheses. *Annals of the Rheumatic Diseases*, vol. 44, no. 12, pp. 838–843.

Shakespeare, D. and Jeffcote, B. (2003). Unicondylar arthroplasty of the knee - cheap at half the price? *The Knee*, vol. 10, no. 4, pp. 357–361.

Smith, J.W. (1954). Observations on the postural mechanism of the human knee joint. *Journal of Anatomy*, vol. 90, pp. 236–261.

Soudry, M., Walker, P., Reilly, D., Kurosawa, H. and Sledge, C. (1986). Effects of total knee replacement design on femoral-tibial contact conditions. *The Journal of Arthroplasty*, vol. 1, no. 1, pp. 35–45.

Spinelli, M., Affatato, S., Harman, M. and DesJardins, J. (2010). Bi-unicondylar knee prosthesis functional assessment utilizing force-control wear testing. *Proceedings of the Institution of Mechanical Engineers, Part H: Journal of Engineering in Medicine*, vol. 224, no. 7, pp. 813–821.

St. Venant, A. and Wantzel, P. (1839). Mèmoire et expèriences sur l'ècoulement de l'air. *J. Ecole Polytech.(Paris)*, vol. 16, pp. 85–122.

Strickland, A. (2009). *Enhanced Pre-Clinical Assessment of Total Knee Replacement Using Computational Modelling with Experimental Corroboration & Probabilistic Applications*. Ph.D. thesis, University of Southampton.

Sutton, L., Werner, F., Haider, H., Hamblin, T. and Clabeaux, J. (2010). In vitro response of the natural cadaver knee to the loading profiles specified in a standard for knee implant wear testing. *Journal of biomechanics*, vol. 43, no. 11, pp. 2203–2207.

The NJR Centre, Hemel Hempstead (2010). *The National Joint Registry for England and Whales Annual report*. [Online] Available at: `http://www.njrcentre.org.uk` [Accessed 22 November 2011].

Tjahjowidodo, T., Al-Bender, F., Van Brussel, H. and Symens, W. (2007). Friction characterization and compensation in electro-mechanical systems. *Journal of sound and vibration*, vol. 308, no. 3-5, pp. 632–646.

Van der Merwe, J. (2009). *Development of a knee replacement wear simulator with displacement control*. Final Year Project, Stellenbosch University.

Walker, P., Blunn, G., Broome, D., Perry, J., Watkins, A., Sathasivam, S., Dewar, M. and Paul, J. (1997). A knee simulating machine for performance evaluation of total knee replacements. *Journal of Biomechanics*, vol. 30, pp. 83–89.

Walker, P., Blunn, G., Perry, J., Bell, C., Sathasivam, S., Andriacchi, T., Paul, J., Haider, H. and Campbell, P. (2000). Methodology for long-term wear testing of total knee replacements. *Clinical orthopaedics and related research*, vol. 372, pp. 290–301.

Wasielewski, R., Galante, J., Leighty, R., Natarajan, R. and Rosenberg, A. (1994). Wear patterns on retrieved polyethylene tibial inserts and their relationship to technical considerations during total knee arthroplasty. *Clinical orthopaedics and related research*, vol. 299, pp. 31–43.

Weale, A., Halabi, O., Jones, P. and White, S. (2001). Perceptions of outcomes after unicompartmental and total knee replacements. *Clinical Orthopaedics and Related Research*, vol. 382, p. 143.

Weale, A. and Newman, J. (1994). Unicompartmental arthroplasty and high tibial osteotomy for osteoarthrosis of the knee: A comparative study with a 12-to 17-year follow-up period. *Clinical Orthopaedics and Related Research*, vol. 302, pp. 134–137.

White, B., D'Lima, D., Drueding, A., Cox, J., Carignan, F. and Dean, S. (2006). A simulator study of tkr kinematics using modeled soft-tissue constraint: virtual soft-tissue control for knee simulation. *Journal of ASTM International*, vol. 3, no. 8, pp. 33–44.

Zavatsky, A. (1997). A kinematic-freedom analysis of a flexed-knee-stance testing rig. *Journal of biomechanics*, vol. 30, no. 3, pp. 277–280.

Zhu, Y. (2006). *Control of pneumatic systems for free space and interaction tasks with system and environmental uncertainties*. Ph.D. thesis, Vanderbilt University.

Zimmer, Inc (). *Knee Solutions*. [Online] Available at: `http://www.zimmer.com` [Accessed 11 October 2011].

Appendices

Appendix A

Movement of the Knee

A.1 Anatomic Reference Frames

Table A.1 lists the definitions of the anatomic reference terms as used throughout this thesis. Illustrated in Figure A.1 are the orthogonal reference planes of the human body, followed by Figure A.2 which depicts the movement of features relating to the knee. Note that these definitions are relative, and therefore do not describe absolute, measurable position or motion.

Table A.1: Anatomic Reference Terms

	Term	Definition
Planes	Coronal	Vertical plane dividing the body into front and back
	Sagittal	Vertical plane dividing the body into left and right
	Transverse	Horizontal plane dividing the body into upper and lower
Translations	Anterior	Forwards
	Posterior	Backwards
	Medial	Toward the middle or inside
	Lateral	Toward the outside, left or right
	Superior	Above
	Inferior	Below
	Proximal	Towards the beginning or torso
	Distal	Further from the beginning or torso
Rotations	Abduction	Motion away from mid-line of body
	Adduction	Motion towards mid-line of body
	Flexion	Motion decreasing joint angle
	Extension	Motion increasing joint angle
	Internal	Inward rotation
	External	Outward rotation
	Varus	Inward turning of bone (bow-legged)
	Valgus	Outward turning of bone (knock-kneed)

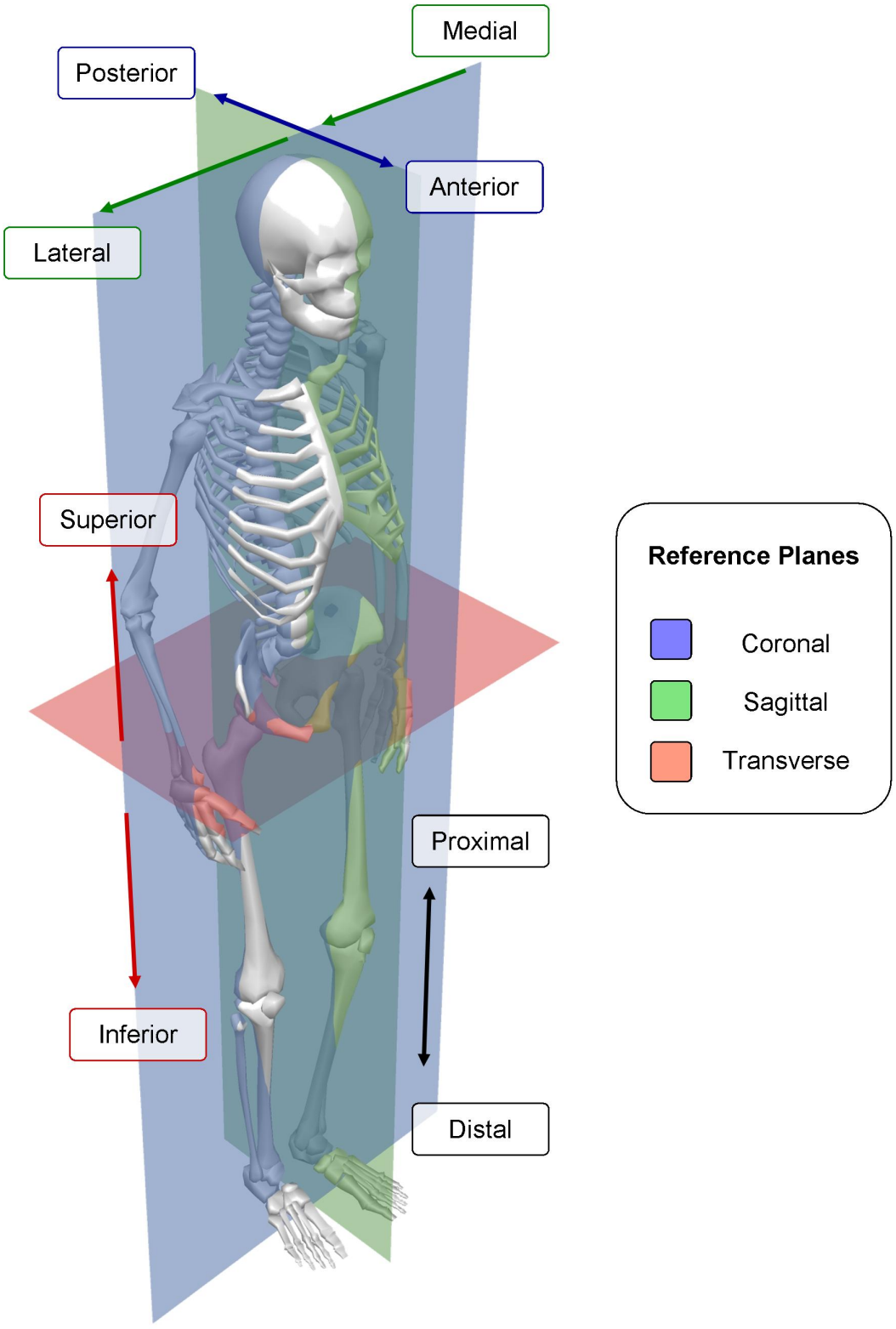

Figure A.1: Reference Planes of the Human Body (Illustration: J. v.d. Merwe)

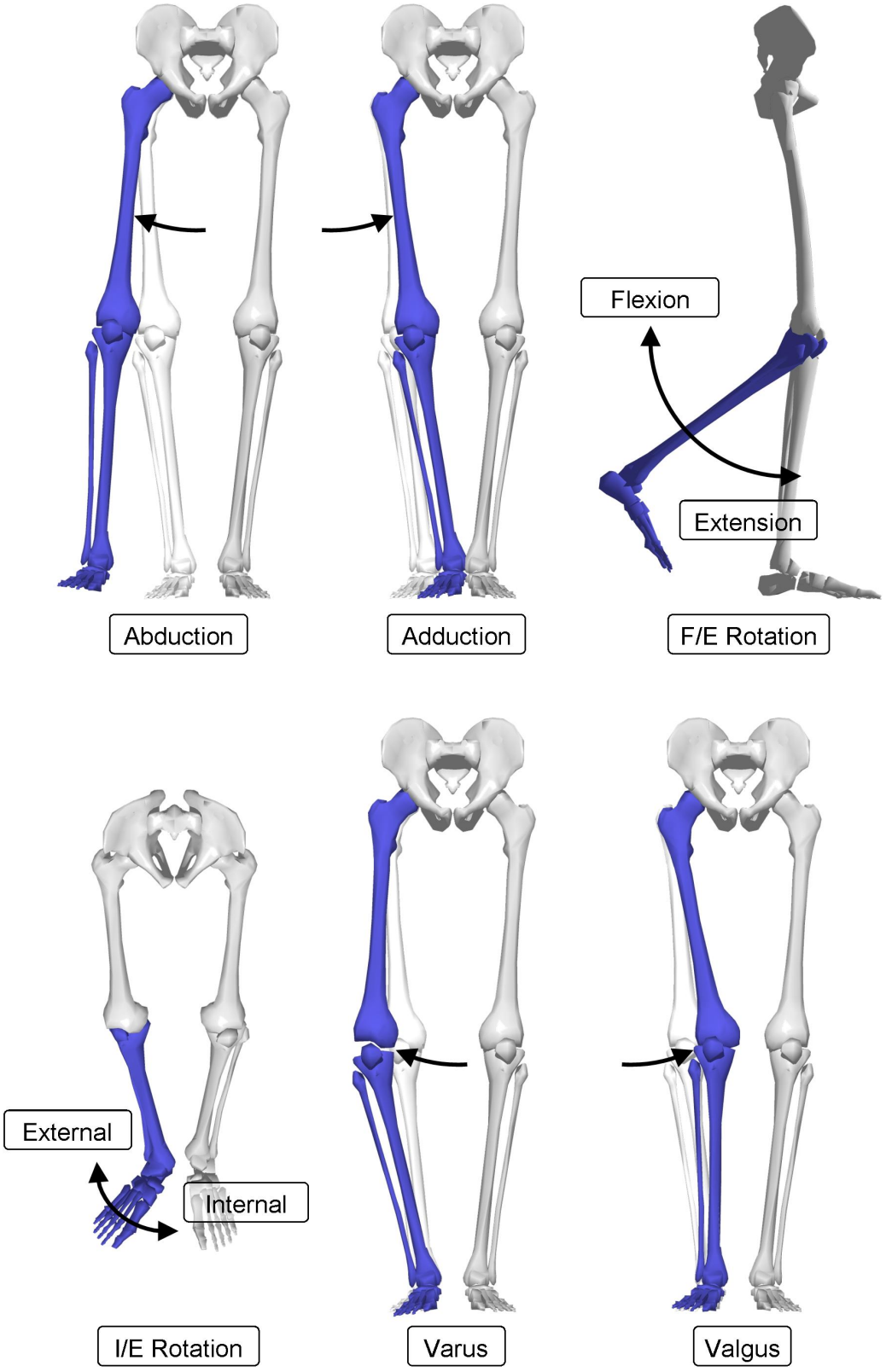

Figure A.2: Relative Movement of the Knee (Illustration: J. v.d. Merwe)

A.2 Physiological Movement

The flexion/extension (F/E) arc of the knee may be divided into three sections, each having a different mode of articulation. They are the active functional, passive, and terminal extension arcs, each shown in Figure A.3. The following discussion attempts to describe the movement of the tibio-femoral joint during articulation within each of the aforementioned arcs in terms of relative physiological orientation.

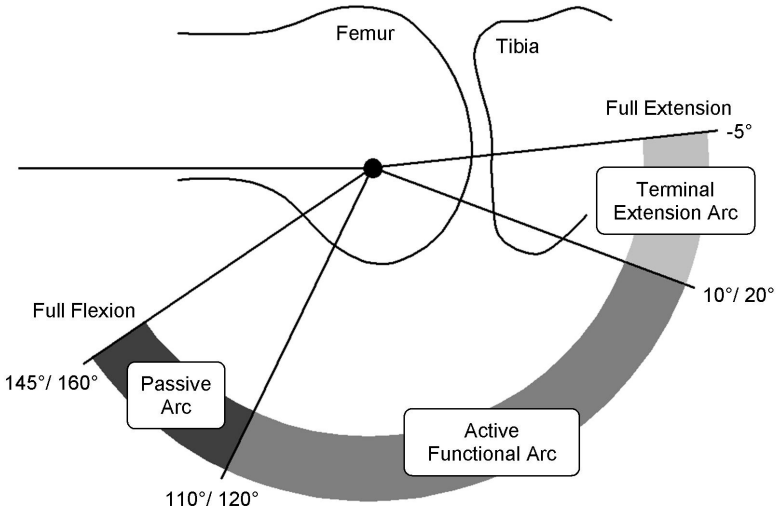

Figure A.3: Knee F/E Arc, Sagittal View (Adapted from Freeman (2001))

The active functional arc has a range that typically extends between 10°/20° and 110°/120°, is entirely under active muscle control, and is most used during everyday activities (Freeman, 2001). Throughout this arc the femoral condyles' surfaces that are in contact with the tibia are circular when viewed in the sagittal plane, with an average radius of 22 mm, with the medial femoral condyle's geometry approximating a spherical section (Martelli and Pinskerova, 2002). During flexion or extension within the active arc the medial femoral condyle typically does not translate anteroposteriorly more than ±1.5 mm, while the lateral femoral condyle may translate up to 15 mm (Freeman and Pinskerova, 2005). This relative stability of the medial femoral condyle, in combination with the large anterior/posterior (A/P) translation of the lateral femoral condyle, results in internal/external (I/E) rotation of the tibia (Freeman, 2001). Varus/valgus (V/V) rotation may also occur due to differences in the level of the medial and lateral contact surfaces between the femur and tibia (Freeman and Pinskerova, 2005).

Throughout the terminal extension arc, which extends between approximately -5°at hyperextension, and 10°/20°, the medial femoral condyle continues to remain relatively anteroposteriorly stable (Freeman, 2001). Contact

between said condyle and the tibia does, however, move from the posterior part of the condyle to its anterior section, which has a larger radius typically $\geq$ 30mm (Martelli and Pinskerova, 2002), via pure sliding motion (Freeman, 2001). The lateral femoral condyle, according to Freeman and Pinskerova (2005), in combination with the relative anteroposterial stability of the medial femoral condyle, rolls anteriorly as terminal extension is approached, causing continued internal rotation. The curvature of the lateral femoral condyle about which the F/E rotation occurs during movement within the terminal extension arc is, however, represented by such a small contact surface region that it is difficult to determine the radius and extent of this region. Finally, as the knee is rotated towards terminal extension, it gradually begins to resist the motion until eventually it locks (Smith, 1954). This is due to various factors, which include the stretching of anterior and lateral cruciate ligaments to their full (Freeman, 2001).

The passive arc is so named, according to Freeman (2001), due to the fact that, within the rotational range between 110°/120°to 145°/160°, the thigh muscles controlling the motion of the joint is unable to flex it further. Flexion throughout this arc occurs under the exertion of an externally applied load. Actions in which the knee is flexed along the passive arc include kneeling and squatting, and the extent thereof is limited by the posterior soft muscles. Nakagawa *et al.* (2000) showed that at extreme flexion angles the medial femoral condyle, although still lying over the tibia, moves away from it, while the lateral femoral condyle becomes posteriorly subluxed. Tibial rotation at passive flexion depends on the type of action performed, such as squatting, which causes little rotation, as opposed to kneeling with the buttocks resting on the feet, which causes greater rotation. Frequent kneeling in the manner previously described may also, over time, influence the magnitude of the tibial rotation and full passive flexion experienced during such an action.

Appendix B

In-vitro Knee Joint Evaluation Devices

Historically, there are two types of devices employed to evaluate knee implants *in-vitro*, namely quasi-static machines and dynamic machines (Maletsky and Hillberry, 2005). Quasi-static machines provide an objective means to evaluate implant characteristics at fixed flexion angles, while according to Moran (2005), by applying cyclic loads and motions to knee implants, dynamic machines attempt to recreate the kinetics and kinematics of the knee joint during activities of daily living (ADL). Dynamic machines may be further sub-classified as either machines that reproduce the entire lower limb's geometry, or machines that implement actuation of the joint only (Walker *et al.*, 1997). Refer to Figure B.1 for an illustration of knee evaluation device classification, as well as an indication of the measure quantifying implant performance to which each is most applied in literature.

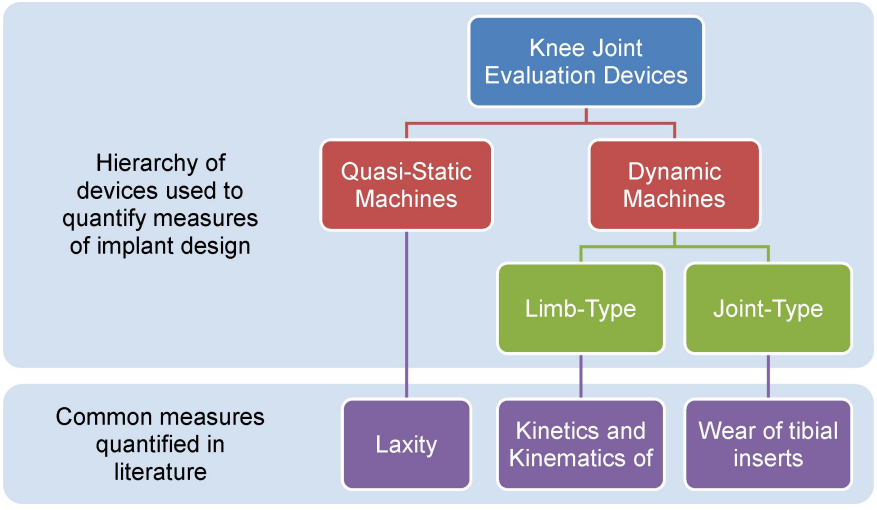

Figure B.1: Classification of Knee Joint Evaluation Devices (Illustration: J. v.d. Merwe)

B.1 Quasi-Static Machines

Quasi-static machines allow the control of selected degrees of freedom pertaining to the femoral and tibial components of an implant, which in turn are rigidly fixed to the test frame (Moran, 2005). The ability of these machines to simulate forces exerted by many of the muscles that cross the knee joint results in robust loading of the specimen (Maletsky and Hillberry, 2005).

Such quasi-static experiments, typically short term (Walker *et al.*, 1997), are sufficient for the evaluation of laxity (Haider and Walker, 2005) and the sensitivity to component placement (Hsu *et al.*, 1989), as well as the demonstration of contact point locations (Soudry *et al.*, 1986) of knee implants. The use of these machines, however, is not solely limited to the investigation of matters relating to knee arthroplasties, but may be expanded to include studies regarding other surgical procedures performed on the knee. Shown in Figure B.2 is a cadaveric knee mounted on a quasi-static test rig during one such study investigating the effects of allograft sizing (Dienst *et al.*, 2007).

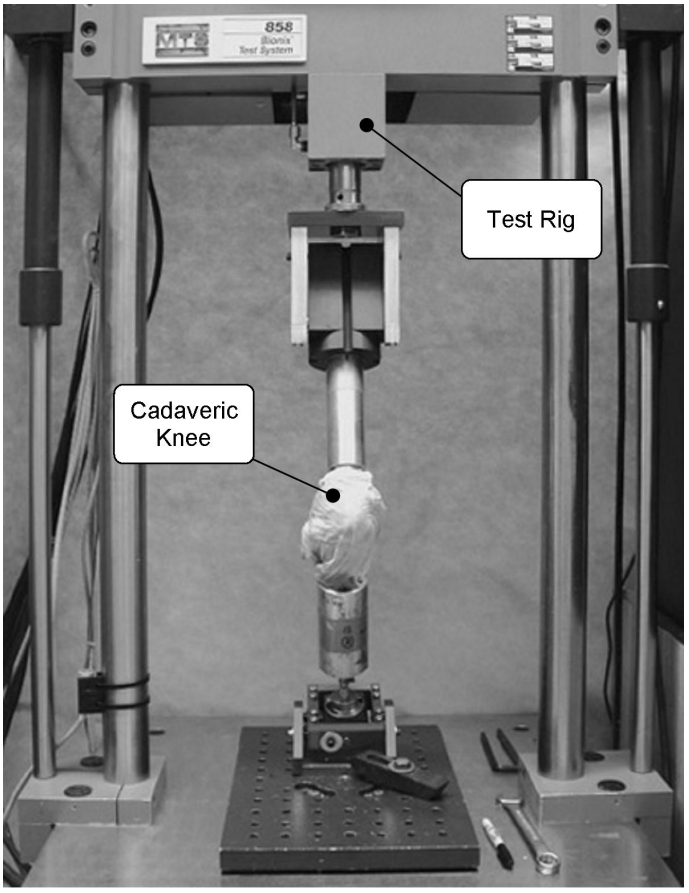

Figure B.2: Quasi-Static Test Rig (Dienst *et al.*, 2007)

B.2 Lower Limb-Type Simulators

Limb-type dynamic machines apply forces externally to 'hip' and 'ankle' joints in combination with a simulated quadriceps force in order to replicate physiological knee joint behaviour (Walker *et al.*, 1997). The EnduraTec Knee Simulation Machine (Pavlovic *et al.*, 1994), the Purdue/Kansas Knee Simulator (Maletsky and Hillberry, 2005) and the MTS Bionix Kinematics Knee Simulator (MTS Systems, 2002) are examples of these types of machines, all of them similar to the Oxford Knee-Testing Rig (Zavatsky, 1997) shown in Figure B.3, even though this machine was originally designed for quasi-static tests.

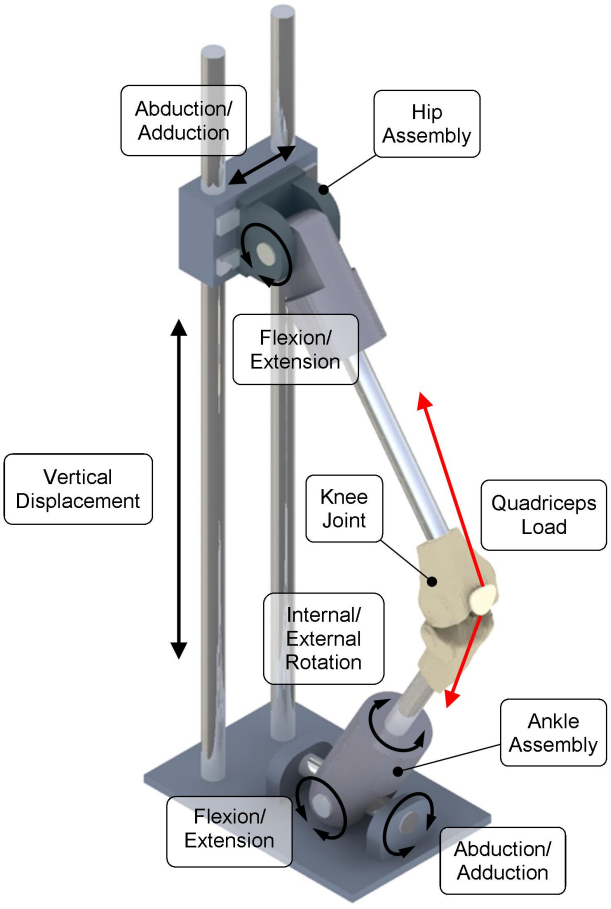

Figure B.3: Rendering of the Oxford Knee-Testing Rig (Zavatsky, 1997) with Quadriceps Load (Illustration: J. v.d. Merwe)

Activities of daily living such as squatting, kneeling, rising from a chair, stair climbing and normal gait are reproducible on cadaveric knees mounted in Limb-type machines both before and after surgical procedures for comparative assessment (Moran, 2005). Examples of where this type of dynamic machine

is utilised in literature include an evaluation of the strain in the posterior cruciate ligament following total knee arthroplasty (TKA) (Mahoney *et al.*, 1994), a comparison between the kinematic patterns of fixed and mobile bearing knee implants (Elias *et al.*, 2002), as well as an investigation of the effect that changing the orientation of the quadriceps load has on tibio-femoral and patello-femoral joint kinematics (Mizuno *et al.*, 2001).

Simulators that reproduce the the entire lower limb's geometry, the patello-femoral joint and the quadriceps load have certain inherent characteristics. They result in more physiological models compared to simulators that actuate the joint only (Moran, 2005), although the resulting added complexity adversely affects the risk of long term failure (Walker *et al.*, 1997). As per Strickland (2009), limb-type simulators can also be driven by input derived from easily measurable clinical data. For example, inputs based on ground-plate reaction forces and torques may be applied at the 'ankle' joint, while motion capture and inverse-dynamics may provide inputs for the quadriceps and 'hip' joint actuators. However, since the knee joint is not directly actuated, it may be difficult to induce specific kinetics and kinematics therein. Finally, based on a perusal of the literature, it seems that limb-type simulators lend themselves much more readily to the investigation of cadaveric specimens than joint simulators, although this is not the rule, as demonstrated by Houtem *et al.* (2006) and Sutton *et al.* (2010).

B.3 Joint-Type Simulators

Joint-type simulators attempt to replicate *in-vivo* articulation of the knee by applying aggregate loads and motions to the joint itself (Strickland, 2009), without simulating the individual actions of the relevant muscle groups (Walker *et al.*, 1997). Commercially available examples of these machines include the Leeds/ProSim Knee Simulator (Simulation Solutions, Stockport, Manchester, UK), the Shore Western Knee Simulator (Shore Western Manufacturing, Monrovia, CA, USA), the dual and four station variants of the Instron Stanmore Knee Simulator (Instron, High Wycombe, Buckinghamshire, UK), the single station MTS Bionix Knee Wear Subsystem for use in conjunction with the Bionix load frame, as well as the six station MTS Bionix Knee Wear Simulator (MTS Systems Corporation, Eden Prairie, MN, USA), and the AMTI Boston Knee Simulator (Advanced Mechanical Technology, Watertown, MA, USA) shown in Figure B.4. The similarities in the design of these machines may be ascribed to the fact that most of them conform to the ISO 14243 Standards (2000; 2002; 2004), developed upon the Instron Stanmore Knee Simulator.

The purpose of standardised pre-clinical tests using joint-type simulators is to isolate the effect of implant design on wear from secondary variables such as patient anatomy, surgical technique and specimen-specific attributes, as well as to facilitate the comparison of implant mechanics (DesJardins *et al.*,

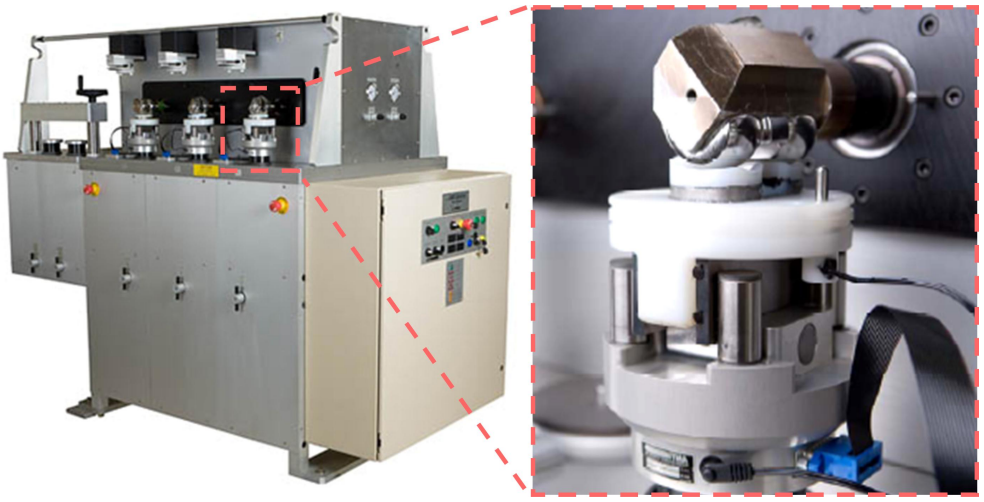

**Figure B.4: Six Station AMTI ADL Knee Simulator (Left)
Single Station with Mounted Specimen (Right)
(Photo: AMTI Force and Motion (2011))**

2000). By employing this methodology, numerous studies on total knee replacements (TKR's), and unicompartmental knee replacements (UKR's) to a lesser degree (Spinelli *et al.*, 2010), have been performed. Aspects relating to implant wear investigated in the literature include the wear rate of an ultra-high-molecular-weight-polyethylene (UHMWPE) tibial insert (Affatato *et al.*, 2008), a comparison of wear between three different implant designs (Bourne *et al.*, 2003), and the effect of joint laxity on implant wear (Kretzer *et al.*, 2010).

While the application of aggregate loads and motions to the joint has the dual advantage of providing greater control over the input variables and decreasing simulator complexity, as compared to the limb-type machine ethos, this methodology results in a model less representative of actual anatomy (Moran, 2005). For instance, one of the most notable features resulting from the joint-only approach is the absence of the patello-femoral joint and the effect it may have on the overall loading of the implant. Additionally, the identification of the standard loads and motions used to represent normal gait during level walking in joint-type simulators involved simplifying assumptions (Walker *et al.*, 1997), potentially further removing such a model from reality. Despite these shortcomings, a perusal of the literature indicates that the benefits associated with these simulators have motivated their extensive use.

Appendix C

Calibration Knee

In order to aid the eventual evaluation of the behaviour of the joint-type simulator as a whole, as well as controller development and fine-tuning, a 'calibration knee' has been designed, as shown in Figure C.1. Its purpose is to allow execution of one or more directions of actuation at a time, while directions of actuation that are not being investigated remain fixed. This should facilitate controller development by negating to an extent both 'cross-talk' between the profiles being actuated, as well as the inherent laxity of an unconstrained knee implant.

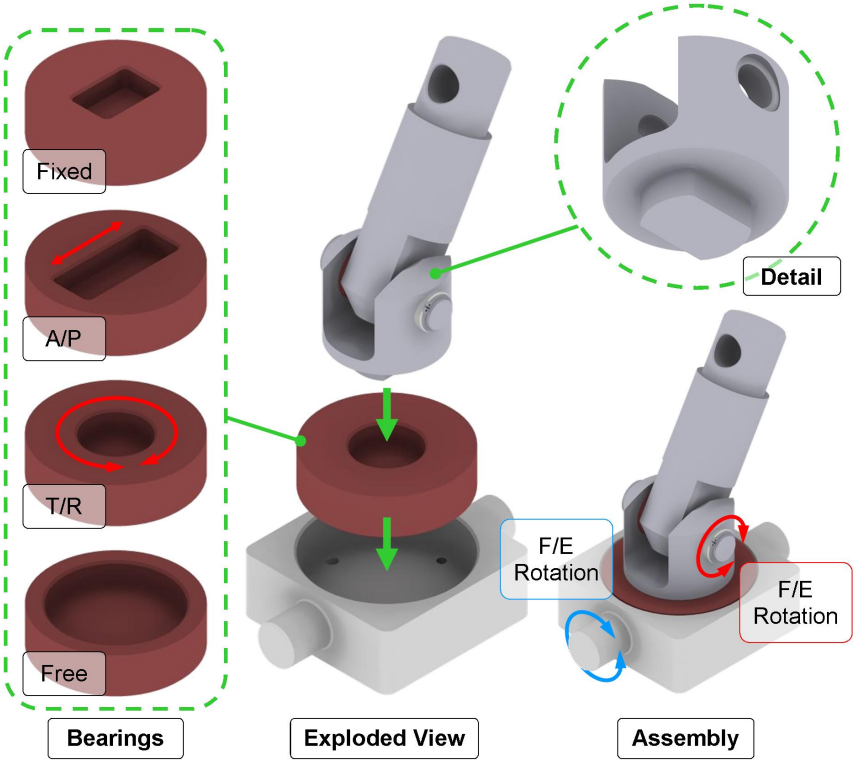

Figure C.1: Calibration Knee Design (Illustration: J. v.d. Merwe)

Various interchangeable bearings have been designed in order to fix different directions of actuation. The 'fixed' bearing is intended to restrict all movement except for either F/E rotation or axial force, or a combination thereof. The A/P and I/E bearings would additionally allow actuation in either of their namesake directions, while restricting the other. Finally, the 'free' bearing is designed to allow unrestricted actuation in all directions, most closely approximating testing of an actual implant. All components are manufactured from stainless steel, except for the aforementioned bearings, which is made from Vesconite, an internally lubricated, low friction polymer. Note should be taken that the calibration knee is not intended for long term testing, and is yet to be implemented as simulator development has not progressed to that extent at the time of this writing. The manufactured device is shown in Figure C.2.

Figure C.2: Calibration Knee (Photo: J. v.d. Merwe)

Appendix D

LabView VI

Illustrated here is the National Instruments LabView 2009 program, or VI, used during the experiments detailed in Chapters 3.5 and 4. Figures D.1 and D.2 shows the consumer and producer loops, respectively, while the alternative cases of the various if-statements are shown in D.3. Lastly,the graphical user interface is depicted in Figure D.4.

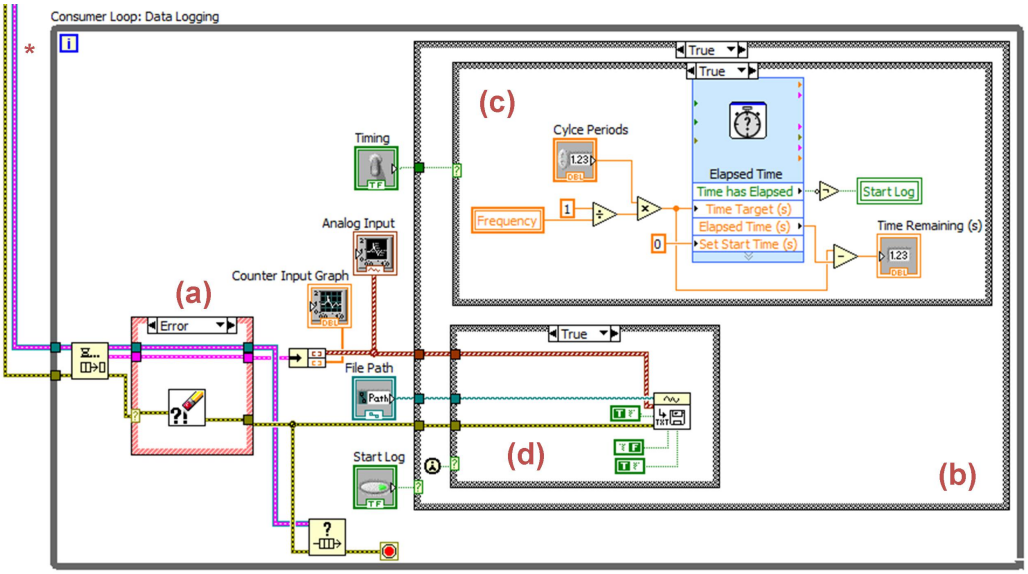

Figure D.1: Consumer Loop Block Diagram (Figure: J. v.d. Merwe)

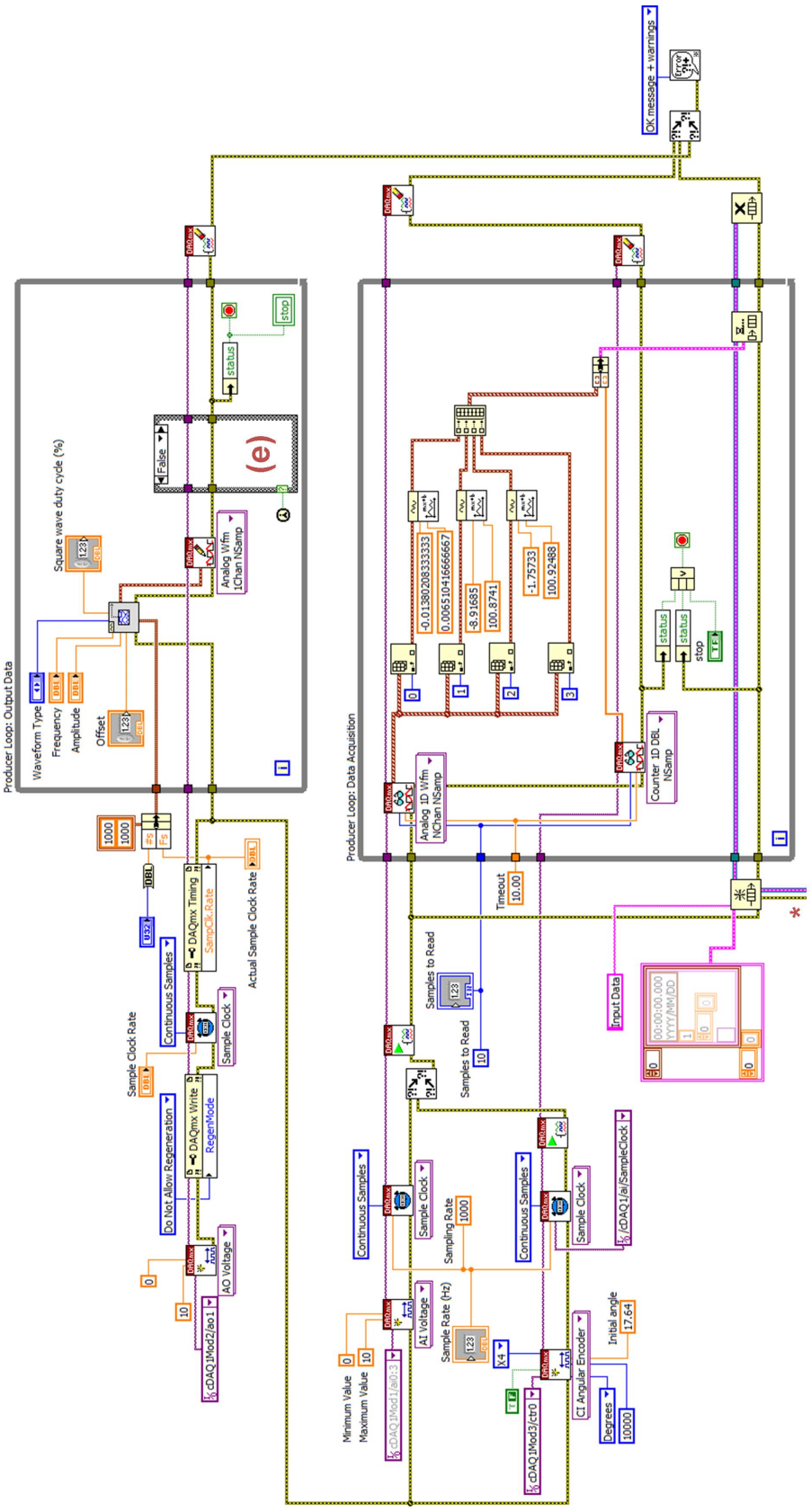

Figure D.2: Producer Loops Block Diagram (Figure: J. v.d. Merwe)

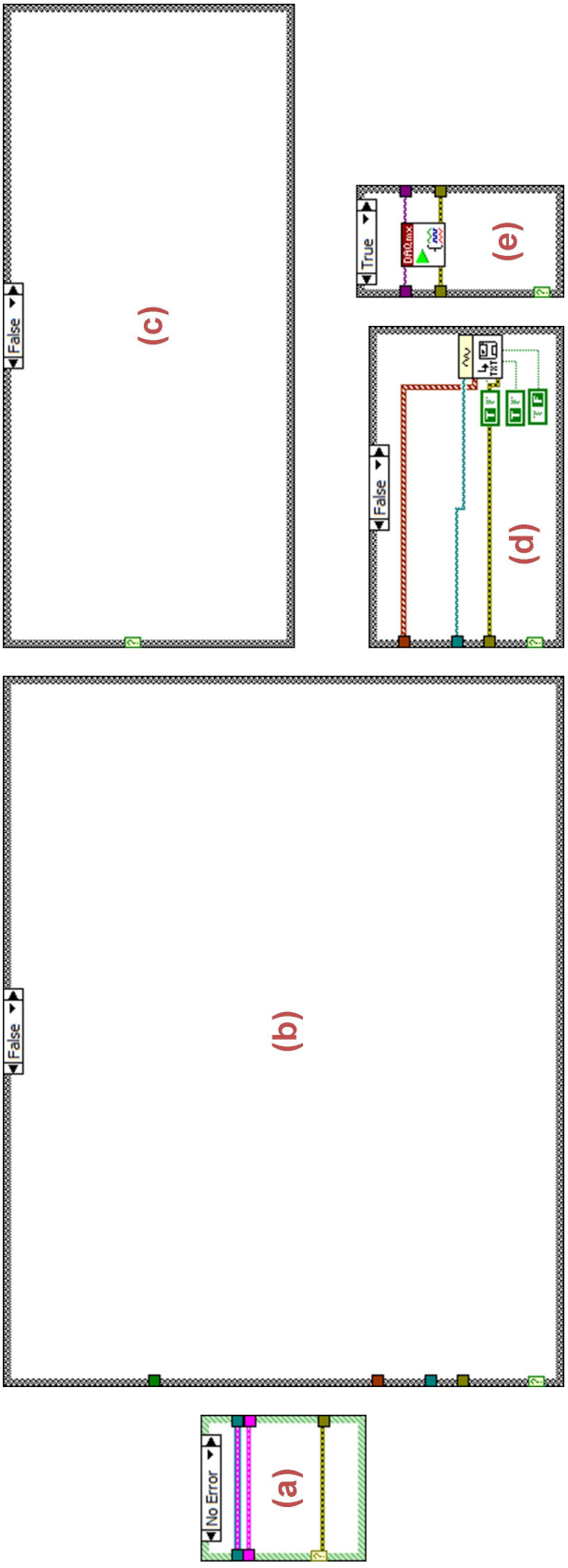

Figure D.3: Alternative Cases (Figure: J. v.d. Merwe)

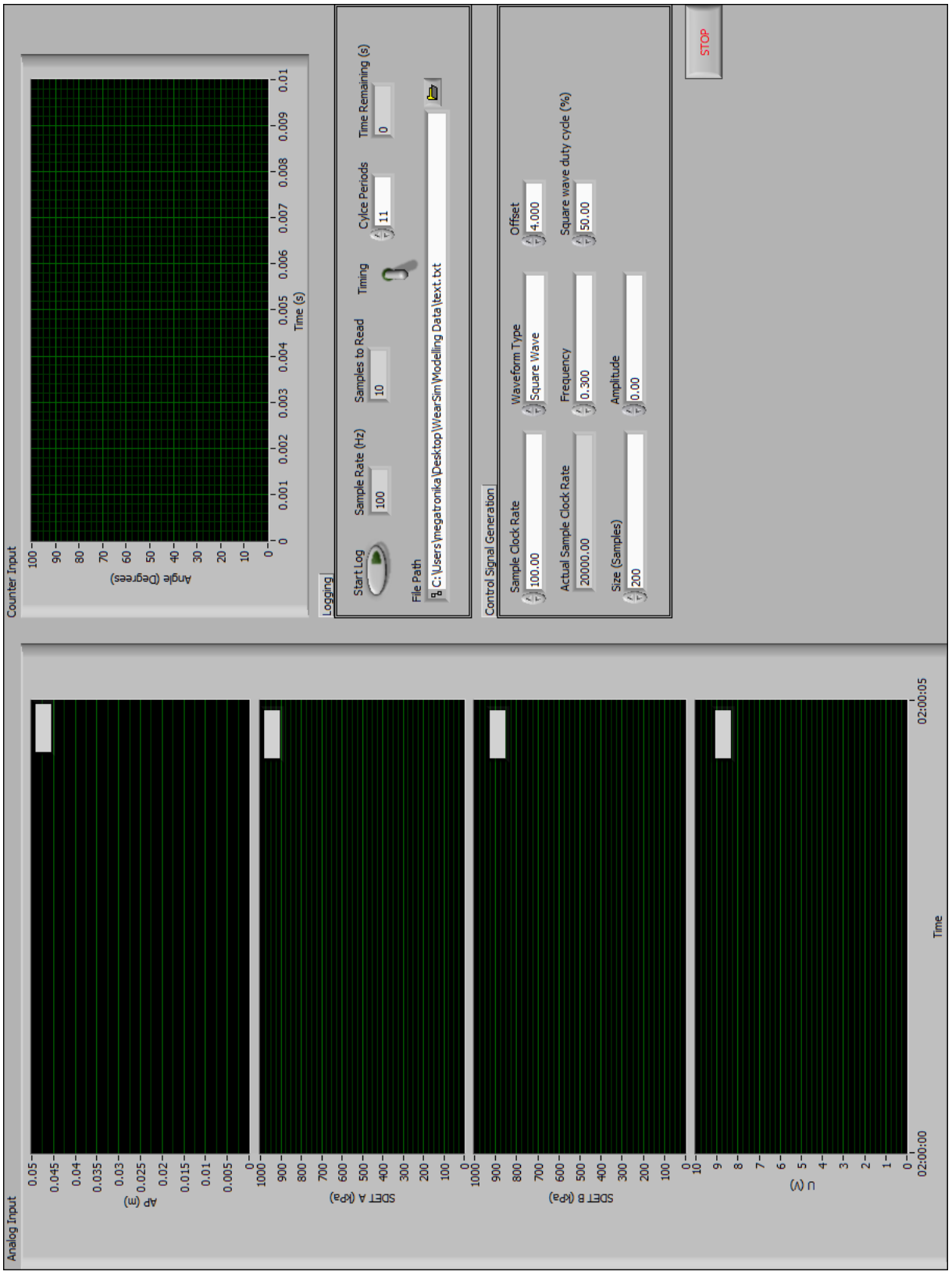

Figure D.4: VI Graphical User Interface (Figure: J. v.d. Merwe)

Appendix E

Supply Pressure Variations

During testing it was noticed that there is considerable variation in supply pressure due to the working of the proportional valves. This could potentially increase the difficulty of identifying unknown parameters, as well as having a negative effect on the eventual functioning of the overall system, not to mention interfering with the objective of evaluating a servo-pneumatic circuit's ability to effect the required actuation. Methods to negate the variations in the supply pressure were therefore investigated.

An experimental setup wherein a control valve was connected in series to the supply via a 10 l pressure vessel, and a 0.4 l pressure vessel connected downstream, was used to investigate the effects of supply pressure variation as shown in Figure E.1. Pressure was measured both at the supply as well as within the smaller pressure vessel. One channel of a 5/3 way proportional flow control valve was used to alternatively charge and discharge the 0.4 l vessel, with the valve's unused channel blocked to prevent leakage. Although a proportional valve was used, the control signal was such that the valve was either fully opened or fully closed with respect to the unblocked channel in order to maximise the effects of supply pressure variation. The valve and sensors used were Festo's MPYE proporional flow control valve and SDET pressure transducers as per Tables 3.1 and 3.5 (Chapter 3) respectively.

Configurations in which the 10 l pressure vessel was either connected or disconnected, and connection tubing with internal diameters of both seven and eight millimetres, were investigated. The resultant pressure plots are depicted in Figure E.2.

From the data it is clear that the drop in supply pressure is most severe for the case where the large pressure vessel is disconnected, and tubing with an internal diameter of seven millimetres is used. Using connection tubing with a greater internal diameter only slightly improves the situation. When the 10 l pressure vessel is connected in series with the supply, the pressure drop markedly decreases, with the configuration using eight millimetre connection tubing yielding the best results, though the corresponding drop in pressure is still greater than 50 kPa. Furthermore, while the inclusion of a pressure vessel

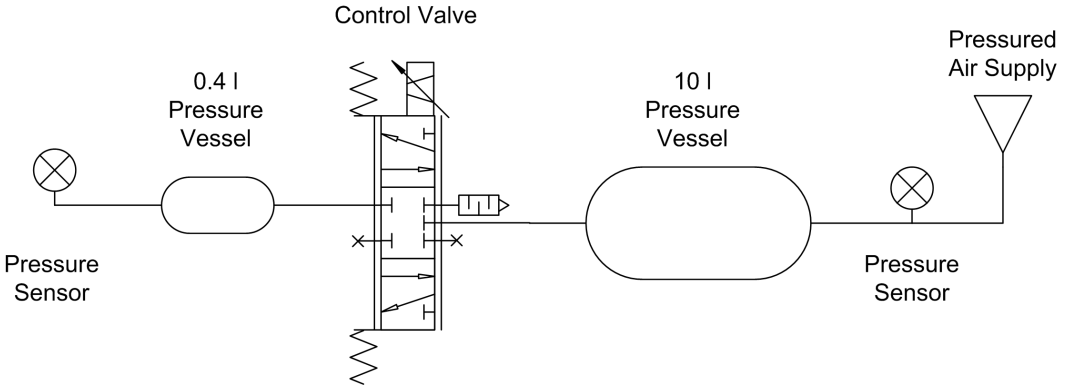

Figure E.1: Supply Pressure Experimental Setup (Diagram: J. v.d. Merwe)

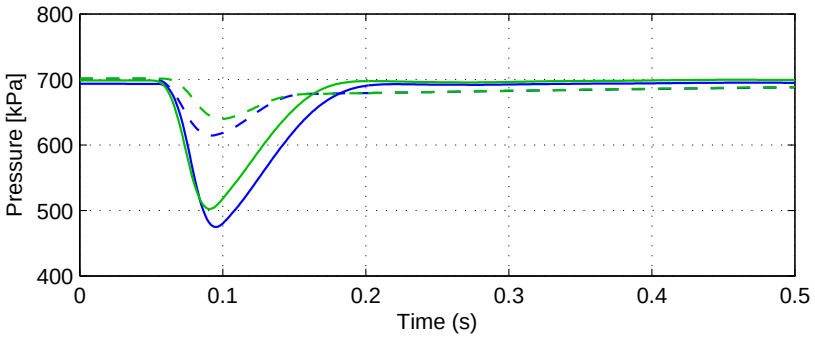

(a) Supply Pressure

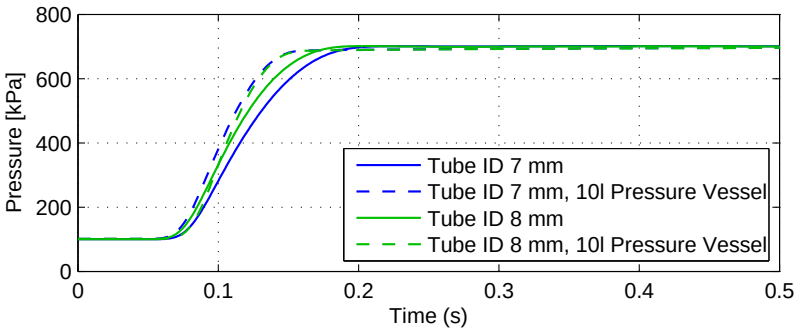

(b) Vessel Pressure

Figure E.2: Supply Pressure Evaluation (Graph: J. v.d. Merwe)

in series with the supply decreases the rise time for the pressure within the smaller vessel, as can be seen on the corresponding plot, it takes a considerably longer time for the supply pressure to reach the level attained before the valve was opened. This is due to the time it takes to refill the large vessel in the presence of a low pressure difference.

While the drop in supply pressure was not entirely negated, it was consid-

erably decreased. The possibility exists that, while the effects thereof is most severe for large valve openings, during the intended actuation of the various profiles the proportional valves might never be opened more than a fraction of the maximum, thereby further decreasing the drop in pressure. If a number of pneumatic circuits share the same supply line, and especially if the peaks of the various profiles correspond, the situation may, however, be aggravated further. Possible methods to overcome the difficulties associated with this include employing a dedicated, high flow-rate air compression system, as well as control schemes taking into account the effects of variations in supply pressure.

Appendix F

Pneumatic Cushioning

In order to prevent damage and prolong a cylinder's life, some form of cushioning is normally implemented at the stroke ends. Methods used include shock absorbing pads, electronic compensation and adjustable pneumatic cushioning - the latter of which is relevant to this thesis.

Modern cylinders with pneumatic cushioning employ seals that serve both as a seal and a non-return valve (Beater, 2007), which is also the case for Festo's DNC type cylinders used here and similar to that illustrated in Figure F.1. These seals feature evenly spaced protrusions on a surface opposite to which sealing occurs during motion of the cylinder towards the stroke end.

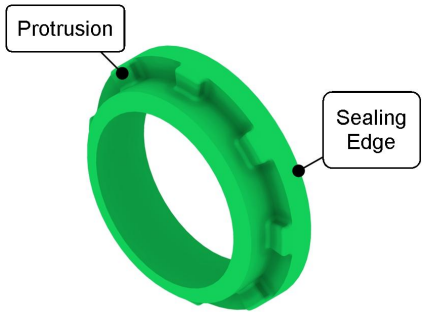

Figure F.1: Cushion Seal
(Illustration: J. v.d. Merwe; Notations: Beater (2007))

Figure F.2 illustrates the function of adjustable pneumatic cushioning. As the cushion spear passes through the seal, the seal is moved towards the stroke end and caused to press against the end cap, thereby preventing air from exhausting either through its centre as it normally would, or through the gaps between the seal's protrusions as during charging. Air is now forced to move through a flow path which may be further restricted by an adjustable screw. At high speed the piston would therefore displace air faster than which it is able to escape past the screw, causing a build-up of back pressure and the

piston to de-accelerate. When the chamber is charged, however, the seal is pushed towards the piston so that its protrusions presses against the opposing surface of the end cap. Since air is able to pass between these protrusions into the chamber, as previously mentioned, pressure is applied to the piston's entire surface area, resulting in maximum force.

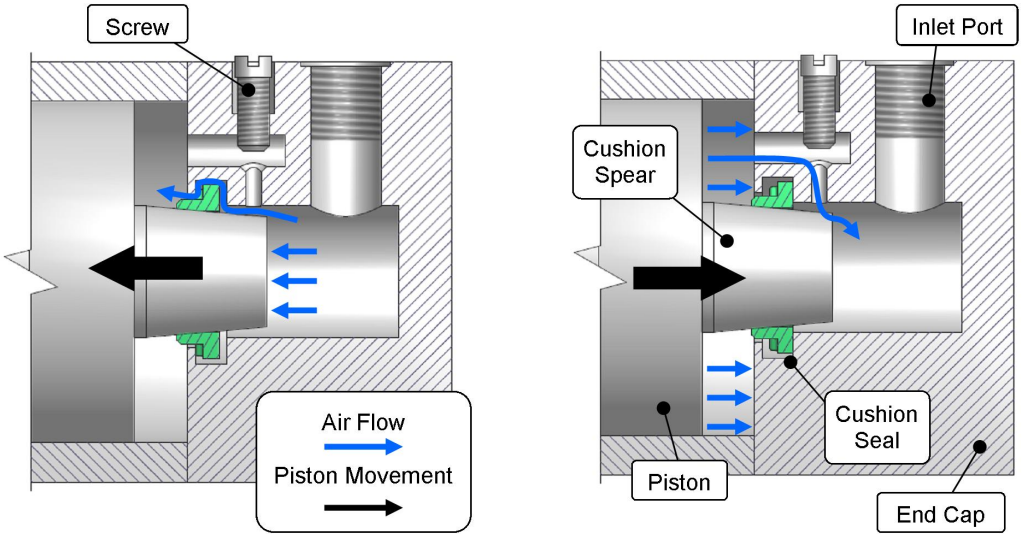

(a) Charging (b) Discharging

Figure F.2: Adjustable Pneumatic Cushioning (Adapted from Beater (2007))

While the effects of pneumatic cushioning are not strictly modelled here, as for example by Najafi *et al.* (2009), an understanding of its function has led to the conclusion that it is best disabled during the parameter identification procedures discussed in Chapter 4. This is because its presence alters normal cylinder behaviour by introducing back pressure build-up towards the stroke ends. Cushioning must be disabled not merely by releasing the screw as much as possible, as the flow path it no longer restricts is still considerably smaller than that obstructed by the cushioning spear. Therefore, it is suggested that both the cushioning seal and spear be removed during paramater identification procedures. Care should be taken, however, that the cylinder is not damaged during the experiments, as it would have no stroke-end protection.

During normal operation, the components required for cushioning may remain assembled with no foreseen introduction of un-modelled behaviour, given that the actuated stroke range does not cause the cushioning spear to enter the relevant seal at either end of the cylinder. Needless to say, if a cylinder with intact pneumatic cushioning is used, the active cushioning lengths at both stroke ends must be taken into account during cylinder stroke selection to ensure that this does not occur.

Appendix G

Geometric Orifice Model

The modelling approach followed by Richer and Hurmuzlu (2000) yields the exposed orifice area for both channels of the valve, A and B respectively, as a function of the spool position, x_{sp}. Equation G.1's derivation is based on the two dimensional geometry of the participating components, as shown in Figure G.1.

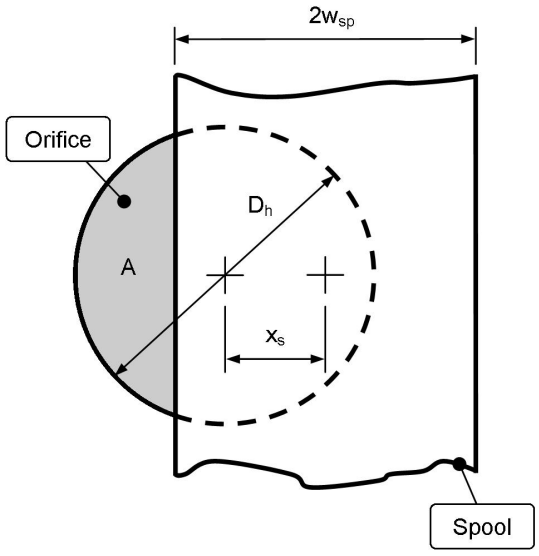

Figure G.1: Exposed Orifice Area versus Spool Position (Adapted from Richer and Hurmuzlu (2000))

$$
\begin{aligned}
A_{A_{in}} \\ A_{B_{ex}}
\end{aligned} = \begin{cases}
0, \text{ if } x_{sp} \leq w_{sp} - \frac{1}{2}D_h \\
n_h \left[D_h^2 \tan^{-1} \left(\sqrt{\frac{\frac{1}{2}D_h - w_{sp} + x_{sp}}{\frac{1}{2}D_h + w_{sp} - x_{sp}}} \right) - (w_{sp} - x_{sp}) \sqrt{\frac{D_h^2}{4} - (w_{sp} - x_{sp})^2} \right] \\
\text{if } w_{sp} - \frac{1}{2}D_h < x_{sp} < w_{sp} - \frac{1}{2}D_h \\
\pi n_h \frac{1}{4} D_h^2, \text{ if } x_{sp} \geq w_{sp} + \frac{1}{2}D_h
\end{cases}
$$

$$
\begin{aligned}
A_{A_{ex}} \\ A_{B_{in}}
\end{aligned} = \begin{cases}
\pi n_h \frac{1}{4} D_h^2, \text{ if } x_{sp} \leq -w_{sp} - \frac{1}{2}D_h \\
n_h \left[D_h^2 \tan^{-1} \left(\sqrt{\frac{\frac{1}{2}D_h - w_{sp} + |x_{sp}|}{\frac{1}{2}D_h + w_{sp} - |x_{sp}|}} \right) - (w_{sp} - |x_{sp}|) \sqrt{\frac{D_h^2}{4} - (w_{sp} - |x_{sp}|)^2} \right] \\
\text{if } -w_{sp} - \frac{1}{2}D_h < x_{sp} < -w_{sp} + \frac{1}{2}D_h \\
0, \text{ if } x_{sp} \geq -w_{sp} + \frac{1}{2}D_h
\end{cases} \tag{G.1}
$$

Here A_A and A_B are the exposed orifice areas of the two channels for a given spool position, where the subscripts in and ex denotes whether the channel in question is serving as an inlet or exhaust, or, alternatively, whether the control volume is being charged or discharged. Note the implied symmetry between the inlet and exhaust path's orifice areas, which may not be the actual case.

Parameters such as D_h, the nominal bore diameter, and n_h, the number of orifices within the flow path, can be determined from the manufacturer's data sheet. The spool's width, denoted by $2w_{sp}$, which is typically slightly larger than the diameter of the orifice to ensure flow is blocked even if the spool is slightly misaligned, is usually not given, and must be measured. This, however, requires the disassembly of the valve, as does the model proposed by Richer and Hurmuzlu in order to identify the parameters required to determine the spool's position x_{sp}. Since the dynamics of the valve's spool is neglected in this work, the following relation for the spool's position is used instead:

$$
x_{sp} = 2w_{sp} \left(\frac{u - u_b}{u_b} \right) \tag{G.2}
$$

Equation G.2 assumes a linear relationship between the spool's position and the input control signal, u. Furthermore, the control signal bias, at wich corresponding spool position flow to both channels are blocked, is denoted by u_b, and the range of said input by $2u_b$. For the sake of illustration, the spool's width is assumed to be equal to the diameter of the orifice, thereby allowing the exposed orifice areas from Equation G.1 to be plotted against the input control signal, which for Festo's MPYE type valves used here ranges between 0 and 10 V and is biased to the intended neutral position at 5 V, in Figure G.2.

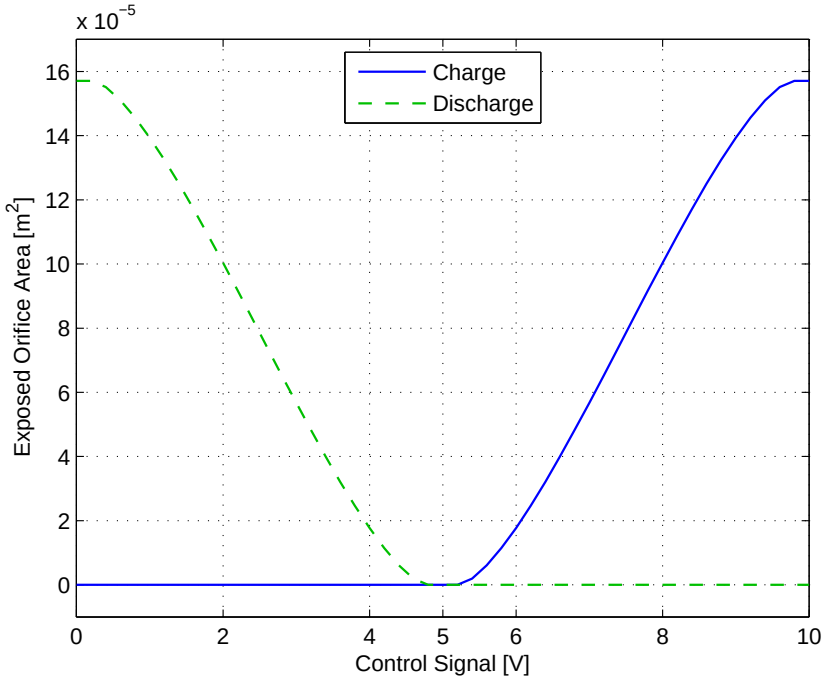

Figure G.2: 2D Exposed Orifice Area
(Graph: J. v.d. Merwe)

Appendix H

Test Protocols

Friction identification tests were conducted by applying a square wave signal to the valve's input. The particular signal applied was tailored such that, for each successive test, piston velocity would marginally increase while exhibiting similar magnitudes for the positive and negative directions. The values listed in Table H.1 describe square wave signal inputs eliciting the desired response from Festo's DNC-50-160-PPV-A cylinder used in this thesis, arranged in terms of increasing resultant velocity. If a different cylinder is used, the test protocol would need to be adjusted suitably.

Table H.1: Friction Model Test Protocol

Dataset [#]	Amplitude [V]	Offset [V]	Frequency [Hz]	Duty Cycle [%]
1	0.45	5.00	0.02	50
2	0.48	5.02	0.02	50
3	0.51	5.04	0.02	50
4	0.54	5.06	0.02	50
5	0.57	5.08	0.02	50
6	0.60	5.10	0.02	50
7	0.63	5.12	0.40	50
8	0.66	5.12	0.05	50
9	0.68	5.12	0.08	50
10	0.70	5.12	0.08	50
11	0.72	5.12	0.08	50
12	0.74	5.12	0.10	50
13	0.76	5.12	0.10	50
14	0.78	5.12	0.10	50
15	0.80	5.12	0.16	50
16	0.82	5.12	0.16	50
17	0.84	5.12	0.16	50
18	0.86	5.12	0.16	50
19	0.88	5.12	0.20	50
20	0.90	5.12	0.20	50

Table H.2 lists the square wave signal values used to identify the orifice models' parameters. Such tests were performed individually for Channels A and B's charge and discharge cases, and are relevant to Festo's MPYE-type valves.

Table H.2: Orifice Model Test Protocol

Signal [V]	Amplitude [V]	Offset [V]	Frequency [Hz]	Duty Cycle [%]
Channel A Charge/Channel B Discharge				
5.00	2.50	2.50	0.05	90
5.20	2.60	2.60	0.05	90
5.40	2.70	2.70	0.05	90
5.60	2.80	2.80	0.05	90
5.80	2.90	2.90	0.20	70
6.00	3.00	3.00	0.20	70
6.20	3.10	3.10	0.20	70
6.40	3.20	3.20	0.20	70
6.60	3.30	3.30	0.20	70
6.80	3.40	3.40	0.20	70
7.00	3.50	3.50	0.20	70
7.20	3.60	3.60	0.20	70
7.40	3.70	3.70	0.20	70
7.60	3.80	3.80	0.20	70
7.80	3.90	3.90	0.20	70
8.00	4.00	4.00	0.20	70
8.20	4.10	4.10	0.20	70
8.40	4.20	4.20	0.20	70
8.60	4.30	4.30	0.20	70
8.80	4.40	4.40	0.20	70
9.00	4.50	4.50	0.20	70
9.20	4.60	4.60	0.20	70
9.40	4.70	4.70	0.20	70
9.60	4.80	4.80	0.20	70
9.80	4.90	4.90	0.20	70
10.00	5.00	5.00	0.20	70
Channel A Disharge/Channel B Charge				
5.00	2.50	7.50	0.05	10
4.80	2.60	7.40	0.05	10
4.60	2.70	7.30	0.05	10
4.40	2.80	7.20	0.05	10
4.20	2.90	7.10	0.20	30
4.00	3.00	7.00	0.20	30
3.80	3.10	6.90	0.20	30
3.60	3.20	6.80	0.20	30
3.40	3.30	6.70	0.20	30
3.20	3.40	6.60	0.20	30
3.00	3.50	6.50	0.20	30
2.80	3.60	6.40	0.20	30
2.60	3.70	6.30	0.20	30
2.40	3.80	6.20	0.20	30
2.20	3.90	6.10	0.20	30
2.00	4.00	6.00	0.20	30
1.80	4.10	5.90	0.20	30
1.60	4.20	5.80	0.20	30
1.40	4.30	5.70	0.20	30
1.20	4.40	5.60	0.20	30
1.00	4.50	5.50	0.20	30
0.80	4.60	5.40	0.20	30
0.60	4.70	5.30	0.20	30
0.40	4.80	5.20	0.20	30
0.20	4.90	5.10	0.20	30
0.00	5.00	5.00	0.20	30

Appendix I

Model Parameters

Table I.1: Miscellaneous Pneumatic Actuator Parameters

Parameter	Value	Parameter	Value	Parameter	Value
m_L	0 kg	A_{p_A}	1.96E-03 m^2	cp	1005 $m^2.s^{-2}.K^{-1}$
m_p	0.538 kg	A_{p_B}	1.65E-03 m^2	cv	718 $m^2.s^{-2}.K^{-1}$
m_r	0.4 kg	A_r	3.14E-04 m^2	γ	1.4
L	0.16 m	V_{0_A}	7.65E-05 m^3	α_{in}	1.4
D_p	0.05 m	V_{0_B}	7.25E-05 m^3	α_{ex}	1
D_r	0.01 m			α	1.2

Table I.2: Friction Model Parameters

Parameter	Positive Velocity	Negative Velocity
F_{sf}	21.065 N	12.770 N
F_{cf}	43.156 N	38.646 N
C_{vf}	91.729 N	96.025 N
$\dot{x}_s$	0.098 $m.s^{-1}$	0.094 $m.s^{-1}$
δ	1.641	1.773
ε	0.010 $m.s^{-1}$	0.010 N

Table I.3: Miscellaneous Valve Parameters

Parameter	Value	Parameter	Value
D_h	0.01 m	$C_{d_{Festo}}$	0.575
A_{max}	7.85E-05 m^2	u_b	5 V
w_{sp}	0.01 m	V_v	0.4 l
n_h	2	P_{cr}	0.528

Table I.4: Theoretical ψ Constant Cd Inlet Parameters

	Channel A				Channel B			
u	A_{eff}	b	a	β	A_{eff}	b	a	β
0.0	0	0.528	1	0.5	4.11E-05	0.528	1	0.5
0.2	0	0.528	1	0.5	4.11E-05	0.528	1	0.5
0.4	0	0.528	1	0.5	4.01E-05	0.528	1	0.5
0.6	0	0.528	1	0.5	3.98E-05	0.528	1	0.5
0.8	0	0.528	1	0.5	3.93E-05	0.528	1	0.5
1.0	0	0.528	1	0.5	3.88E-05	0.528	1	0.5
1.2	0	0.528	1	0.5	3.78E-05	0.528	1	0.5
1.4	0	0.528	1	0.5	3.76E-05	0.528	1	0.5
1.6	0	0.528	1	0.5	3.68E-05	0.528	1	0.5
1.8	0	0.528	1	0.5	3.55E-05	0.528	1	0.5
2.0	0	0.528	1	0.5	3.44E-05	0.528	1	0.5
2.2	0	0.528	1	0.5	3.28E-05	0.528	1	0.5
2.4	0	0.528	1	0.5	3.15E-05	0.528	1	0.5
2.6	0	0.528	1	0.5	2.98E-05	0.528	1	0.5
2.8	0	0.528	1	0.5	2.80E-05	0.528	1	0.5
3.0	0	0.528	1	0.5	2.58E-05	0.528	1	0.5
3.2	0	0.528	1	0.5	2.33E-05	0.528	1	0.5
3.4	0	0.528	1	0.5	2.04E-05	0.528	1	0.5
3.6	0	0.528	1	0.5	1.73E-05	0.528	1	0.5
3.8	0	0.528	1	0.5	1.40E-05	0.528	1	0.5
4.0	0	0.528	1	0.5	1.02E-05	0.528	1	0.5
4.2	0	0.528	1	0.5	5.89E-06	0.528	1	0.5
4.4	0	0.528	1	0.5	1.49E-06	0.528	1	0.5
4.6	0	0.528	1	0.5	1.36E-07	0.528	1	0.5
4.8	0	0.528	1	0.5	1.07E-07	0.528	1	0.5
5.0	9.11E-08	0.528	1	0.5	9.23E-08	0.528	1	0.5
5.2	1.04E-07	0.528	1	0.5	0	0.528	1	0.5
5.4	1.19E-07	0.528	1	0.5	0	0.528	1	0.5
5.6	1.47E-07	0.528	1	0.5	0	0.528	1	0.5
5.8	8.90E-07	0.528	1	0.5	0	0.528	1	0.5
6.0	4.97E-06	0.528	1	0.5	0	0.528	1	0.5
6.2	9.34E-06	0.528	1	0.5	0	0.528	1	0.5
6.4	1.31E-05	0.528	1	0.5	0	0.528	1	0.5
6.6	1.65E-05	0.528	1	0.5	0	0.528	1	0.5
6.8	1.97E-05	0.528	1	0.5	0	0.528	1	0.5
7.0	2.25E-05	0.528	1	0.5	0	0.528	1	0.5
7.2	2.50E-05	0.528	1	0.5	0	0.528	1	0.5
7.4	2.72E-05	0.528	1	0.5	0	0.528	1	0.5
7.6	2.94E-05	0.528	1	0.5	0	0.528	1	0.5
7.8	3.10E-05	0.528	1	0.5	0	0.528	1	0.5
8.0	3.28E-05	0.528	1	0.5	0	0.528	1	0.5
8.2	3.40E-05	0.528	1	0.5	0	0.528	1	0.5
8.4	3.55E-05	0.528	1	0.5	0	0.528	1	0.5
8.6	3.64E-05	0.528	1	0.5	0	0.528	1	0.5
8.8	3.78E-05	0.528	1	0.5	0	0.528	1	0.5
9.0	3.85E-05	0.528	1	0.5	0	0.528	1	0.5
9.2	3.89E-05	0.528	1	0.5	0	0.528	1	0.5
9.4	3.93E-05	0.528	1	0.5	0	0.528	1	0.5
9.6	3.98E-05	0.528	1	0.5	0	0.528	1	0.5
9.8	4.05E-05	0.528	1	0.5	0	0.528	1	0.5
10.0	4.03E-05	0.528	1	0.5	0	0.528	1	0.5

Table I.5: Theoretical ψ Constant Cd Exhaust Parameters

	Channel A				Channel B			
u	A_{eff}	b	a	β	A_{eff}	b	a	β
0.0	6.02E-05	0.528	1	0.5	0	0.528	1	0.5
0.2	5.99E-05	0.528	1	0.5	0	0.528	1	0.5
0.4	5.98E-05	0.528	1	0.5	0	0.528	1	0.5
0.6	6.00E-05	0.528	1	0.5	0	0.528	1	0.5
0.8	5.81E-05	0.528	1	0.5	0	0.528	1	0.5
1.0	5.77E-05	0.528	1	0.5	0	0.528	1	0.5
1.2	5.60E-05	0.528	1	0.5	0	0.528	1	0.5
1.4	5.54E-05	0.528	1	0.5	0	0.528	1	0.5
1.6	5.34E-05	0.528	1	0.5	0	0.528	1	0.5
1.8	5.26E-05	0.528	1	0.5	0	0.528	1	0.5
2.0	5.01E-05	0.528	1	0.5	0	0.528	1	0.5
2.2	4.80E-05	0.528	1	0.5	0	0.528	1	0.5
2.4	4.54E-05	0.528	1	0.5	0	0.528	1	0.5
2.6	4.30E-05	0.528	1	0.5	0	0.528	1	0.5
2.8	4.00E-05	0.528	1	0.5	0	0.528	1	0.5
3.0	3.71E-05	0.528	1	0.5	0	0.528	1	0.5
3.2	3.36E-05	0.528	1	0.5	0	0.528	1	0.5
3.4	2.94E-05	0.528	1	0.5	0	0.528	1	0.5
3.6	2.49E-05	0.528	1	0.5	0	0.528	1	0.5
3.8	1.99E-05	0.528	1	0.5	0	0.528	1	0.5
4.0	1.44E-05	0.528	1	0.5	0	0.528	1	0.5
4.2	8.69E-06	0.528	1	0.5	0	0.528	1	0.5
4.4	1.87E-06	0.528	1	0.5	0	0.528	1	0.5
4.6	1.31E-07	0.528	1	0.5	0	0.528	1	0.5
4.8	8.01E-08	0.528	1	0.5	0	0.528	1	0.5
5.0	6.21E-08	0.528	1	0.5	5.29E-08	0.528	1	0.5
5.2	0	0.528	1	0.5	6.62E-08	0.528	1	0.5
5.4	0	0.528	1	0.5	8.37E-08	0.528	1	0.5
5.6	0	0.528	1	0.5	1.21E-07	0.528	1	0.5
5.8	0	0.528	1	0.5	7.47E-07	0.528	1	0.5
6.0	0	0.528	1	0.5	6.23E-06	0.528	1	0.5
6.2	0	0.528	1	0.5	1.21E-05	0.528	1	0.5
6.4	0	0.528	1	0.5	1.79E-05	0.528	1	0.5
6.6	0	0.528	1	0.5	2.36E-05	0.528	1	0.5
6.8	0	0.528	1	0.5	2.88E-05	0.528	1	0.5
7.0	0	0.528	1	0.5	3.36E-05	0.528	1	0.5
7.2	0	0.528	1	0.5	3.79E-05	0.528	1	0.5
7.4	0	0.528	1	0.5	4.19E-05	0.528	1	0.5
7.6	0	0.528	1	0.5	4.57E-05	0.528	1	0.5
7.8	0	0.528	1	0.5	4.88E-05	0.528	1	0.5
8.0	0	0.528	1	0.5	5.18E-05	0.528	1	0.5
8.2	0	0.528	1	0.5	5.44E-05	0.528	1	0.5
8.4	0	0.528	1	0.5	5.67E-05	0.528	1	0.5
8.6	0	0.528	1	0.5	5.87E-05	0.528	1	0.5
8.8	0	0.528	1	0.5	6.06E-05	0.528	1	0.5
9.0	0	0.528	1	0.5	6.22E-05	0.528	1	0.5
9.2	0	0.528	1	0.5	6.38E-05	0.528	1	0.5
9.4	0	0.528	1	0.5	6.44E-05	0.528	1	0.5
9.6	0	0.528	1	0.5	6.60E-05	0.528	1	0.5
9.8	0	0.528	1	0.5	6.72E-05	0.528	1	0.5
10.0	0	0.528	1	0.5	6.81E-05	0.528	1	0.5

Table I.6: Theoretical ψ Variable Cd Inlet Parameters

	Channel A				Channel B			
u	A_{eff}	b	a	β	A_{eff}	b	a	β
0.0	0	0.528	1	0.5	3.32E-05	0.528	1	0.5
0.2	0	0.528	1	0.5	3.35E-05	0.528	1	0.5
0.4	0	0.528	1	0.5	3.23E-05	0.528	1	0.5
0.6	0	0.528	1	0.5	3.23E-05	0.528	1	0.5
0.8	0	0.528	1	0.5	3.18E-05	0.528	1	0.5
1.0	0	0.528	1	0.5	3.16E-05	0.528	1	0.5
1.2	0	0.528	1	0.5	3.06E-05	0.528	1	0.5
1.4	0	0.528	1	0.5	3.08E-05	0.528	1	0.5
1.6	0	0.528	1	0.5	3.04E-05	0.528	1	0.5
1.8	0	0.528	1	0.5	2.92E-05	0.528	1	0.5
2.0	0	0.528	1	0.5	2.84E-05	0.528	1	0.5
2.2	0	0.528	1	0.5	2.71E-05	0.528	1	0.5
2.4	0	0.528	1	0.5	2.64E-05	0.528	1	0.5
2.6	0	0.528	1	0.5	2.50E-05	0.528	1	0.5
2.8	0	0.528	1	0.5	2.37E-05	0.528	1	0.5
3.0	0	0.528	1	0.5	2.18E-05	0.528	1	0.5
3.2	0	0.528	1	0.5	1.98E-05	0.528	1	0.5
3.4	0	0.528	1	0.5	1.75E-05	0.528	1	0.5
3.6	0	0.528	1	0.5	1.49E-05	0.528	1	0.5
3.8	0	0.528	1	0.5	1.20E-05	0.528	1	0.5
4.0	0	0.528	1	0.5	8.72E-06	0.528	1	0.5
4.2	0	0.528	1	0.5	5.12E-06	0.528	1	0.5
4.4	0	0.528	1	0.5	1.45E-06	0.528	1	0.5
4.6	0	0.528	1	0.5	1.90E-07	0.528	1	0.5
4.8	0	0.528	1	0.5	1.31E-07	0.528	1	0.5
5.0	9.99E-08	0.528	1	0.5	1.02E-07	0.528	1	0.5
5.2	1.23E-07	0.528	1	0.5	0	0.528	1	0.5
5.4	1.54E-07	0.528	1	0.5	0	0.528	1	0.5
5.6	2.11E-07	0.528	1	0.5	0	0.528	1	0.5
5.8	9.07E-07	0.528	1	0.5	0	0.528	1	0.5
6.0	4.27E-06	0.528	1	0.5	0	0.528	1	0.5
6.2	7.86E-06	0.528	1	0.5	0	0.528	1	0.5
6.4	1.10E-05	0.528	1	0.5	0	0.528	1	0.5
6.6	1.40E-05	0.528	1	0.5	0	0.528	1	0.5
6.8	1.66E-05	0.528	1	0.5	0	0.528	1	0.5
7.0	1.89E-05	0.528	1	0.5	0	0.528	1	0.5
7.2	2.09E-05	0.528	1	0.5	0	0.528	1	0.5
7.4	2.27E-05	0.528	1	0.5	0	0.528	1	0.5
7.6	2.46E-05	0.528	1	0.5	0	0.528	1	0.5
7.8	2.56E-05	0.528	1	0.5	0	0.528	1	0.5
8.0	2.72E-05	0.528	1	0.5	0	0.528	1	0.5
8.2	2.79E-05	0.528	1	0.5	0	0.528	1	0.5
8.4	2.92E-05	0.528	1	0.5	0	0.528	1	0.5
8.6	2.97E-05	0.528	1	0.5	0	0.528	1	0.5
8.8	3.09E-05	0.528	1	0.5	0	0.528	1	0.5
9.0	3.14E-05	0.528	1	0.5	0	0.528	1	0.5
9.2	3.15E-05	0.528	1	0.5	0	0.528	1	0.5
9.4	3.19E-05	0.528	1	0.5	0	0.528	1	0.5
9.6	3.22E-05	0.528	1	0.5	0	0.528	1	0.5
9.8	3.30E-05	0.528	1	0.5	0	0.528	1	0.5
10.0	3.25E-05	0.528	1	0.5	0	0.528	1	0.5

Table I.7: Theoretical ψ Variable Cd Exhaust Parameters

	Channel A				Channel B			
u	A_{eff}	b	a	β	A_{eff}	b	a	β
0.0	4.30E-05	0.528	1	0.5	0	0.528	1	0.5
0.2	4.28E-05	0.528	1	0.5	0	0.528	1	0.5
0.4	4.27E-05	0.528	1	0.5	0	0.528	1	0.5
0.6	4.30E-05	0.528	1	0.5	0	0.528	1	0.5
0.8	4.15E-05	0.528	1	0.5	0	0.528	1	0.5
1.0	4.12E-05	0.528	1	0.5	0	0.528	1	0.5
1.2	4.00E-05	0.528	1	0.5	0	0.528	1	0.5
1.4	3.96E-05	0.528	1	0.5	0	0.528	1	0.5
1.6	3.81E-05	0.528	1	0.5	0	0.528	1	0.5
1.8	3.76E-05	0.528	1	0.5	0	0.528	1	0.5
2.0	3.58E-05	0.528	1	0.5	0	0.528	1	0.5
2.2	3.43E-05	0.528	1	0.5	0	0.528	1	0.5
2.4	3.24E-05	0.528	1	0.5	0	0.528	1	0.5
2.6	3.07E-05	0.528	1	0.5	0	0.528	1	0.5
2.8	2.86E-05	0.528	1	0.5	0	0.528	1	0.5
3.0	2.66E-05	0.528	1	0.5	0	0.528	1	0.5
3.2	2.41E-05	0.528	1	0.5	0	0.528	1	0.5
3.4	2.11E-05	0.528	1	0.5	0	0.528	1	0.5
3.6	1.79E-05	0.528	1	0.5	0	0.528	1	0.5
3.8	1.43E-05	0.528	1	0.5	0	0.528	1	0.5
4.0	1.04E-05	0.528	1	0.5	0	0.528	1	0.5
4.2	6.36E-06	0.528	1	0.5	0	0.528	1	0.5
4.4	1.85E-06	0.528	1	0.5	0	0.528	1	0.5
4.6	9.11E-08	0.528	1	0.5	0	0.528	1	0.5
4.8	5.56E-08	0.528	1	0.5	0	0.528	1	0.5
5.0	4.30E-08	0.528	1	0.5	3.66E-08	0.528	1	0.5
5.2	0	0.528	1	0.5	4.59E-08	0.528	1	0.5
5.4	0	0.528	1	0.5	5.82E-08	0.528	1	0.5
5.6	0	0.528	1	0.5	8.47E-08	0.528	1	0.5
5.8	0	0.528	1	0.5	6.32E-07	0.528	1	0.5
6.0	0	0.528	1	0.5	4.65E-06	0.528	1	0.5
6.2	0	0.528	1	0.5	8.88E-06	0.528	1	0.5
6.4	0	0.528	1	0.5	1.31E-05	0.528	1	0.5
6.6	0	0.528	1	0.5	1.72E-05	0.528	1	0.5
6.8	0	0.528	1	0.5	2.10E-05	0.528	1	0.5
7.0	0	0.528	1	0.5	2.45E-05	0.528	1	0.5
7.2	0	0.528	1	0.5	2.77E-05	0.528	1	0.5
7.4	0	0.528	1	0.5	3.07E-05	0.528	1	0.5
7.6	0	0.528	1	0.5	3.34E-05	0.528	1	0.5
7.8	0	0.528	1	0.5	3.57E-05	0.528	1	0.5
8.0	0	0.528	1	0.5	3.79E-05	0.528	1	0.5
8.2	0	0.528	1	0.5	3.98E-05	0.528	1	0.5
8.4	0	0.528	1	0.5	4.15E-05	0.528	1	0.5
8.6	0	0.528	1	0.5	4.30E-05	0.528	1	0.5
8.8	0	0.528	1	0.5	4.44E-05	0.528	1	0.5
9.0	0	0.528	1	0.5	4.57E-05	0.528	1	0.5
9.2	0	0.528	1	0.5	4.69E-05	0.528	1	0.5
9.4	0	0.528	1	0.5	4.72E-05	0.528	1	0.5
9.6	0	0.528	1	0.5	4.85E-05	0.528	1	0.5
9.8	0	0.528	1	0.5	4.94E-05	0.528	1	0.5
10.0	0	0.528	1	0.5	5.01E-05	0.528	1	0.5

Table I.8: ISO ψ Constant Cd Inlet Parameters

	Channel A				Channel B			
u	A_{eff}	b	a	β	A_{eff}	b	a	β
0.0	0	5.28E-01	1	0.5	4.11E-05	5.28E-01	1	0.5
0.2	0	5.28E-01	1	0.5	4.11E-05	5.28E-01	1	0.5
0.4	0	5.28E-01	1	0.5	4.01E-05	5.28E-01	1	0.5
0.6	0	5.28E-01	1	0.5	3.98E-05	5.28E-01	1	0.5
0.8	0	5.28E-01	1	0.5	3.93E-05	5.28E-01	1	0.5
1.0	0	5.28E-01	1	0.5	3.88E-05	5.28E-01	1	0.5
1.2	0	5.28E-01	1	0.5	3.78E-05	5.28E-01	1	0.5
1.4	0	5.28E-01	1	0.5	3.76E-05	5.28E-01	1	0.5
1.6	0	5.28E-01	1	0.5	3.68E-05	5.28E-01	1	0.5
1.8	0	5.28E-01	1	0.5	3.55E-05	5.28E-01	1	0.5
2.0	0	5.28E-01	1	0.5	3.44E-05	5.28E-01	1	0.5
2.2	0	5.28E-01	1	0.5	3.28E-05	5.28E-01	1	0.5
2.4	0	5.28E-01	1	0.5	3.17E-05	5.07E-01	1	0.5
2.6	0	5.28E-01	1	0.5	3.02E-05	4.88E-01	1	0.5
2.8	0	5.28E-01	1	0.5	2.86E-05	4.57E-01	1	0.5
3.0	0	5.28E-01	1	0.5	2.65E-05	4.43E-01	1	0.5
3.2	0	5.28E-01	1	0.5	2.42E-05	4.12E-01	1	0.5
3.4	0	5.28E-01	1	0.5	2.14E-05	3.74E-01	1	0.5
3.6	0	5.28E-01	1	0.5	1.85E-05	3.19E-01	1	0.5
3.8	0	5.28E-01	1	0.5	1.50E-05	2.94E-01	1	0.5
4.0	0	5.28E-01	1	0.5	1.10E-05	2.83E-01	1	0.5
4.2	0	5.28E-01	1	0.5	6.95E-06	2.22E-02	1	0.5
4.4	0	5.28E-01	1	0.5	1.84E-06	3.88E-14	1	0.5
4.6	0	5.28E-01	1	0.5	1.88E-07	3.54E-14	1	0.5
4.8	0	5.28E-01	1	0.5	1.46E-07	4.05E-14	1	0.5
5.0	1.20E-07	3.10E-14	1	0.5	1.22E-07	3.06E-14	1	0.5
5.2	1.40E-07	2.78E-14	1	0.5	0	5.28E-01	1	0.5
5.4	1.63E-07	3.86E-14	1	0.5	0	5.28E-01	1	0.5
5.6	2.05E-07	3.38E-14	1	0.5	0	5.28E-01	1	0.5
5.8	1.12E-06	3.35E-14	1	0.5	0	5.28E-01	1	0.5
6.0	5.40E-06	2.59E-01	1	0.5	0	5.28E-01	1	0.5
6.2	9.60E-06	4.38E-01	1	0.5	0	5.28E-01	1	0.5
6.4	1.35E-05	4.18E-01	1	0.5	0	5.28E-01	1	0.5
6.6	1.72E-05	4.02E-01	1	0.5	0	5.28E-01	1	0.5
6.8	2.03E-05	4.25E-01	1	0.5	0	5.28E-01	1	0.5
7.0	2.29E-05	4.59E-01	1	0.5	0	5.28E-01	1	0.5
7.2	2.53E-05	4.85E-01	1	0.5	0	5.28E-01	1	0.5
7.4	2.74E-05	5.01E-01	1	0.5	0	5.28E-01	1	0.5
7.6	2.97E-05	5.01E-01	1	0.5	0	5.28E-01	1	0.5
7.8	3.10E-05	5.28E-01	1	0.5	0	5.28E-01	1	0.5
8.0	3.28E-05	5.28E-01	1	0.5	0	5.28E-01	1	0.5
8.2	3.40E-05	5.28E-01	1	0.5	0	5.28E-01	1	0.5
8.4	3.55E-05	5.28E-01	1	0.5	0	5.28E-01	1	0.5
8.6	3.64E-05	5.28E-01	1	0.5	0	5.28E-01	1	0.5
8.8	3.78E-05	5.28E-01	1	0.5	0	5.28E-01	1	0.5
9.0	3.85E-05	5.28E-01	1	0.5	0	5.28E-01	1	0.5
9.2	3.89E-05	5.28E-01	1	0.5	0	5.28E-01	1	0.5
9.4	3.93E-05	5.28E-01	1	0.5	0	5.28E-01	1	0.5
9.6	3.98E-05	5.28E-01	1	0.5	0	5.28E-01	1	0.5
9.8	4.05E-05	5.28E-01	1	0.5	0	5.28E-01	1	0.5
10.0	4.03E-05	5.28E-01	1	0.5	0	5.28E-01	1	0.5

Table I.9: ISO ψ Constant Cd Exhaust Parameters

	Channel A				Channel B			
u	A_{eff}	b	a	β	A_{eff}	b	a	β
0.0	6.10E-05	2.61E-01	1	0.5	0	5.28E-01	1	0.5
0.2	6.17E-05	5.90E-02	1	0.5	0	5.28E-01	1	0.5
0.4	6.06E-05	2.46E-01	1	0.5	0	5.28E-01	1	0.5
0.6	6.09E-05	2.32E-01	1	0.5	0	5.28E-01	1	0.5
0.8	6.01E-05	4.14E-02	1	0.5	0	5.28E-01	1	0.5
1.0	5.85E-05	2.35E-01	1	0.5	0	5.28E-01	1	0.5
1.2	5.67E-05	2.44E-01	1	0.5	0	5.28E-01	1	0.5
1.4	5.62E-05	2.33E-01	1	0.5	0	5.28E-01	1	0.5
1.6	5.41E-05	2.35E-01	1	0.5	0	5.28E-01	1	0.5
1.8	5.34E-05	2.17E-01	1	0.5	0	5.28E-01	1	0.5
2.0	5.09E-05	2.24E-01	1	0.5	0	5.28E-01	1	0.5
2.2	4.87E-05	2.18E-01	1	0.5	0	5.28E-01	1	0.5
2.4	4.61E-05	2.16E-01	1	0.5	0	5.28E-01	1	0.5
2.6	4.37E-05	2.03E-01	1	0.5	0	5.28E-01	1	0.5
2.8	4.07E-05	1.93E-01	1	0.5	0	5.28E-01	1	0.5
3.0	3.78E-05	1.77E-01	1	0.5	0	5.28E-01	1	0.5
3.2	3.44E-05	1.60E-01	1	0.5	0	5.28E-01	1	0.5
3.4	3.01E-05	1.33E-01	1	0.5	0	5.28E-01	1	0.5
3.6	2.62E-05	1.61E-09	1	0.5	0	5.28E-01	1	0.5
3.8	2.09E-05	1.07E-09	1	0.5	0	5.28E-01	1	0.5
4.0	1.52E-05	4.93E-10	1	0.5	0	5.28E-01	1	0.5
4.2	9.23E-06	4.44E-14	1	0.5	0	5.28E-01	1	0.5
4.4	2.31E-06	3.34E-14	1	0.5	0	5.28E-01	1	0.5
4.6	1.35E-07	2.66E-14	1	0.5	0	5.28E-01	1	0.5
4.8	8.19E-08	2.68E-14	1	0.5	0	5.28E-01	1	0.5
5.0	6.33E-08	3.38E-14	1	0.5	5.39E-08	3.32E-14	1	0.5
5.2	0	5.28E-01	1	0.5	6.75E-08	3.24E-14	1	0.5
5.4	0	5.28E-01	1	0.5	8.57E-08	2.65E-14	1	0.5
5.6	0	5.28E-01	1	0.5	1.25E-07	3.31E-14	1	0.5
5.8	0	5.28E-01	1	0.5	8.83E-07	2.91E-14	1	0.5
6.0	0	5.28E-01	1	0.5	6.70E-06	3.55E-14	1	0.5
6.2	0	5.28E-01	1	0.5	1.29E-05	2.67E-10	1	0.5
6.4	0	5.28E-01	1	0.5	1.90E-05	9.18E-10	1	0.5
6.6	0	5.28E-01	1	0.5	2.50E-05	1.55E-09	1	0.5
6.8	0	5.28E-01	1	0.5	3.05E-05	2.13E-09	1	0.5
7.0	0	5.28E-01	1	0.5	3.56E-05	2.66E-09	1	0.5
7.2	0	5.28E-01	1	0.5	4.02E-05	3.14E-09	1	0.5
7.4	0	5.28E-01	1	0.5	4.45E-05	2.22E-14	1	0.5
7.6	0	5.28E-01	1	0.5	4.85E-05	2.22E-14	1	0.5
7.8	0	5.28E-01	1	0.5	5.18E-05	2.22E-14	1	0.5
8.0	0	5.28E-01	1	0.5	5.50E-05	2.22E-14	1	0.5
8.2	0	5.28E-01	1	0.5	5.78E-05	2.22E-14	1	0.5
8.4	0	5.28E-01	1	0.5	6.02E-05	2.22E-14	1	0.5
8.6	0	5.28E-01	1	0.5	6.24E-05	2.22E-14	1	0.5
8.8	0	5.28E-01	1	0.5	6.44E-05	2.22E-14	1	0.5
9.0	0	5.28E-01	1	0.5	6.62E-05	2.22E-14	1	0.5
9.2	0	5.28E-01	1	0.5	6.79E-05	2.22E-14	1	0.5
9.4	0	5.28E-01	1	0.5	6.84E-05	2.22E-14	1	0.5
9.6	0	5.28E-01	1	0.5	7.02E-05	2.22E-14	1	0.5
9.8	0	5.28E-01	1	0.5	7.15E-05	2.22E-14	1	0.5
10.0	0	5.28E-01	1	0.5	7.25E-05	2.22E-14	1	0.5

Table I.10: ISO ψ Variable Cd Inlet Parameters

	Channel A				Channel B			
u	A_{eff}	b	a	β	A_{eff}	b	a	β
0.0	0	5.28E-01	1	0.5	3.32E-05	5.28E-01	1	0.5
0.2	0	5.28E-01	1	0.5	3.35E-05	5.28E-01	1	0.5
0.4	0	5.28E-01	1	0.5	3.23E-05	5.28E-01	1	0.5
0.6	0	5.28E-01	1	0.5	3.23E-05	5.28E-01	1	0.5
0.8	0	5.28E-01	1	0.5	3.18E-05	5.28E-01	1	0.5
1.0	0	5.28E-01	1	0.5	3.16E-05	5.28E-01	1	0.5
1.2	0	5.28E-01	1	0.5	3.06E-05	5.28E-01	1	0.5
1.4	0	5.28E-01	1	0.5	3.08E-05	5.28E-01	1	0.5
1.6	0	5.28E-01	1	0.5	3.04E-05	5.28E-01	1	0.5
1.8	0	5.28E-01	1	0.5	2.92E-05	5.28E-01	1	0.5
2.0	0	5.28E-01	1	0.5	2.84E-05	5.28E-01	1	0.5
2.2	0	5.28E-01	1	0.5	2.71E-05	5.28E-01	1	0.5
2.4	0	5.28E-01	1	0.5	2.64E-05	5.28E-01	1	0.5
2.6	0	5.28E-01	1	0.5	2.50E-05	5.28E-01	1	0.5
2.8	0	5.28E-01	1	0.5	2.37E-05	5.28E-01	1	0.5
3.0	0	5.28E-01	1	0.5	2.18E-05	5.28E-01	1	0.5
3.2	0	5.28E-01	1	0.5	1.98E-05	5.28E-01	1	0.5
3.4	0	5.28E-01	1	0.5	1.75E-05	5.28E-01	1	0.5
3.6	0	5.28E-01	1	0.5	1.49E-05	5.28E-01	1	0.5
3.8	0	5.28E-01	1	0.5	1.20E-05	5.28E-01	1	0.5
4.0	0	5.28E-01	1	0.5	8.72E-06	5.28E-01	1	0.5
4.2	0	5.28E-01	1	0.5	5.12E-06	5.28E-01	1	0.5
4.4	0	5.28E-01	1	0.5	1.45E-06	5.28E-01	1	0.5
4.6	0	5.28E-01	1	0.5	2.32E-07	3.08E-14	1	0.5
4.8	0	5.28E-01	1	0.5	1.63E-07	4.38E-14	1	0.5
5.0	1.24E-07	2.77E-14	1	0.5	1.28E-07	2.74E-14	1	0.5
5.2	1.53E-07	2.54E-14	1	0.5	0	5.28E-01	1	0.5
5.4	1.90E-07	3.28E-14	1	0.5	0	5.28E-01	1	0.5
5.6	2.54E-07	3.16E-14	1	0.5	0	5.28E-01	1	0.5
5.8	9.07E-07	5.28E-01	1	0.5	0	5.28E-01	1	0.5
6.0	4.27E-06	5.28E-01	1	0.5	0	5.28E-01	1	0.5
6.2	7.86E-06	5.28E-01	1	0.5	0	5.28E-01	1	0.5
6.4	1.10E-05	5.28E-01	1	0.5	0	5.28E-01	1	0.5
6.6	1.40E-05	5.28E-01	1	0.5	0	5.28E-01	1	0.5
6.8	1.66E-05	5.28E-01	1	0.5	0	5.28E-01	1	0.5
7.0	1.89E-05	5.28E-01	1	0.5	0	5.28E-01	1	0.5
7.2	2.09E-05	5.28E-01	1	0.5	0	5.28E-01	1	0.5
7.4	2.27E-05	5.28E-01	1	0.5	0	5.28E-01	1	0.5
7.6	2.46E-05	5.28E-01	1	0.5	0	5.28E-01	1	0.5
7.8	2.56E-05	5.28E-01	1	0.5	0	5.28E-01	1	0.5
8.0	2.72E-05	5.28E-01	1	0.5	0	5.28E-01	1	0.5
8.2	2.79E-05	5.28E-01	1	0.5	0	5.28E-01	1	0.5
8.4	2.92E-05	5.28E-01	1	0.5	0	5.28E-01	1	0.5
8.6	2.97E-05	5.28E-01	1	0.5	0	5.28E-01	1	0.5
8.8	3.09E-05	5.28E-01	1	0.5	0	5.28E-01	1	0.5
9.0	3.14E-05	5.28E-01	1	0.5	0	5.28E-01	1	0.5
9.2	3.15E-05	5.28E-01	1	0.5	0	5.28E-01	1	0.5
9.4	3.19E-05	5.28E-01	1	0.5	0	5.28E-01	1	0.5
9.6	3.22E-05	5.28E-01	1	0.5	0	5.28E-01	1	0.5
9.8	3.30E-05	5.28E-01	1	0.5	0	5.28E-01	1	0.5
10.0	3.25E-05	5.28E-01	1	0.5	0	5.28E-01	1	0.5

Table I.11: ISO ψ Variable Cd Exhaust Parameters

	Channel A				Channel B			
u	A_{eff}	b	a	β	A_{eff}	b	a	β
0.0	4.30E-05	5.28E-01	1	0.5	0	5.28E-01	1	0.5
0.2	4.28E-05	5.28E-01	1	0.5	0	5.28E-01	1	0.5
0.4	4.27E-05	5.28E-01	1	0.5	0	5.28E-01	1	0.5
0.6	4.30E-05	5.28E-01	1	0.5	0	5.28E-01	1	0.5
0.8	4.15E-05	5.28E-01	1	0.5	0	5.28E-01	1	0.5
1.0	4.12E-05	5.28E-01	1	0.5	0	5.28E-01	1	0.5
1.2	4.00E-05	5.28E-01	1	0.5	0	5.28E-01	1	0.5
1.4	3.96E-05	5.28E-01	1	0.5	0	5.28E-01	1	0.5
1.6	3.81E-05	5.28E-01	1	0.5	0	5.28E-01	1	0.5
1.8	3.76E-05	5.28E-01	1	0.5	0	5.28E-01	1	0.5
2.0	3.58E-05	5.28E-01	1	0.5	0	5.28E-01	1	0.5
2.2	3.43E-05	5.28E-01	1	0.5	0	5.28E-01	1	0.5
2.4	3.24E-05	5.28E-01	1	0.5	0	5.28E-01	1	0.5
2.6	3.07E-05	5.28E-01	1	0.5	0	5.28E-01	1	0.5
2.8	2.86E-05	5.28E-01	1	0.5	0	5.28E-01	1	0.5
3.0	2.66E-05	5.28E-01	1	0.5	0	5.28E-01	1	0.5
3.2	2.41E-05	5.28E-01	1	0.5	0	5.28E-01	1	0.5
3.4	2.11E-05	5.28E-01	1	0.5	0	5.28E-01	1	0.5
3.6	1.79E-05	5.28E-01	1	0.5	0	5.28E-01	1	0.5
3.8	1.45E-05	1.92E-01	1	0.5	0	5.28E-01	1	0.5
4.0	1.08E-05	2.22E-14	1	0.5	0	5.28E-01	1	0.5
4.2	6.63E-06	3.73E-14	1	0.5	0	5.28E-01	1	0.5
4.4	2.04E-06	4.33E-14	1	0.5	0	5.28E-01	1	0.5
4.6	9.39E-08	3.20E-14	1	0.5	0	5.28E-01	1	0.5
4.8	5.68E-08	3.18E-14	1	0.5	0	5.28E-01	1	0.5
5.0	4.38E-08	2.67E-14	1	0.5	3.73E-08	3.17E-14	1	0.5
5.2	0	5.28E-01	1	0.5	4.68E-08	3.66E-14	1	0.5
5.4	0	5.28E-01	1	0.5	5.95E-08	3.14E-14	1	0.5
5.6	0	5.28E-01	1	0.5	8.72E-08	3.41E-14	1	0.5
5.8	0	5.28E-01	1	0.5	7.18E-07	3.25E-14	1	0.5
6.0	0	5.28E-01	1	0.5	4.88E-06	2.66E-14	1	0.5
6.2	0	5.28E-01	1	0.5	9.27E-06	3.07E-14	1	0.5
6.4	0	5.28E-01	1	0.5	1.36E-05	2.22E-14	1	0.5
6.6	0	5.28E-01	1	0.5	1.79E-05	2.22E-14	1	0.5
6.8	0	5.28E-01	1	0.5	2.18E-05	1.68E-02	1	0.5
7.0	0	5.28E-01	1	0.5	2.53E-05	4.02E-02	1	0.5
7.2	0	5.28E-01	1	0.5	2.85E-05	8.24E-02	1	0.5
7.4	0	5.28E-01	1	0.5	3.14E-05	1.05E-01	1	0.5
7.6	0	5.28E-01	1	0.5	3.41E-05	1.29E-01	1	0.5
7.8	0	5.28E-01	1	0.5	3.63E-05	1.70E-01	1	0.5
8.0	0	5.28E-01	1	0.5	3.85E-05	1.74E-01	1	0.5
8.2	0	5.28E-01	1	0.5	4.05E-05	1.49E-01	1	0.5
8.4	0	5.28E-01	1	0.5	4.23E-05	1.37E-01	1	0.5
8.6	0	5.28E-01	1	0.5	4.39E-05	1.32E-01	1	0.5
8.8	0	5.28E-01	1	0.5	4.51E-05	1.83E-01	1	0.5
9.0	0	5.28E-01	1	0.5	4.74E-05	2.71E-02	1	0.5
9.2	0	5.28E-01	1	0.5	4.88E-05	1.08E-02	1	0.5
9.4	0	5.28E-01	1	0.5	4.84E-05	1.08E-01	1	0.5
9.6	0	5.28E-01	1	0.5	5.04E-05	2.03E-02	1	0.5
9.8	0	5.28E-01	1	0.5	5.14E-05	1.46E-02	1	0.5
10.0	0	5.28E-01	1	0.5	5.21E-05	1.22E-02	1	0.5

Table I.12: Extended ψ Constant Cd Inlet Parameters

	Channel A				Channel B			
u	A_{eff}	b	a	β	A_{eff}	b	a	β
0.0	0	5.28E-01	1.000	0.500	4.05E-05	5.28E-01	1.000	0.418
0.2	0	5.28E-01	1.000	0.500	4.07E-05	5.28E-01	1.000	0.445
0.4	0	5.28E-01	1.000	0.500	3.95E-05	5.28E-01	1.000	0.425
0.6	0	5.28E-01	1.000	0.500	3.94E-05	5.28E-01	1.000	0.445
0.8	0	5.28E-01	1.000	0.500	3.89E-05	5.28E-01	1.000	0.439
1.0	0	5.28E-01	1.000	0.500	3.85E-05	5.28E-01	1.000	0.458
1.2	0	5.28E-01	1.000	0.500	3.74E-05	5.28E-01	1.000	0.449
1.4	0	5.28E-01	1.000	0.500	3.75E-05	5.28E-01	1.000	0.483
1.6	0	5.28E-01	1.000	0.500	3.68E-05	5.28E-01	1.000	0.503
1.8	0	5.28E-01	1.000	0.500	3.55E-05	5.28E-01	1.000	0.497
2.0	0	5.28E-01	1.000	0.500	3.45E-05	5.28E-01	1.000	0.519
2.2	0	5.28E-01	1.000	0.500	3.25E-05	5.28E-01	1.000	0.454
2.4	0	5.28E-01	1.000	0.500	3.16E-05	5.28E-01	1.000	0.513
2.6	0	5.28E-01	1.000	0.500	3.02E-05	5.19E-01	1.000	0.546
2.8	0	5.28E-01	1.000	0.500	2.86E-05	4.81E-01	1.000	0.531
3.0	0	5.28E-01	1.000	0.500	2.65E-05	4.63E-01	1.000	0.525
3.2	0	5.28E-01	1.000	0.500	2.41E-05	4.18E-01	1.000	0.507
3.4	0	5.28E-01	1.000	0.500	2.14E-05	3.74E-01	1.000	0.500
3.6	0	5.28E-01	1.000	0.500	1.85E-05	3.16E-01	1.000	0.498
3.8	0	5.28E-01	1.000	0.500	1.51E-05	2.65E-01	1.000	0.479
4.0	0	5.28E-01	1.000	0.500	1.11E-05	1.96E-01	1.000	0.453
4.2	0	5.28E-01	1.000	0.500	6.89E-06	2.34E-14	1.000	0.466
4.4	0	5.28E-01	1.000	0.500	2.13E-06	2.34E-14	0.995	0.733
4.6	0	5.28E-01	1.000	0.500	4.18E-07	2.22E-14	0.866	1.000
4.8	0	5.28E-01	1.000	0.500	3.37E-07	2.22E-14	0.805	1.000
5.0	2.93E-07	2.22E-14	0.750	1.000	2.96E-07	2.22E-14	0.756	1.000
5.2	3.25E-07	2.22E-14	0.794	1.000	0	5.28E-01	1.000	0.500
5.4	3.64E-07	2.22E-14	0.835	1.000	0	5.28E-01	1.000	0.500
5.6	4.35E-07	2.22E-14	0.882	1.000	0	5.28E-01	1.000	0.500
5.8	1.34E-06	2.34E-14	0.979	0.721	0	5.28E-01	1.000	0.500
6.0	5.33E-06	3.33E-01	1.000	0.527	0	5.28E-01	1.000	0.500
6.2	9.61E-06	4.27E-01	1.000	0.490	0	5.28E-01	1.000	0.500
6.4	1.35E-05	4.21E-01	1.000	0.503	0	5.28E-01	1.000	0.500
6.6	1.72E-05	4.05E-01	1.000	0.504	0	5.28E-01	1.000	0.500
6.8	2.03E-05	4.34E-01	1.000	0.510	0	5.28E-01	1.000	0.500
7.0	2.29E-05	4.77E-01	1.000	0.524	0	5.28E-01	1.000	0.500
7.2	2.53E-05	5.08E-01	1.000	0.532	0	5.28E-01	1.000	0.500
7.4	2.74E-05	5.28E-01	1.000	0.533	0	5.28E-01	1.000	0.500
7.6	2.96E-05	5.28E-01	1.000	0.532	0	5.28E-01	1.000	0.500
7.8	3.06E-05	5.28E-01	1.000	0.449	0	5.28E-01	1.000	0.500
8.0	3.25E-05	5.28E-01	1.000	0.448	0	5.28E-01	1.000	0.500
8.2	3.40E-05	5.28E-01	1.000	0.504	0	5.28E-01	1.000	0.500
8.4	3.55E-05	5.28E-01	1.000	0.499	0	5.28E-01	1.000	0.500
8.6	3.63E-05	5.28E-01	1.000	0.476	0	5.28E-01	1.000	0.500
8.8	3.76E-05	5.28E-01	1.000	0.473	0	5.28E-01	1.000	0.500
9.0	3.82E-05	5.28E-01	1.000	0.459	0	5.28E-01	1.000	0.500
9.2	3.85E-05	5.28E-01	1.000	0.439	0	5.28E-01	1.000	0.500
9.4	3.90E-05	5.28E-01	1.000	0.446	0	5.28E-01	1.000	0.500
9.6	3.93E-05	5.28E-01	1.000	0.430	0	5.28E-01	1.000	0.500
9.8	4.02E-05	5.28E-01	1.000	0.449	0	5.28E-01	1.000	0.500
10.0	3.98E-05	5.28E-01	1.000	0.418	0	5.28E-01	1.000	0.500

Table I.13: Extended ψ Constant Cd Exhaust Parameters

	Channel A				Channel B			
u	A_{eff}	b	a	β	A_{eff}	b	a	β
0.0	6.13E-05	3.56E-01	0.988	1.000	0	5.28E-01	1.000	0.500
0.2	6.10E-05	3.47E-01	0.988	1.000	0	5.28E-01	1.000	0.500
0.4	6.10E-05	3.38E-01	0.988	1.000	0	5.28E-01	1.000	0.500
0.6	6.14E-05	3.21E-01	0.988	1.000	0	5.28E-01	1.000	0.500
0.8	5.92E-05	3.37E-01	0.988	1.000	0	5.28E-01	1.000	0.500
1.0	5.89E-05	3.25E-01	0.988	1.000	0	5.28E-01	1.000	0.500
1.2	5.71E-05	3.35E-01	0.988	1.000	0	5.28E-01	1.000	0.500
1.4	5.65E-05	3.23E-01	0.988	1.000	0	5.28E-01	1.000	0.500
1.6	5.45E-05	3.26E-01	0.988	1.000	0	5.28E-01	1.000	0.500
1.8	5.38E-05	3.04E-01	0.988	1.000	0	5.28E-01	1.000	0.500
2.0	5.12E-05	3.16E-01	0.988	1.000	0	5.28E-01	1.000	0.500
2.2	4.90E-05	3.08E-01	0.988	1.000	0	5.28E-01	1.000	0.500
2.4	4.64E-05	3.07E-01	0.988	1.000	0	5.28E-01	1.000	0.500
2.6	4.40E-05	2.89E-01	0.988	1.000	0	5.28E-01	1.000	0.500
2.8	4.10E-05	2.77E-01	0.988	1.000	0	5.28E-01	1.000	0.500
3.0	3.81E-05	2.56E-01	0.988	1.000	0	5.28E-01	1.000	0.500
3.2	3.47E-05	2.30E-01	0.988	0.992	0	5.28E-01	1.000	0.500
3.4	3.04E-05	2.10E-01	0.988	0.978	0	5.28E-01	1.000	0.500
3.6	2.59E-05	1.81E-01	0.988	0.994	0	5.28E-01	1.000	0.500
3.8	2.08E-05	1.46E-01	0.987	1.000	0	5.28E-01	1.000	0.500
4.0	1.59E-05	2.22E-14	0.985	1.000	0	5.28E-01	1.000	0.500
4.2	9.79E-06	2.22E-14	0.963	1.000	0	5.28E-01	1.000	0.500
4.4	3.33E-06	2.22E-14	0.829	1.000	0	5.28E-01	1.000	0.500
4.6	8.67E-07	2.22E-14	0.234	1.000	0	5.28E-01	1.000	0.500
4.8	9.27E-07	2.22E-14	0.200	1.000	0	5.28E-01	1.000	0.500
5.0	9.96E-07	2.22E-14	0.187	1.000	8.85E-07	2.22E-14	0.185	1.000
5.2	0	5.28E-01	1.000	0.500	8.10E-07	2.22E-14	0.195	1.000
5.4	0	5.28E-01	1.000	0.500	7.50E-07	2.22E-14	0.210	1.000
5.6	0	5.28E-01	1.000	0.500	7.31E-07	2.22E-14	0.240	1.000
5.8	0	5.28E-01	1.000	0.500	1.51E-06	2.22E-14	0.639	1.000
6.0	0	5.28E-01	1.000	0.500	7.23E-06	2.22E-14	0.951	1.000
6.2	0	5.28E-01	1.000	0.500	1.36E-05	2.22E-14	0.978	1.000
6.4	0	5.28E-01	1.000	0.500	2.01E-05	2.22E-14	0.984	1.000
6.6	0	5.28E-01	1.000	0.500	2.63E-05	2.22E-14	0.987	1.000
6.8	0	5.28E-01	1.000	0.500	3.22E-05	2.22E-14	0.988	1.000
7.0	0	5.28E-01	1.000	0.500	3.75E-05	2.22E-14	0.988	1.000
7.2	0	5.28E-01	1.000	0.500	4.24E-05	2.22E-14	0.987	1.000
7.4	0	5.28E-01	1.000	0.500	4.70E-05	2.22E-14	0.988	1.000
7.6	0	5.28E-01	1.000	0.500	5.12E-05	2.22E-14	0.988	1.000
7.8	0	5.28E-01	1.000	0.500	5.38E-05	3.89E-02	0.986	1.000
8.0	0	5.28E-01	1.000	0.500	5.70E-05	4.80E-02	0.986	1.000
8.2	0	5.28E-01	1.000	0.500	5.92E-05	7.57E-02	0.987	1.000
8.4	0	5.28E-01	1.000	0.500	6.16E-05	8.46E-02	0.987	1.000
8.6	0	5.28E-01	1.000	0.500	6.38E-05	8.43E-02	0.987	1.000
8.8	0	5.28E-01	1.000	0.500	6.62E-05	7.32E-02	0.987	1.000
9.0	0	5.28E-01	1.000	0.500	6.85E-05	5.54E-02	0.988	1.000
9.2	0	5.28E-01	1.000	0.500	7.08E-05	3.54E-02	0.988	1.000
9.4	0	5.28E-01	1.000	0.500	6.96E-05	1.05E-01	0.988	1.000
9.6	0	5.28E-01	1.000	0.500	7.24E-05	6.85E-02	0.988	1.000
9.8	0	5.28E-01	1.000	0.500	7.40E-05	5.90E-02	0.988	1.000
10.0	0	5.28E-01	1.000	0.500	7.50E-05	5.71E-02	0.988	1.000

Table I.14: Extended ψ Variable Cd Inlet Parameters

	Channel A				Channel B			
u	A_{eff}	b	a	β	A_{eff}	b	a	β
0.0	0	5.28E-01	1.000	5.00E-01	3.31E-05	5.28E-01	1.000	2.22E-14
0.2	0	5.28E-01	1.000	5.00E-01	3.34E-05	5.28E-01	1.000	2.22E-14
0.4	0	5.28E-01	1.000	5.00E-01	3.23E-05	5.28E-01	1.000	2.22E-14
0.6	0	5.28E-01	1.000	5.00E-01	3.22E-05	5.28E-01	1.000	2.22E-14
0.8	0	5.28E-01	1.000	5.00E-01	3.17E-05	5.28E-01	1.000	2.22E-14
1.0	0	5.28E-01	1.000	5.00E-01	3.15E-05	5.28E-01	1.000	2.22E-14
1.2	0	5.28E-01	1.000	5.00E-01	3.05E-05	5.28E-01	1.000	2.22E-14
1.4	0	5.28E-01	1.000	5.00E-01	3.07E-05	5.28E-01	1.000	2.22E-14
1.6	0	5.28E-01	1.000	5.00E-01	3.02E-05	5.28E-01	1.000	2.22E-14
1.8	0	5.28E-01	1.000	5.00E-01	2.91E-05	5.28E-01	1.000	2.22E-14
2.0	0	5.28E-01	1.000	5.00E-01	2.83E-05	5.28E-01	1.000	2.22E-14
2.2	0	5.28E-01	1.000	5.00E-01	2.70E-05	5.28E-01	1.000	2.22E-14
2.4	0	5.28E-01	1.000	5.00E-01	2.62E-05	5.28E-01	1.000	2.22E-14
2.6	0	5.28E-01	1.000	5.00E-01	2.48E-05	5.28E-01	1.000	2.22E-14
2.8	0	5.28E-01	1.000	5.00E-01	2.35E-05	5.28E-01	1.000	2.22E-14
3.0	0	5.28E-01	1.000	5.00E-01	2.17E-05	5.28E-01	1.000	2.22E-14
3.2	0	5.28E-01	1.000	5.00E-01	1.96E-05	5.28E-01	1.000	2.22E-14
3.4	0	5.28E-01	1.000	5.00E-01	1.73E-05	5.28E-01	1.000	2.22E-14
3.6	0	5.28E-01	1.000	5.00E-01	1.48E-05	5.28E-01	1.000	2.22E-14
3.8	0	5.28E-01	1.000	5.00E-01	1.19E-05	5.28E-01	1.000	2.22E-14
4.0	0	5.28E-01	1.000	5.00E-01	8.64E-06	5.28E-01	1.000	2.22E-14
4.2	0	5.28E-01	1.000	5.00E-01	5.07E-06	5.28E-01	1.000	2.22E-14
4.4	0	5.28E-01	1.000	5.00E-01	1.46E-06	1.31E-04	0.995	8.29E-02
4.6	0	5.28E-01	1.000	5.00E-01	2.96E-07	2.34E-14	0.866	6.83E-01
4.8	0	5.28E-01	1.000	5.00E-01	2.43E-07	2.34E-14	0.805	8.06E-01
5.0	2.14E-07	2.34E-14	0.750	8.98E-01	2.15E-07	2.34E-14	0.756	8.78E-01
5.2	2.33E-07	2.34E-14	0.794	8.05E-01	0	5.28E-01	1.000	5.00E-01
5.4	2.56E-07	2.34E-14	0.835	7.10E-01	0	5.28E-01	1.000	5.00E-01
5.6	2.99E-07	2.34E-14	0.882	5.88E-01	0	5.28E-01	1.000	5.00E-01
5.8	8.98E-07	9.86E-05	0.979	6.00E-02	0	5.28E-01	1.000	5.00E-01
6.0	4.23E-06	5.28E-01	1.000	2.22E-14	0	5.28E-01	1.000	5.00E-01
6.2	7.81E-06	5.28E-01	1.000	2.22E-14	0	5.28E-01	1.000	5.00E-01
6.4	1.10E-05	5.28E-01	1.000	2.22E-14	0	5.28E-01	1.000	5.00E-01
6.6	1.39E-05	5.28E-01	1.000	2.22E-14	0	5.28E-01	1.000	5.00E-01
6.8	1.65E-05	5.28E-01	1.000	2.22E-14	0	5.28E-01	1.000	5.00E-01
7.0	1.88E-05	5.28E-01	1.000	2.22E-14	0	5.28E-01	1.000	5.00E-01
7.2	2.07E-05	5.28E-01	1.000	2.22E-14	0	5.28E-01	1.000	5.00E-01
7.4	2.25E-05	5.28E-01	1.000	2.22E-14	0	5.28E-01	1.000	5.00E-01
7.6	2.45E-05	5.28E-01	1.000	2.22E-14	0	5.28E-01	1.000	5.00E-01
7.8	2.55E-05	5.28E-01	1.000	2.22E-14	0	5.28E-01	1.000	5.00E-01
8.0	2.71E-05	5.28E-01	1.000	2.22E-14	0	5.28E-01	1.000	5.00E-01
8.2	2.78E-05	5.28E-01	1.000	2.22E-14	0	5.28E-01	1.000	5.00E-01
8.4	2.91E-05	5.28E-01	1.000	2.22E-14	0	5.28E-01	1.000	5.00E-01
8.6	2.96E-05	5.28E-01	1.000	2.22E-14	0	5.28E-01	1.000	5.00E-01
8.8	3.08E-05	5.28E-01	1.000	2.22E-14	0	5.28E-01	1.000	5.00E-01
9.0	3.13E-05	5.28E-01	1.000	2.22E-14	0	5.28E-01	1.000	5.00E-01
9.2	3.14E-05	5.28E-01	1.000	2.22E-14	0	5.28E-01	1.000	5.00E-01
9.4	3.18E-05	5.28E-01	1.000	2.22E-14	0	5.28E-01	1.000	5.00E-01
9.6	3.21E-05	5.28E-01	1.000	2.22E-14	0	5.28E-01	1.000	5.00E-01
9.8	3.29E-05	5.28E-01	1.000	2.22E-14	0	5.28E-01	1.000	5.00E-01
10.0	3.25E-05	5.28E-01	1.000	2.22E-14	0	5.28E-01	1.000	5.00E-01

Table I.15: Extended ψ Variable Cd Exhaust Parameters

	Channel A				Channel B			
u	A_{eff}	b	a	β	A_{eff}	b	a	β
0.0	4.29E-05	5.28E-01	0.988	2.22E-14	0	5.28E-01	1.000	0.500
0.2	4.27E-05	5.28E-01	0.988	2.22E-14	0	5.28E-01	1.000	0.500
0.4	4.26E-05	5.28E-01	0.988	1.29E-11	0	5.28E-01	1.000	0.500
0.6	4.29E-05	5.28E-01	0.988	1.47E-02	0	5.28E-01	1.000	0.500
0.8	4.14E-05	5.28E-01	0.988	2.22E-14	0	5.28E-01	1.000	0.500
1.0	4.12E-05	5.28E-01	0.988	3.96E-11	0	5.28E-01	1.000	0.500
1.2	3.99E-05	5.28E-01	0.988	2.22E-14	0	5.28E-01	1.000	0.500
1.4	3.95E-05	5.28E-01	0.988	2.22E-14	0	5.28E-01	1.000	0.500
1.6	3.81E-05	5.28E-01	0.988	2.22E-14	0	5.28E-01	1.000	0.500
1.8	3.76E-05	5.11E-01	0.988	1.19E-02	0	5.28E-01	1.000	0.500
2.0	3.58E-05	5.28E-01	0.988	2.22E-14	0	5.28E-01	1.000	0.500
2.2	3.43E-05	5.28E-01	0.988	2.22E-14	0	5.28E-01	1.000	0.500
2.4	3.24E-05	5.28E-01	0.988	2.22E-14	0	5.28E-01	1.000	0.500
2.6	3.07E-05	4.74E-01	0.988	8.02E-10	0	5.28E-01	1.000	0.500
2.8	2.86E-05	3.52E-01	0.988	9.46E-09	0	5.28E-01	1.000	0.500
3.0	2.66E-05	3.25E-01	0.988	2.01E-02	0	5.28E-01	1.000	0.500
3.2	2.41E-05	2.69E-01	0.988	4.86E-02	0	5.28E-01	1.000	0.500
3.4	2.11E-05	2.33E-01	0.988	6.64E-02	0	5.28E-01	1.000	0.500
3.6	1.80E-05	1.89E-01	0.988	1.27E-01	0	5.28E-01	1.000	0.500
3.8	1.44E-05	1.52E-01	0.987	2.29E-01	0	5.28E-01	1.000	0.500
4.0	1.08E-05	2.34E-14	0.985	3.87E-01	0	5.28E-01	1.000	0.500
4.2	6.86E-06	2.34E-14	0.963	8.78E-01	0	5.28E-01	1.000	0.500
4.4	2.38E-06	2.22E-14	0.829	1.00E+00	0	5.28E-01	1.000	0.500
4.6	6.00E-07	2.22E-14	0.234	1.00E+00	0	5.28E-01	1.000	0.500
4.8	6.40E-07	2.22E-14	0.200	1.00E+00	0	5.28E-01	1.000	0.500
5.0	6.88E-07	2.22E-14	0.187	1.00E+00	6.11E-07	2.22E-14	0.185	1.000
5.2	0	5.28E-01	1.000	5.00E-01	5.59E-07	2.22E-14	0.195	1.000
5.4	0	5.28E-01	1.000	5.00E-01	5.19E-07	2.22E-14	0.210	1.000
5.6	0	5.28E-01	1.000	5.00E-01	5.06E-07	2.22E-14	0.240	1.000
5.8	0	5.28E-01	1.000	5.00E-01	1.07E-06	2.22E-14	0.639	1.000
6.0	0	5.28E-01	1.000	5.00E-01	5.14E-06	2.22E-14	0.951	1.000
6.2	0	5.28E-01	1.000	5.00E-01	9.31E-06	2.34E-14	0.978	0.530
6.4	0	5.28E-01	1.000	5.00E-01	1.35E-05	2.34E-14	0.984	0.390
6.6	0	5.28E-01	1.000	5.00E-01	1.77E-05	2.34E-14	0.987	0.350
6.8	0	5.28E-01	1.000	5.00E-01	2.19E-05	2.74E-06	0.988	0.483
7.0	0	5.28E-01	1.000	5.00E-01	2.55E-05	4.27E-06	0.988	0.485
7.2	0	5.28E-01	1.000	5.00E-01	2.89E-05	6.55E-06	0.987	0.483
7.4	0	5.28E-01	1.000	5.00E-01	3.17E-05	2.34E-14	0.988	0.386
7.6	0	5.28E-01	1.000	5.00E-01	3.45E-05	2.14E-02	0.988	0.397
7.8	0	5.28E-01	1.000	5.00E-01	3.63E-05	1.73E-01	0.986	0.499
8.0	0	5.28E-01	1.000	5.00E-01	3.85E-05	1.79E-01	0.986	0.513
8.2	0	5.28E-01	1.000	5.00E-01	4.04E-05	1.91E-01	0.987	0.525
8.4	0	5.28E-01	1.000	5.00E-01	4.22E-05	1.96E-01	0.987	0.543
8.6	0	5.28E-01	1.000	5.00E-01	4.37E-05	1.98E-01	0.987	0.558
8.8	0	5.28E-01	1.000	5.00E-01	4.52E-05	1.97E-01	0.987	0.577
9.0	0	5.28E-01	1.000	5.00E-01	4.65E-05	1.94E-01	0.988	0.593
9.2	0	5.28E-01	1.000	5.00E-01	4.78E-05	1.94E-01	0.988	0.622
9.4	0	5.28E-01	1.000	5.00E-01	4.80E-05	2.10E-01	0.988	0.603
9.6	0	5.28E-01	1.000	5.00E-01	4.93E-05	2.02E-01	0.988	0.619
9.8	0	5.28E-01	1.000	5.00E-01	5.03E-05	2.01E-01	0.988	0.630
10.0	0	5.28E-01	1.000	5.00E-01	5.10E-05	2.03E-01	0.988	0.645

Table I.16: Miscellaneous Tube Parameters

Parameter	**Value**
L_t	5.5 m
ID	0.008 m
c	340.29 $m.s^{-1}$

Table I.17: Extended ψ Constant Cd Tube Parameters

u	A_{eff}	b	a	β
0	2.01e-05	0.341	1	0.957
10	1.92e-05	0.471	1	0.525